Title
Photomechanical Response of Molecular Nanostructures

Author
Pechenezhskiy, Ivan Viktorovich

Publication Date
2014

Peer reviewed|Thesis/dissertation

Photomechanical Response of Molecular Nanostructures

by

Ivan Viktorovich Pechenezhskiy

A dissertation submitted in partial satisfaction of the
requirements for the degree of
Doctor of Philosophy

in

Physics

in the

Graduate Division

of the

University of California, Berkeley

Committee in charge:

Professor Michael F. Crommie, Chair
Professor Feng Wang
Professor Gerard Marriott

Spring 2014

Photomechanical Response of Molecular Nanostructures

Abstract

Photomechanical Response of Molecular Nanostructures

by

Ivan Viktorovich Pechenezhskiy

Doctor of Philosophy in Physics

University of California, Berkeley

Professor Michael F. Crommie, Chair

This dissertation focuses on the optomechanical behavior of molecular adsorbates on semiconducting and metal surfaces. Specifically, light-induced conformational changes of an azobenzene derivative on a semiconducting surface and infrared active vibrational modes of diamondoid molecules on a metal surface were studied in a scanning tunneling microscopy setup.

Using conventional scanning tunneling microscopy, the self-assembly and light-induced mechanical switching of 3,3′,5,5′-tetra-*tert*-butylazobenzene deposited on GaAs(110) were explored at the single-molecule level. After exposure to ultraviolet light, tetra-*tert*-butylazobenzene molecules exhibited conformational changes attributed to *trans* to *cis* photoisomerization. Photoisomerization of the molecules was observed to occur preferentially in one-dimensional stripes, a behavior that is significantly different from optically induced switching behavior observed when these molecules were placed on a gold surface.

To characterize infrared absorption of submonolayers of molecules on electrically conducting crystals, a new scanning-tunneling-microscopy-based spectroscopy technique was developed. The technique employs a scanning tunneling microscope as a precise detector to measure the expansion of a molecule-decorated crystal that is irradiated by infrared light from a tunable laser source. Using this technique, the infrared absorption spectra of adamantane, [121]tetramantane, and [123]tetramantane on a Au(111) surface were obtained. Significant differences between the infrared spectra for the two tetramantane isomers show the power of the new technique to differentiate chemical structures even when single-molecule-resolved scanning tunneling microscopy images look quite similar. For adamantane on Au(111), the simplest studied system, *ab initio* calculations allowed for the interpretation of the microscopic vibrational dynamics revealed by the measurements. The infrared spectrum of an adamantane monolayer on Au(111) was found to be substantially modified with respect to the gas-phase infrared spectrum due to both the adamantane-adamantane interaction and adamantane-gold interactions.

The results presented in this dissertation improve our understanding of photoisomerizational and optically induced vibrational properties of molecules placed in a condensed matter

environment, and highlight the important role played by the molecule-surface and molecule-molecule interactions. These results are highly relevant to the field of molecular electronics and optically actuated molecular nanomachines.

To the memory of my parents.

Contents

List of Figures

List of Tables

Acknowledgments

First and foremost, I would like to thank Professor Mike Crommie who has been a great adviser throughout my time at Berkeley. His scientific enthusiasm helped me stay optimistic, the freedom he gave me allowed me to grow and his narratives on human psychology taught me the importance clearly presenting my work. I will always cherish the time I spent in his lab and the support that he has given me.

Jong Cho was the first graduate student that I worked with when I came to Berkeley. He taught me basic information about the scanning tunneling microscope (STM), the ultra-high vacuum systems, and the art of repairing the STM. We worked on a couple of projects together including the photoswitching of an azobenzene derivative on a gallium arsenide surface. Giang Nguyen was the second grad student that I have had the pleasure of working with. We performed most of the experimental work on diamondoid molecules, tried out numerous other experimental ideas, and maintained the STM. For several years, we have basically shared all our successes and failures. Giang is a terrific co-worker, with an ever optimistic smile on his face. He was also the one who ensured that my brain was constantly challenged with some important but sometimes totally irrelevant questions. The work on diamondoid molecules would not be even possible without Xiaoping Hong who, together with Professor Feng Wang, designed and built a tunable infrared laser required for our infrared spectroscopy experiments. Xiaoping, Giang, and I spent many hours together arguing about all kinds of experimental issues and I learned a great deal through those discussions. I also learned some optical tricks from Xiaoping. Finally, Yuki Sakai performed all the difficult calculations that we needed to understand the adamantane data while Hannes Böckmann performed a lot of simulations that enhanced our understanding of many technical aspects of our experiments.

There have been a number of professors who helped us choose the research directions and interpret our data. Professor Feng Wang generated many great ideas and provided help with the infrared spectroscopy experiments. I have definitely learned a lot through discussions with him and really appreciate his deep knowledge of many different subjects. Professors Gerard Marriott, Felix Fischer, and Jeremy Dahl all provided me with a great deal of useful advice and ideas throughout my time at Berkeley. Professors Rodrigo Capaz, Steve Louie, and Marvin Cohen provided explanations and helped in the computational aspect of the adamantane work. I would like to thank all of them for their scientific advice.

There have been a number of people in the lab who I have learned enormously from and have been lucky to work with. I am thankful to postdoctoral researchers Alex Riss (who started so many endless discussions with me on topics ranging from the scanning tunneling microscopy, to the meaning of the life, but I actually doubt that we ever came up with any meaningful conclusions), Luis Berbil-Bautista (who convinced me that failures will eventually result in success), Dimas de Oteyza (who once managed to right a capsized boat while I sat on it), Sinisa Coh (who provided help in understanding the adamantane data) as well as to Chenggang Tao, Miguel Ugeda, Jairo Velasco, and Danny Haberer who all provided a great deal of advice. It has been a real pleasure to work in the same lab with

graduate students Aaron Bradley (who helped me with countless number of different things, including proof-reading real nonsense written by me), Victor Brar (whose controversial and provocative opinions led to so many interesting debates), Yen-Chia Chen (who almost always was ahead of me with all formal requirements, forcing me to stay on top of my things as well), Sebastian Wickenburg (who got me involved in one project that was like a breath of fresh air), Niv Levy (who taught me how to value my time), and Ryan Yamachika (whose experience with diamondoid molecules saved us a lot of time). I also had a lot of useful and sometimes fun discussions with graduate students Trinity Joshi, Ryan Cloke, Dillon Wong, Zahra Pedramrazi, Chen Chen, Kacey Meaker, Xiaowei Zhang, and Yang Wang. Finally, undergraduate student Brandon Giles assisted us with some experiments and junior researcher Chad Germany proof-read some sections of this dissertation.

I feel extremely lucky to have gotten to work with all these people. In this dissertation I will often use the pronoun "we" to properly acknowledge the contributions made by my collaborators.

I would also like to mention the enormous inspiration I got from classes given by Professors Eugene Commins, Eli Yablonovitch, Holger Müller, James Analytis, Joe Orenstein, and Ahmet Yildiz. Their classes were definitely among my best experiences I have had at Berkeley.

My graduate student work here could not have been completed without additional help from Anne Takizawa, Elaine Quiter, Donna Sakima, and Kathy Lee. I am very thankful to all of them for helping me to meet numerous deadlines. Special thanks go to Eleanor Crump who professionally led the response to several power outages that affected our lab.

Finally, I thank all of my friends for their support during my years at Berkeley.

Chapter 1

Introduction

1.1 Towards Molecular Nanomachines

In 1959 Richard Feynman in his talk at the annual meeting of the American Physical Society at Caltech [1] outlined the scope, the potential and the problems of a new field of creating, manipulating and controlling things at very small scale, the field that would be later called 'nanotechnology' [2]. Over the past few decades nanotechnology has undergone remarkable developments and these developments have already benefited many different scientific and practical fields ranging from electronics and energy efficient technologies to biology and medicine. Nevertheless, it is generally believed that the field of nanotechnology is still in its very early age. In fact, many questions that Richard Feynman brought up in his famous talk have not been yet fully resolved. Specifically, among many other things, he questioned how we can characterize objects at the atomic and molecular scales, how we can build tiny machines made from only few hundreds of atoms that can still do some useful work, and how we can control such machines? There can be little doubt that the answers to these profound questions will eventually lead to numerous technological applications.

Regarding the instrumentation to characterize things at the nanoscale, one of the most important breakthroughs arrived in 1982 with the invention of a new microscopy technique, scanning tunneling microscopy (STM), by Gerd Binnig and Heinrich Rohrer [3, 4]. This development revolutionized the field of nanoscience since it became possible for the first time to directly observe atoms and molecules. Scanning tunneling microscopy allows local investigation of the electronic properties of surfaces [5, 6]. More impressively, a scanning tunneling microscope (STM) can be used to manipulate atoms and molecules that are adsorbed to a surface [7–10]. Due to these outstanding capabilities, STM has become the instrument of choice for many studies at the nanoscale. A number of other scanning probe microscopy techniques have also been developed following the success of STM, such as atomic force microscopy [11] and near-field scanning optical microscopy [12, 13]. Although extremely powerful in their realms, scanning probe microscopy techniques do suffer from some serious limitations. Therefore, novel experimental techniques are still widely sought after to advance

our capabilities of probing things at the nanoscale.

We are still far away from achieving the ultimate goal of constructing molecular-scale machines with pre-defined useful behavior, despite significant achievements in recent years. In principle, the basic laws of quantum mechanics and electromagnetism, which should govern the behavior of such machines, are very well understood. However, due to the fact that the number of possible chemical structures is enormous and the interactions of molecules with their environment can be extremely complex, solving a general theoretical problem of designing a nanomachine with a specified functionality is currently an impossible task given modern computational capabilities. First principle computations without any significant approximations can be performed at best only for molecular systems consisting of hundreds of atoms [14], and the computations can become unmanageably intensive in the presence of a dissipative environment. Since the simulations of relatively complex systems are extremely challenging, a more feasible strategy to achieve the ultimate goal is required. Specifically, one can start with some molecules that are known to exhibit certain behavior in a specific environment (for example, in a biological system), then place these molecules in another well controlled environment (potentially suitable for applications) and characterize the molecular behavior in this new environment with the available experimental tools. Once the observation is done, some computations with appropriate approximations can be done in order to find out whether it is possible to understand the observed behavior. Such computations can potentially identify the most important interactions in the system and suggest improved designs. Additionally, comparing the results of computations to the experimental observations can help improve the computational methods by validating the appropriate approximations. In subsequent iterations, either the redesigned molecular structures can be synthesized (unfortunately not yet in the 'atom-by-atom' fashion that Richard Feynman dreamt about but rather using conventional chemistry synthesis) and studied in the same environment or the previously studied molecular structures can be placed in a new environment for further observations. The hope is to develop a set of functional building blocks that can be used for the design of molecular nanomachines and a set of empirical rules that can describe the behavior of these building blocks. Eventually, successful development of functional nanomachines should become possible.

While quantum mechanics may allow, in principle, molecular machines with quite novel behavior, it appears reasonable to focus the early practical efforts on the design and synthesis of molecular machines that exhibit very simple mechanical behavior. In other words, while the behavior of molecular machines is governed by the laws of quantum mechanics, the motion of this class of machines can initially be visualized (for simplicity) as being classical.

Finally, there should be a way to control functional nanomachines. This control might be implemented with external stimuli, such as electrical fields, electrical currents, temperature, solution acidity, and light [15, 16]. Employing light for this purpose is definitely a very appealing approach since light naturally provides a remote way to control objects at the nanoscale. In addition, light can supply energy to nanomachines, and it is compatible with fast operations. Frequency-dependent response of molecular nanostructures may allow for selective control and for communication of various commands to achieve complex behavior.

One of the simplest systems that can be considered as a starting point for building functional nanomachines is a single molecule that is adsorbed to a surface and is irradiated with light. Such systems are the focus of this dissertation, and the content here should be viewed in the context of the preceding introductory remarks. It will be shown here how local environments can affect the photoisomerizational behavior of molecules, how advances in characterization instrumentation can provide new insights into the photoinduced oscillatory behavior of molecules on a surface, and how our understanding of different molecular-scale interactions can be enhanced with first principle calculations.

1.2 Photoinduced Mechanical-Like Motion of Molecules at Surfaces

For many practical applications, photoactive molecules are expected to be integrated into larger devices. In many cases, therefore, molecules will experience the influence of the condensed matter environment. A model system for exploring effects of the condensed matter environment involves molecules that bind to the surface of a crystal that is placed in vacuum to reduce the number of possible interactions. The surface of the crystal is irradiated with light and the response of the molecules is detected with a probe. One of the primary goals of such a study would be to investigate how conversion of electromagnetic energy into the mechanical activity of molecular nanostructures is affected by the presence of a surface and other molecules that might be adsorbed to the same surface.

The two most important forms of photoinduced mechanical-like motion that will be considered in this dissertation are photoisomerization and vibrational motion. In fact the useful functionality of future nanomachines might be thought of as arising from different active molecular building blocks that exhibit combined photoisomerizational, vibrational and/or rotational behaviors since proper combinations of such active elements could result in complex, useful dynamics.

Photoisomerization can be viewed as photoinduced mechanical switching from one metastable conformation of a molecule to another in response to light illumination [17]. Not surprisingly, molecules that exhibit this optomechanical switching behavior are very promising building blocks for synthetic molecular machines. These molecules, due to their ability to reversibly change mechanical conformation upon illumination, are nearly ideal mechanically metastable active elements, capable of converting light energy into directed mechanical motion. The problem, however, is that this photomechanical switching behavior can be significantly modified or even quenched in the presence of a dissipative environment, and, specifically, in the presence of a surface [18]. Photoisomerizational processes are typically considered as a sequence of several steps: the photon-induced excitation from a ground electronic state to an excited state (i.e., to a wave packet formed according to the Franck-Condon principle), the wave packet evolution along the reaction pathway on the potential energy surface of the excited state, the radiative decay or the radiationless relaxation through a conical

intersection to the ground state, and, finally, the vibrational relaxation to a new metastable configuration of atomic nuclei [19–21]. The dynamics of this complicated process can be significantly modified when molecules are adsorbed to a surface. Bonding of the molecules to the surface can modify the electronic and vibrational energy levels of the molecules due to hybridization of the molecular states with the states of the surface, charge transfer between the molecules and the surface, and/or surface screening effects [22]. In addition, bonding to the surface can reduce the accessible space of molecular conformations due to high energy costs associated with specific arrangements of atoms in the presence of the surface. This steric hindrance is, therefore, expected to significantly reshape the potential energy surfaces. Finally, the surface can drastically reduce the lifetimes of the excited states by providing extra relaxation channels for the excited states. (Surfaces, however, can also introduce new, useful excitation mechanisms for photoisomerization [23, 24].) Interaction with the surface, steric hindrance, and the reduced lifetimes of excited states can easily alter and even quench the photoisomerization of nanomachine molecules [25, 26].

Light can also excite various vibrational modes of molecules. While vibrational motion alone cannot serve as the single working principle of nanomachine operation, the vibrations can play an important role as part of more complex motion (including activation over an energy barrier). More importantly, the molecular vibrations can provide information about molecular structure as well as the local environment that molecules experience. This is due to the fact that natural vibrational frequencies of molecules are very sensitive to external forces that the molecules experience in the presence of other molecules or solid state systems. Photoisomerizational properties can be extremely sensitive to the local environment but the dynamics of photoisomerizational processes can be complex. In fact, photoisomerizational dynamics of even an isolated molecule can be extremely involved [19]. Vibrations, on the other hand, are relatively simple excitations of a molecule and the theory of molecular vibrations is very well understood [27]. Because of this, detailed computations even for relatively large systems are often possible. Thus, vibrational spectroscopy, enhanced by computational results, can be employed to probe local molecular environment.

Since molecules can exhibit surprisingly complex behavior as they convert energy into mechanical motion in a dissipative environment, a reasonable strategy to understand the fundamental behavior of such systems is to explore a range of different systems that exhibit one or both types of behavior. The ultimate goal here is to find common principles and empirical rules that can help us to understand the molecular motion and to allow the mechanical control at a fundamental level.

1.3 Summary of Thesis Contents

This dissertation is organized as follows. Following a very brief overview of STM and STM instrumentation in Sections 1.4 and 1.5, the main results of the work will be presented.

In Chapter 2 an investigation of photoswitching properties of an azobenzene derivative adsorbed onto a GaAs(110) surface will be presented. The reversible photoswitching proper-

ties of azobenzene have been previously studied on metal surfaces [25, 26, 28–32], but not on semiconductors. Semiconductors, however, provide a more desirable substrate due to their lower electron density, better optical properties, and potential for integration with existing technology. It will be shown that the photoswitching behavior of the azobenzene derivative differs significantly from optically induced switching behavior previously observed when the molecules were placed on a gold surface.

In Chapter 3 a simple technique whereby an STM can achieve vibrational spectroscopy of molecular adsorbates at the submonolayer level will be described. As the molecules on the surface absorb infrared light in resonance with one of their vibrational modes they relax back to the unexcited state and transfer the vibrational energy to the substrate, causing sub-Ångström expansion of the surface, and thus allowing the STM to detect the infrared modes of the adsorbed molecules. Spectra of higher diamondoid molecules, specifically [121]tetramantane and [123]tetramantane, deposited on a Au(111) surface will be presented and the performance of the new spectroscopy technique will be discussed.

The new spectroscopy technique was also used to study the vibrational properties of adamantane on a Au(111) surface, and this study will be reported in Chapter 4. The experimental adamantane spectra will be compared to spectra computed via density functional theory to reveal the roles played by adamantane-gold and adamantane-adamantane interactions.

1.4 Scanning Tunneling Microscopy

An STM is a very sensitive instrument that allows sub-Ångström-resolution imaging of atoms and molecules on conducting substrates. Furthermore, STM-based scanning tunneling spectroscopy can be used to probe local electronic structure of bare surfaces [5, 6], defects [33], dopants [34], atomic adsorbates [35], etc., and vibrational properties of molecular adsorbates [36–38]. An STM can also be used to manipulate single atoms and molecules that adsorb to surfaces [7–10, 39].

An STM employes a metallic tip that is positioned within several Ångströms from the surface of a conducting substrate, so that quantum mechanical tunneling is possible between the tip and the surface when a bias is applied across the tip-sample junction. The tunneling current depends exponentially on the tip-surface distance [3] and this is the origin of the extreme topographical sensitivity of STM measurements. The resolution in the direction perpendicular to the surface (the 'Z direction') can be easily as good as 10 pm and an order of magnitude better in the best instruments [40]. For practical reasons, STM topography measurements are typically done in a constant-current mode, i.e., with the tunneling current kept constant by a feedback control loop implemented on the tunneling current while the tip moves in a raster-like manner above the sample surface. Such motion of the tip can be realized with a piezo tube scanner that holds the tip. By applying appropriate voltages to the piezo scanner electrodes, the apex of STM tip can be moved along all three spatial axes. The voltage that is applied to the piezo scanner to control the distance between the surface

and the tip and keep the tunneling current constant is recorded as a function of the position above the sample, yielding the topography of the sample surface. This voltage is referred to as the 'Z signal' and can be calibrated in units of length. The imaging capabilities of the STM and its remarkable resolution in the Z direction are indispensable for the studies presented in this dissertation.

A solid theoretical treatment of STM using Bardeen's tunneling formalism [41] has been given by J. Tersoff and D. R. Hamann [42, 43].

Extensive discussions of the numerous questions related to STM can easily be found in the literature [3, 4, 6, 44, 45].

1.5 Instrumentation

1.5.1 Scanning Tunneling Microscope

The STM measurements presented in this dissertation were performed using a home-built variable-temperature ultra-high vacuum scanning tunneling microscope with optical access to the sample. This STM machine was designed and built by Katsumi Nagaoka, Mike Crommie, Matt Comstock, Hadrian Knotz, and David Kwon [46]. Subsequent significant modifications (and repairs) to the machine have been performed by Matt Comstock [46], Niv Levy [47], Jong Cho [48], Luis Berbil-Bautista, Giang Nguyen, and me. The overview of the major recent modifications to the microscope are given below.

Gwyddion, an open-source software, was used to analyze the STM data and process the STM images [49].

1.5.2 Control System Upgrade

A scanning probe microscopy (SPM) control system, which consists of special electronics and software installed on a computer to run the STM scanhead, is required to operate the STM instrument and acquire data.

Though the data reported in this dissertation were acquired using the RHK SPM 1000 Control System (RHK Technology), we have recently upgraded both the software and hardware to the Nanonis SPM Control System (SPECS Zurich GmbH) since the Nanonis SPM Control System provides a higher degree of flexibility in setting up and conducting our experiments. The transition to the new electronics was fairly straightforward and did not require any modifications to the other parts of the STM instrument. (Switching back to the RHK SPM 1000 Control System is possible, should it be necessary.)

The only undocumented piece of information with regard to the upgrade is that pin 7 of the DIO PORT A THROUGH on the backside of the Nanonis HVA4 (SPECS Zurich GmbH) can be used for the controlled ('fine') stage of the tip approach procedure (see Section A.3 of the appendix for details).

1.5.3 Shear Piezo Stacks for the Piezo Motor

The controlled tip motion towards and away from the sample surface is achieved with a coarse approach mechanism ('piezo motor') of the 'Pan-type' design [40]. This piezo motor operates in the so-called 'stick-slip' motion mode, which is well-described in the literature [40, 46, 48, 50]. In the STM used in this work, the coarse approach mechanism consists of six shear piezo stacks that are glued inside the STM body cavity in three sets of two on each face of the cavity [46, 48]. When the voltage across a piezo stack is ramped, the unglued face of the piezo stack can either slide along or move together with the STM sapphire prism, which holds the STM scanner [46], depending on the voltage slew rate and the shear motion of the other piezo stacks. It had been found that the original design of these shear piezo stacks was prone to short circuit. After an accident that destroyed the coarse approach mechanism, I rebuilt the piezo stacks using new design principles [47]. The new design of the piezo stacks has been already reported in Reference 48 and all details of the corresponding assembling process are given in Reference 47. The new shear peizo stacks have been working without any serious problems for five years by the time of writing this dissertation.

1.5.4 Electronics for Driving the Piezo Stacks

Originally, the STM shear piezo stacks were powered by a custom control box (the 'walker box') built by the Physics Electronics Support Group (University of California, Berkeley). The walker box generates high voltage waveforms that actuate the piezo stacks and the piezo stacks move the STM prism step by step in the stick-slip mode. There had been a serious problem with the retraction waveforms generated by the original walker box. The origin of the problem is explained here. Two motion phases must be distinguished during each piezo motor step in either direction: a slow piezo shear ('stick phase') in which the piezo stacks stay attached to the STM prism and a fast slip ('slip phase') in which the piezo stacks break the frictional contact with the prim and slide along it. Therefore, both approach and retraction single-step waveforms have two corresponding phases: a slow phase when a slowly varying voltage is applied across the piezo stacks to shear the piezo stacks simultaneously in order to move the STM sapphire prism, and a fast phase when the voltages across the piezo stacks are abruptly but asynchronously changed, so that the piezo stacks shear quickly, one after another, and ideally do not carry the sapphire prism with them [40, 46, 48, 50]. It is implied that each step begins and ends with the piezo stacks being discharged.

To move the prism a single step towards the sample, the original walker box rapidly ramped the voltages across the piezo stacks to a positive value, shearing the piezo stacks in turns without disturbing the sapphire prism, then slowly and synchronously drove the voltages back to zero, pushing the sapphire prism towards the sample surface. To retract the prism one step back, the voltages across the piezo stacks were quickly but asynchronously raised to a negative value and then slowly and synchronously brought back to zero. Thus, the reversion of the motion direction was achieved by flipping the polarity of the driving voltage waveforms. It appeared that the performance of the piezo motor during the fast slip phases

of the retraction process was not perfect when the original walker box was used to power the piezo stacks. Specifically, some incidental motion of the sapphire prism towards the surface occurred when the piezo stack voltages were quickly driven to the negative value. Such unintended motion often caused very undesirable crashes. When the tip was reapproached to the same spot on the sample surface, these crashes revealed themselves via the resulting extremely poor surface conditions. It should be noted here that one of the great advantages of the Pan-style walker is its reproducibility of walking, i.e., the walker can repeatedly approach the exact same spot after many cycles of retraction and approach (in other words, the tip can be macroscopically moved away from the surface and brought back to the exact same microscopic spot). This advantage was partially compromised when the original walker box was used. There were no simple workaround because the shape of the waveforms was set by the original walker box hardware design and thus the waveforms could not be modified.

To eliminate the crashes during the initial steps of the retraction procedure, new electronics has been designed. The new electronics is controlled by a program run in the LabVIEW environment (National Instruments Corporation), and modifications to the approach and retraction waveforms can be readily done by replacing the content of the waveform files that are external to the LabVIEW program. The design of the new electronics and an overview of its performance is given in Appendix A. A waveform that is very similar to the original waveform is used for the approach [i.e., the voltage across a piezo stack is quickly driven towards a positive value and subsequently slowly driven back to zero as can be seen in Figure A.4(a)]. However, to retract the prism a step away from the surface, a slowly increasing voltage is applied across all the piezo stacks to shear the stacks and move the prism away from the surface; and only after this motion the piezo stack voltages are quickly but asynchronously driven back to zero, bringing all the piezo stacks to the initial state, one piezo stack after another [Figure A.4(b)]. Reversal of the coarse motion direction is achieved by flipping the fast and slow phases in a single-step waveform while the driving voltage polarity stays the same. The new walker electronics, being very reliable in general, have eliminated the problem of the crashes. Without any hardware modifications the new electronics can be used together with either the Nanonis SPM Control System or the RHK SPM 1000 Control System (see Appendix A for details).

1.5.5 Cryogenic System

An extensive overview of the STM cryogenic system is given in M. J. Comstock's dissertation [46] and subsequent improvements to the STM design that led to a lower STM base temperature are described in J. Cho's dissertation [48]. Nevertheless, it has been found that the absence of a good seal between the Heli-tran transfer line dewar bayonet and the bayonet extension was a cause of periodic oscillations in the STM base temperature. These thermal oscillations had been notably interfering with the STM measurements. The thermal oscillations have been eliminated by applying an indium wire seal as described in Appendix B.

1.5.6 Sample Preparation

Successful preparation of many different atomically clean surfaces can be achieved in the STM setup used for this work. This dissertation is, however, focused on measurements taken on the GaAs(110) and Au(111) surfaces. GaAs(110) surfaces were obtained by *in-situ* cleaving of GaAs crystals in ultra-high vacuum as described in J. Cho's dissertation [48]. The Au(111) surface of a single crystal was cleaned by repeating cycles of sputtering and annealing [48].

The tetra-*tert*-butylazobenzene molecules studied in Chapter 2 were deposited onto GaAs(110) using a standard thermal sublimation technique. The design of the home-built evaporator used for this purpose is described in Reference 48. The tetramantane isomers studied in Chapter 3 were deposited using a home-built Knudsen cell evaporator, which is described in Reference 51. Due to a relatively high vapor pressure, the adamantane molecules studied in Chapter 4 were deposited using a precision leak valve as described in details in Section 4.2.

Chapter 2

Self-Assembly and Photomechanical Switching of Tetra-*Tert*-Butylazobenzene on GaAs(110)

In this chapter an STM study of self-assembly and light-induced mechanical switching of an azobenzene derivative deposited on GaAs(110) is presented. 3,3′,5,5′-Tetra-*tert*-butylazobenzene (TTB-AB) molecules in the *trans* isomer configuration were found to form well-ordered islands on GaAs(110). After exposure to ultraviolet light, the TTB-AB molecules exhibited conformational changes attributed to *trans* to *cis* photoisomerization. Photoisomerization of TTB-AB/GaAs(110) is observed to occur preferentially in one-dimensional stripes. This one-dimensional cascade behavior differs significantly from optically induced switching behavior observed when TTB-AB molecules are placed on a gold surface.

This chapter is adapted with permission from I. V. Pechenezhskiy et al., "Self-Assembly and Photomechanical Switching of an Azobenzene Derivative on GaAs(110): Scanning Tunneling Microscopy Study", J. Phys. Chem. C **116**, 1052 (2012).

2.1 Introduction

Azobenzene-derived molecules are an appealing candidate for future nanometer-scale optomechanical applications [15, 53] due to their ability to robustly convert light into mechanical motion at the single-molecule level. When irradiated by ultraviolet (UV) and visible light, azobenzene-derived molecules undergo reversible photoisomerization between *trans* and *cis* structural isomers [17]. The isomerization of these molecules has been widely studied in both gas and solution phases [17], leading to many proposals for light-powered nanomachines [15], molecular electronics [53], and new biochemical elements [54, 55]. Many

potential nanotechnology applications of these molecules, however, require placing them on a surface. Compared to gas- and solution-based environments, molecular structures on surfaces exhibit substantially different photomechanical switching properties. This has been observed through electron energy loss spectroscopy [56], two-photon photoemission spectroscopy [23, 57], and scanning tunneling microscopy [25, 26, 28–32]. Most of these molecular surface switching studies have been conducted on metal substrates and, in particular, on Au(111) [23, 25, 26, 29, 30, 56, 57]. Semiconductor surfaces are an appealing alternative for surface-bound molecular photoswitching studies due to their more tunable electronic and optical properties.

In this chapter we describe an STM study of molecular photomechanical switching for an azobenzene derivative adsorbed to the surface of a GaAs single crystal. The (110) surface of GaAs was chosen for this study because it does not possess surface states within its direct band gap (1.43 eV)[58]. We find that 3,3',5,5'-tetra-*tert*-butylazobenzene (TTB-AB) molecules adsorbed onto GaAs(110) self-assemble into well-ordered molecular islands of *trans* isomers that have two preferred orientations with respect to the surface. Grain boundaries between these orientations are clearly resolved, and the molecular island structures are consistent with a commensurate overlayer model. Upon UV exposure ($\lambda = 375$ nm) TTB-AB molecules on GaAs(110) exhibit conformational changes that lead to formation of one-dimensional stripes of mechanically altered molecules. We are able to use the STM tip to reverse this switching, which supports our conclusion that these changes can be attributed to molecular photoisomerization. This switching behavior differs significantly from previous observations of TTB-AB photoswitching on Au(111), suggesting that stronger molecule-molecule interactions occur on GaAs(110) compared to Au(111).

2.2 Experimental Methods

Atomically clean GaAs(110) surfaces were obtained by *in-situ* cleaving of GaAs crystals in ultra-high vacuum at room temperature [48]. Both n-type (Si doped, carrier concentration (0.1–0.5) $\times 10^{19}$cm^{-3}) and p-type (Zn doped, carrier concentration (0.8–1.5) $\times 10^{19}$cm^{-3}) GaAs wafers were used. Before deposition of TTB-AB, the surface of each sample was imaged by STM to ensure its cleanliness. These images were consistent with previously reported GaAs images [58–61]. No significant difference in molecular behavior was observed between n- and p-type GaAs. TTB-AB molecules were synthesized via oxidative coupling reactions of 3,5-di-*tert*-butylaniline [62]. Submonolayer coverages of the *trans* isomer of TTB-AB were achieved via thermal evaporation onto GaAs(110) substrates held at 13 ± 2 K. Samples were then annealed at room temperature for 10–30 minutes in order to achieve ordered molecular islands. All STM images were acquired in the temperature range of 11–15 K with tunnel currents below 30 pA for stable imaging (unless otherwise specified). An electrochemically etched tungsten tip was used [48]. A cw laser aligned at an external viewport provided UV radiation at $\lambda = 375$ nm wavelength with an average intensity of 92 mW/cm^2 at the sample surface. During laser exposures the STM tip was retracted several millimeters away from

the surface to avoid shadowing effects of the tip and the sample temperature was maintained between 11 and 15 K. Checks were performed to ensure that shining light into the chamber did not cause surface contamination (i.e., light was shined on a bare surface for more than 17 hours and the surface was observed to remain clean).

2.3 Self-Assembly of Tetra-*Tert*-Butylazobenzene on GaAs(110)

Figures 2.1(a) and 2.1(b) show STM images of a typical monolayer island of TTB-AB on GaAs(110), prepared as described in Section 2.2. Comparison of the dimensions of the features in the STM image with expected TTB-AB size reveals that each lobe seen in the image corresponds to the position of one of the four *tert*-butyl groups of a TTB-AB molecule. This four-lobed structure is clearly seen in the close-up image shown in Figure 2.1(b) where a single molecule is outlined (a similar four-lobed structure has been seen for TTB-AB on metal surfaces [24, 25, 63–67]). This planar configuration indicates that TTB-AB is adsorbed onto GaAs(110) in the *trans* state. The orientation of TTB-AB molecules with respect to the underlying GaAs surface atoms was determined by comparing the four-lobed molecular structure [Figure 2.1(b)] with the atomic row configuration of the bare GaAs surface [Figure 2.1(a)]. This suggests a molecular arrangement of TTB-AB on GaAs(110) as shown in Figure 2.1(c). In this model structure the TTB-AB molecules are commensurate with the GaAs surface, and the molecular lattice can be described by lattice vectors aligned with the $[\bar{3}34]$ and $[1\bar{1}1]$ crystallographic directions of GaAs. The lengths of the lattice vectors for this periodic molecular structure (averaged over many molecular islands) are found to be 16.7 ± 0.3 and 9.9 ± 0.2 Å, respectively. Our data is thus consistent with a commensurate molecular overlayer, in which case one would expect molecular lattice constants of 16.5 and 9.8 Å, respectively. The TTB-AB molecules are also observed to exhibit an arrangement that can be described as a reflection of this structure across $[1\bar{1}0]$, leading to two different orientational domains for TTB-AB/GaAs(110). Figure 2.2 shows an ordered TTB-AB island which consists of domains having both possible orientations.

2.4 Photoswitching of Tetra-*Tert*-Butylazobenzene on GaAs(110)

After illumination with UV light ($\lambda = 375$ nm) the TTB-AB molecules on GaAs(110) undergo a conformational change. Figure 2.3 shows images of the same molecular island obtained before and after an 18-hour exposure to UV light. New morphological features appear as a result of this exposure, the highest concentrations of which occur near the molecular island edges and domain boundaries. These features appear as molecule-sized protrusions in the STM topographs. Most of the optically induced protrusions have similar apparent height,

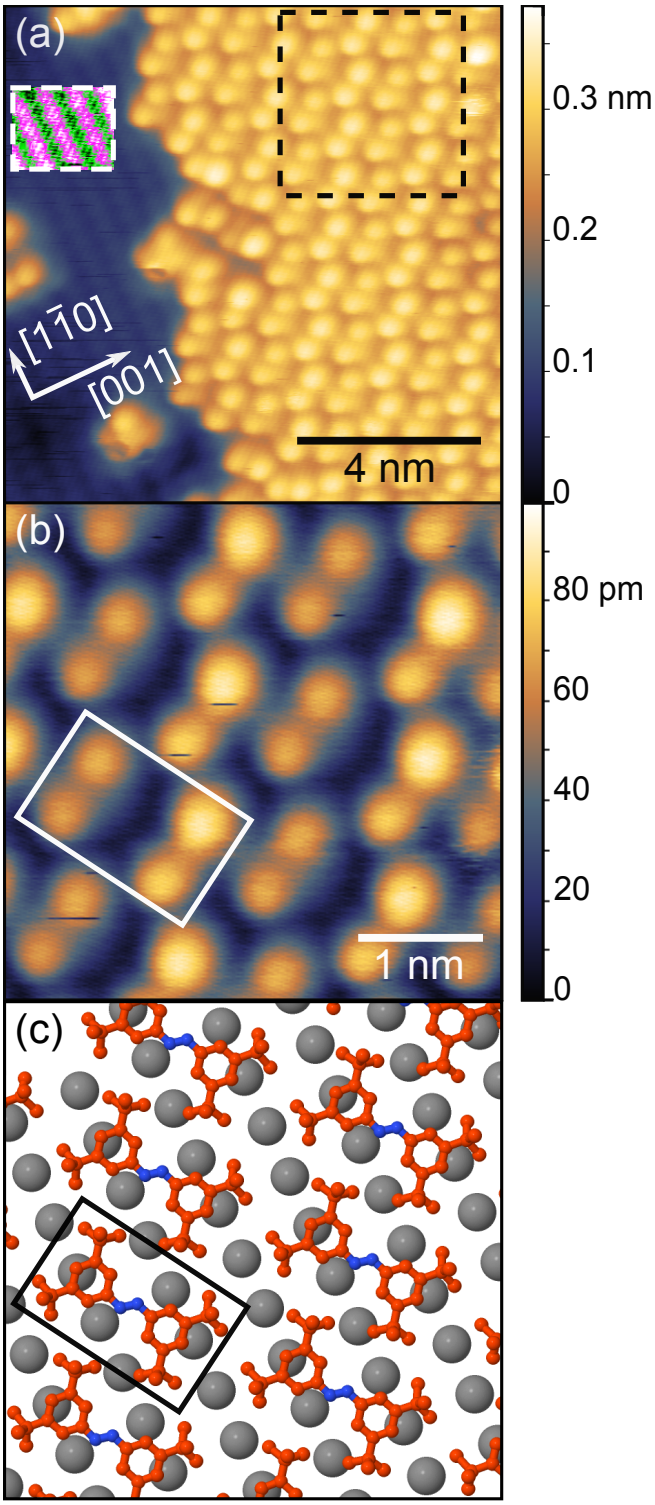

Figure 2.1: (a) STM constant-current image of TTB-AB molecules in *trans* configuration on a GaAs(110) surface ($V_{\text{sample}} = 2.0\,\text{V}$, $I = 15\,\text{pA}$). Crystallographic directions of the GaAs(110) surface are depicted by white arrows. The color scale within area bordered by the white dashed box has been modified to allow observation of underlying GaAs atomic rows (highest pink point is 0.10 nm high, while lowest green point is 0.08 nm high). (b) Close-up scan of the region inside the black dashed square in (a) shows *trans*-TTB-AB molecules in a highly ordered phase ($V_{\text{sample}} = 2.5\,\text{V}$, $I = 15\,\text{pA}$). A single *trans*-TTB-AB molecule is surrounded by a white box. (c) Ball-and-stick model of *trans*-TTB-AB on GaAs(110) representing the arrangement seen in (b). Red, blue and gray balls correspond to carbon, nitrogen and gallium atoms, respectively. Only gallium atoms in the first surface layer of GaAs(110) are depicted. A black box surrounds a single TTB-AB molecule corresponding to the molecule shown in the white box in (b).

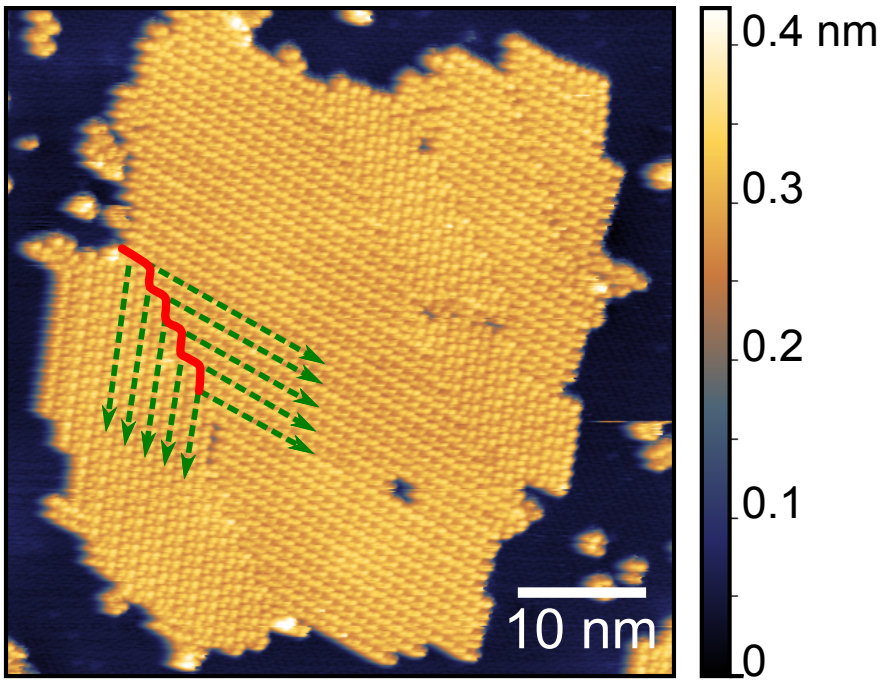

Figure 2.2: STM topograph of a monolayer island of *trans*-TTB-AB molecules on GaAs(110) exhibiting domains with different molecular orientations ($V_{\text{sample}} = -2.0\,\text{V}$, $I = 20\,\text{pA}$). The red solid line outlines a portion of the border between two adjacent molecular domains, and the green dashed arrows show separate rows of molecules in the two domains.

suggesting that they represent molecules that have switched to some new structure. Such photoswitched molecules typically appear as a bright lobe surrounded by dimmer peripheral lobes in a configuration similar to what has been previously reported for *cis*-TTB-AB isomers on metals [24, 25, 63–67]. The photoswitched molecules on GaAs(110) often appear in short one-dimensional stripes along either the $[\bar{1}1\bar{1}]$ or $[\bar{1}11]$ crystallographic directions (depending on molecular island orientation). Several photoswitched stripes along $[\bar{1}11]$ are indicated by blue arrows in Figure 2.3(b). Analysis of photoinduced switching rates shows that after 20 hours of UV illumination typically about one-third of the TTB-AB molecules have isomerized from *trans* to *cis*.

2.5 Discussion

It is possible to reverse molecules from the photoswitched state back to the initial *trans* state by changing STM tunneling parameters between consecutive scans. Figure 2.4 shows STM images of a photoswitched molecule both before [Figure 2.4(a)] and after [Figure 2.4(b)] switching it back to the *trans* state via scanning (this process does not reverse all switched molecules, as seen by the fact that other optically switched molecules in the figure did not re-

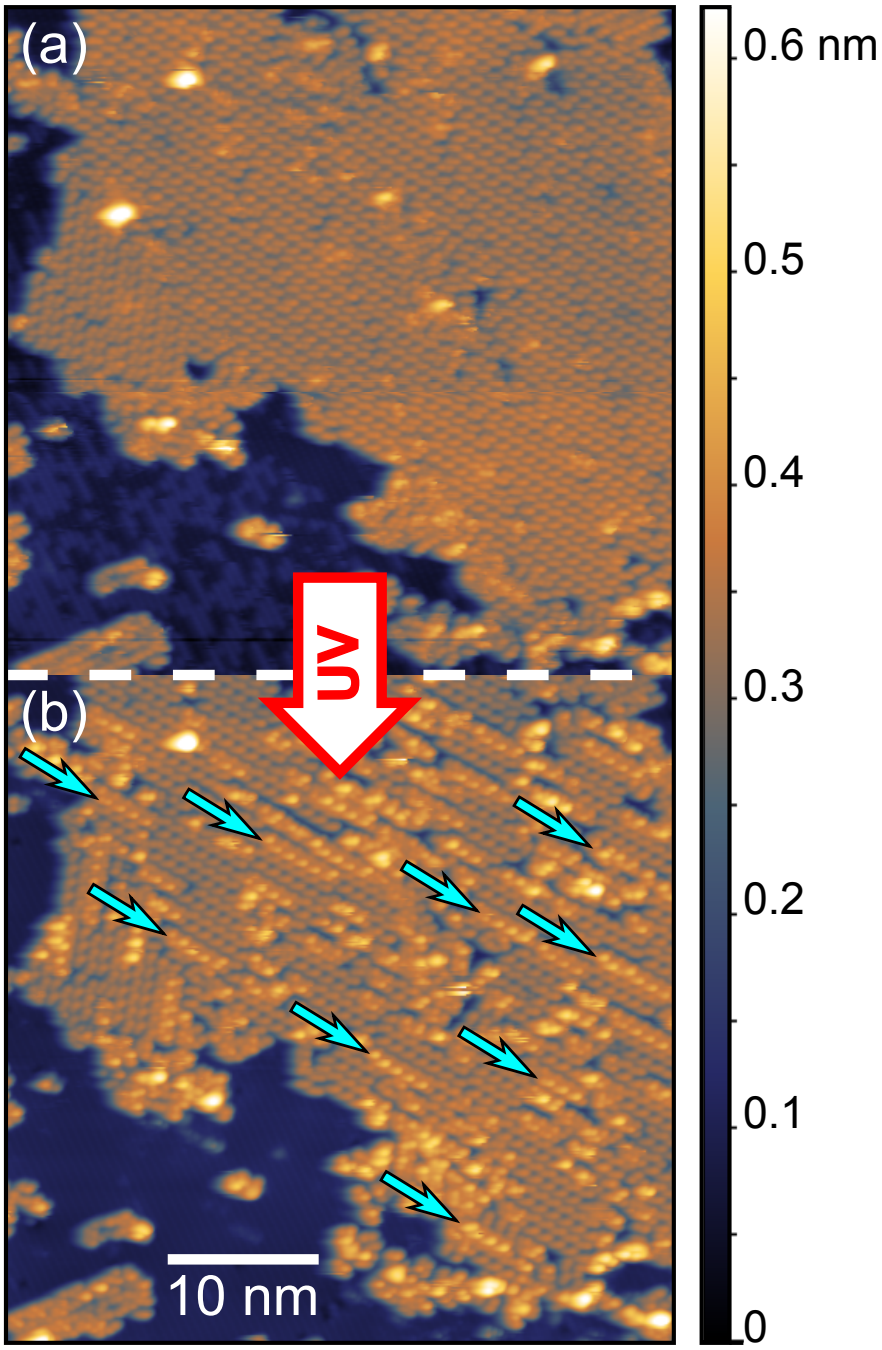

Figure 2.3: Photoisomerization of TTB-AB molecules on GaAs(110). The same TTB-AB molecular island is shown (a) before and (b) after an 18-hour exposure to UV irradiation at 375 nm and 92 mW/cm^2 ($V_{\text{sample}} = -2.0$ V, $I = 25$ pA). Molecules in the *cis* configuration appear to have one brighter lobe and occur in one-dimensional stripes, as indicated by blue arrows.

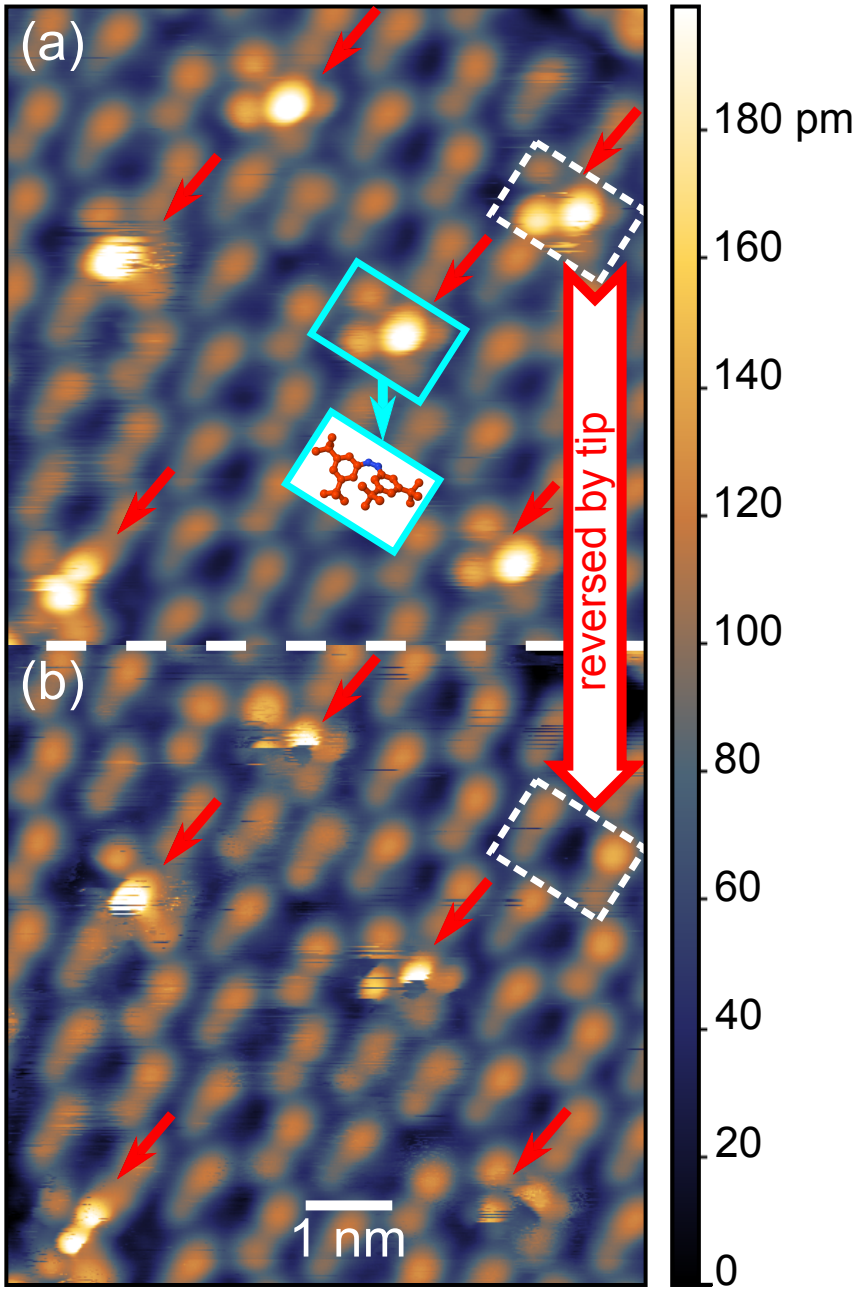

Figure 2.4: Two successive STM scans showing tip-induced reverse switching [from *cis* (a) to *trans* (b)] of a single TTB-AB molecule on GaAs(110) (the switched molecule is surrounded by the dashed white box). Red arrows point to TTB-AB molecules in photoswitched *cis* configuration. Inset shows schematic ball-and-stick structural model of photoswitched molecule in *cis* state. Tunneling parameters: (a) $V_{\text{sample}} = -2.0\,\text{V}$, $I = 20\,\text{pA}$, (b) $V_{\text{sample}} = -2.0\,\text{V}$, $I = 80\,\text{pA}$. Reverse switching is caused by scanning at the higher tunnel current of (b).

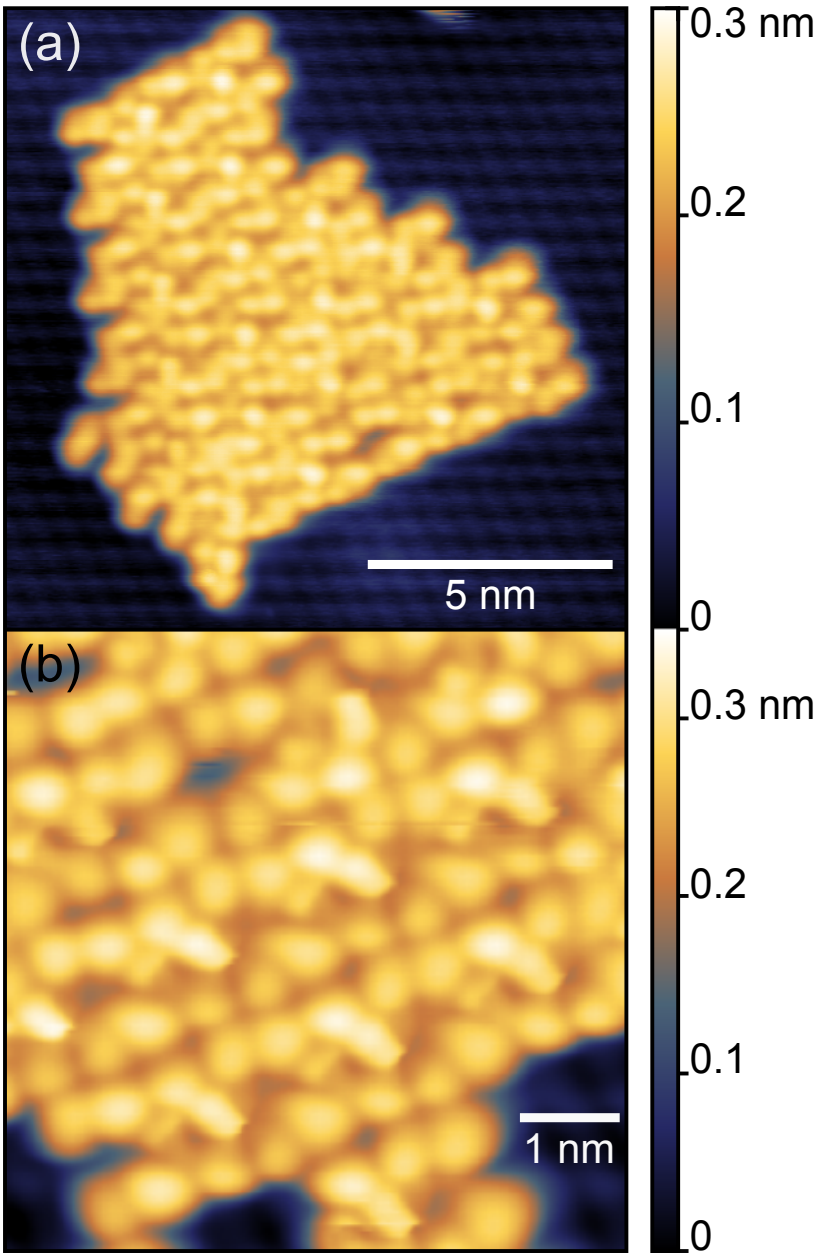

Figure 2.5: (a) STM constant-current image of an ordered TTB-AB molecular island that was formed after annealing a sample at room temperature for 2 hours and 30 minutes ($V_{\text{sample}} = -2.0\,\text{V}$, $I = 30\,\text{pA}$). (b) Close-up scan of another TTB-AB island that was formed after annealing a sample at room temperature for about 1 hour ($V_{\text{sample}} = -2.0\,\text{V}$, $I = 30\,\text{pA}$). The molecules appear in a self-assembly phase that is notably different from the one observed in Figures 2.1 and 2.2.

verse during this particular scan). Reverse switching in this case occurred when the set point current was changed from 20 to 80 pA while keeping the sample bias at −2.0 V. The slightly changed appearance of other molecules in Figure 2.4(b) is attributed to increased molecule-tip interactions during the scan at the higher current set point (note, for example, that the raised *tert*-butyl groups of the *cis* molecules sometimes shift during scanning). The observed structural reversibility implies that the photoswitched structures are TTB-AB molecules in the *cis* isomeric configuration [Figure 2.4(a) inset], rather than simply reflecting contamination or optically induced molecular decomposition. This interpretation is bolstered by the fact that our control experiment of shining light on a bare surface rules out light-induced contamination, as well as the fact that forward (from *trans* to *cis*) tip-induced transitions were also observed (although not shown in Figure 2.4). Tip-induced switching occurred randomly for a range of biases between −2.5 and +2.5 V. For typical scanning parameters, however, tip-induced switching events are very rare and, therefore, can be ruled out as the origin of the switched molecules observed after light irradiation (tip-induced switching accounts for less than 2% of switched molecules observed). The observed photoinduced changes can not be attributed to a possible local increase of the sample temperature when the sample is exposed to UV radiation. This possibility of thermally induced conformational changes is ruled out by our control experiment of annealing the TTB-AB/GaAs(110) samples at room temperature for 1 hour or longer. The main effect of such annealing is an occasional formation of islands in a new self-assembled phase that is shown in Figure 2.5. No one-dimensional strips formed by *cis*-TTB-AB isomers were observed in this control experiment.

Since the energy of the 375 nm photons used here (3.3 eV) is larger than the band gap of GaAs (1.43 eV), the electron-hole pairs created in GaAs may interact with the TTB-AB molecules, resulting in substrate-induced isomerization. On the other hand, UV-visible absorption spectra of TTB-AB in cyclohexane suggest that the molecules do have direct absorption near 375 nm [23, 57]. It is, therefore, difficult to determine from our experiment whether the photoisomerization arises from direct excitation of a charge carrier within the molecule or from indirect excitation via transfer of charge carriers excited in GaAs. Experiments performed on azobenzene derivatives on metals suggest that both of these mechanisms can contribute to surface-bound molecular photoswitching [23, 31].

In contrast to the photoswitching behavior observed here for TTB-AB on GaAs(110), the majority of TTB-AB molecules that photoswitch on Au(111) exhibit spatially random switching (i.e., on Au(111) the vast majority of molecules show no tendency to preferentially switch in the vicinity of other switched molecules or near island edges) [66]. On GaAs(110) the TTB-AB molecules show a clear enhancement of switching rate for molecules near island edges and domain walls. These switching nucleation sites are likely due to reduced steric hindrance at these locations, and indicate that a switched molecule causes adjacent molecules to switch more easily on GaAs(110) [a behavior not observed on Au(111)]. This increase in switching probability propagates to the interior of molecular islands in a cascade-like process. This suggests a stronger molecule-molecule interaction for TTB-AB on GaAs(110) compared to TTB-AB on Au(111), and that disorder in the molecular layer on GaAs(110) leads to a reduced energy barrier for switching.

2.6 Conclusion

In conclusion, self-assembly and photomechanical switching of individual TTB-AB molecules on a bare GaAs surface have been experimentally observed. The results reveal a defect-induced triggering pattern that differs from switching mechanisms previously observed for TTB-AB on gold. The varied switching behaviors seen for TTB-AB on different substrates highlight the important role played by the substrate in determining the photomechanical switching properties of molecules.

Chapter 3

Infrared Spectroscopy of Tetramantane Isomers on Au(111)

In this chapter a new scanning-tunneling-microscopy-based spectroscopy technique to characterize infrared absorption of submonolayers of molecules on conducting crystals is described. The technique employs a scanning tunneling microscope as a precise detector to measure the expansion of a molecule-decorated crystal that is irradiated by infrared light from a tunable laser source. Using this technique, the infrared absorption spectra of [121]tetramantane and [123]tetramantane on Au(111) were obtained. Significant differences between the infrared spectra for these two isomers show the power of this new technique to differentiate chemical structures even when single-molecule-resolved scanning tunneling microscopy images look quite similar. Furthermore, the new technique was found to yield significantly better spectral resolution than STM-based inelastic electron tunneling spectroscopy, and to allow determination of optical absorption cross sections. Compared to infrared spectroscopy of bulk tetramantane powders, infrared scanning tunneling microscopy spectra reveal narrower and blueshifted vibrational peaks for an ordered tetramantane adlayer. Differences between bulk and surface tetramantane vibrational spectra are explained via molecule-molecule interactions.

This chapter is adapted with permission from I. V. Pechenezhskiy et al., "Infrared Spectroscopy of Molecular Submonolayers on Surfaces by Infrared Scanning Tunneling Microscopy: Tetramantane on Au(111)", Phys. Rev. Lett. **111**, 126101 (2013).

3.1 Introduction

Simultaneously probing the vibrational behavior and local electronic or geometric structure of molecular adsorbates is important for understanding their physical and chemical properties. Scanning tunneling microscopy is a powerful tool for this purpose since it can yield subnanometer-resolved topographical information and orbital energetics, as well as vibra-

tional properties through inelastic electron tunneling spectroscopy (STM-IETS) [36, 37]. Electron-based STM-IETS, however, does not allow direct probing of optical processes and has a spectral resolution limited by thermal broadening. STM-induced luminescence [69–73] and tip-enhanced Raman spectroscopy (TERS) [74–76] are related techniques that do give simultaneous local and optovibrational information. STM-induced luminescence, however, can so far probe only selected vibrational modes through vibronic transitions and has energy resolution that is partially limited by electronic excited state lifetimes, while TERS is limited to dyelike molecules with large Raman cross sections and usually requires satisfying the resonant Raman condition [77]. Atomic force microscopy infrared spectroscopy (photothermal induced resonance) [78–81] is an additional technique that has been employed to acquire local infrared (IR) absorption spectra and images of surface structures, but this technique works only for high-coverage aggregates of thickness > 40–$80\,\mathrm{nm}$ [80, 81] and so cannot yet address the adsorbate-dominated submonolayer regime.

Here we demonstrate a new STM-based vibrational spectroscopy which overcomes many of the drawbacks of the above-mentioned techniques by using the STM as a sensitive detector to probe the IR response of adsorbed molecular assemblies. Although our technique is not yet capable of performing single-molecule-resolved IR spectroscopy (it averages over a wider surface area), the technique can be used to probe a wide range of molecular species at submonolayer coverages and with the subthermal energy resolution inherent to IR spectroscopy, while the surface can be simultaneously characterized by conventional STM imaging. We refer to this new technique as IRSTM. Using IRSTM we have obtained IR absorption spectra and STM images of submonolayer coverages of the diamondoid molecules [121]tetramantane and [123]tetramantane deposited onto Au(111). Significant differences in IRSTM spectra for these two isomers demonstrate the power of IRSTM to differentiate individual chemical species and to determine molecular vibrational properties in different surface environments. Our analysis of tetramantane IRSTM spectra allows us to conclude that tetramantane vibrational resonances are more strongly affected by intermolecular interactions than by interactions between the tetramantane molecules and the gold surface.

3.2 Infrared Scanning-Tunneling-Microscopy-Based Spectroscopy: Basic Principle

The main idea of IRSTM is to employ an STM tip in tunneling mode to detect the thermal expansion of a sample due to the molecular absorption of tunable, monochromatic IR radiation. When a bare crystal is irradiated, thermal expansion of the crystal in the direction perpendicular to its surface can be measured by monitoring the motion of an STM tip in constant-current mode. When the surface is covered by adsorbed molecules, however, a new absorption channel appears whenever the wavelength of light is tuned to a molecular vibrational resonance. Excited vibrational states of a molecule typically relax in $\sim 10\,\mathrm{ps}$ [82] and the associated energy is transferred to the substrate. Therefore, the extra expansion (the

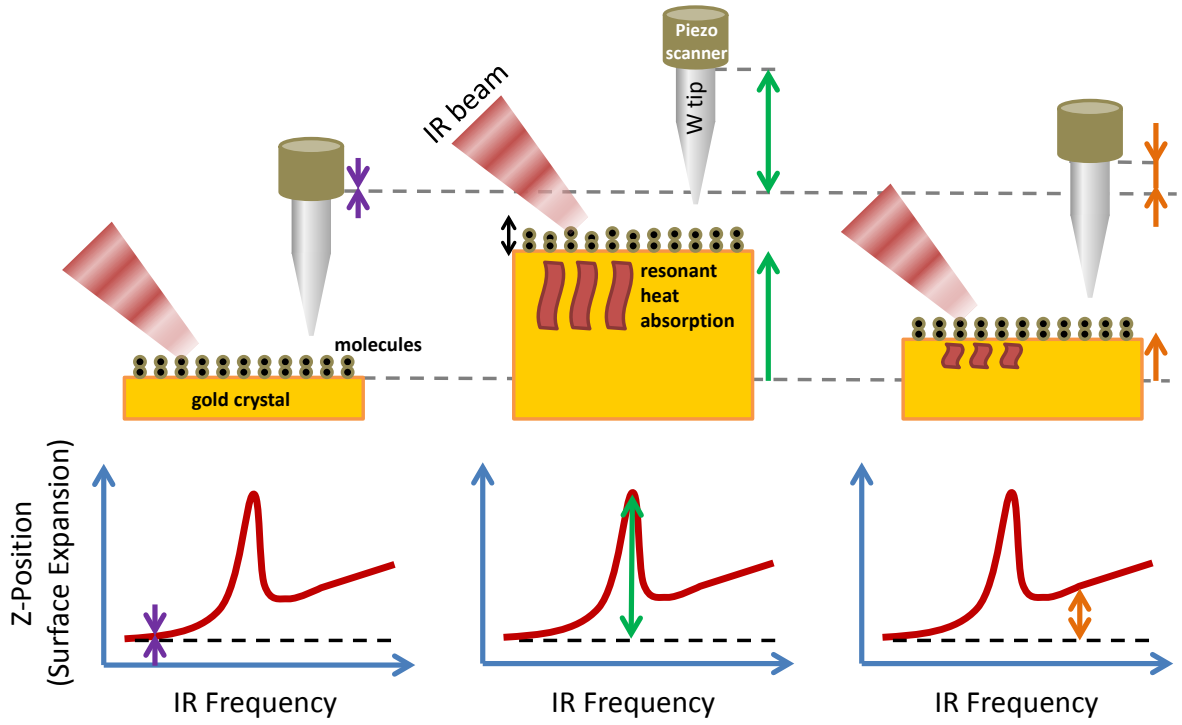

Figure 3.1: Schematic illustration of the IRSTM operating principle. When a crystal is irradiated, thermal expansion of the crystal in the direction perpendicular to its surface can be measured by monitoring the motion of an STM tip in constant-current mode. In the left panel, the frequency of the IR light does not excite any vibrational modes of the adsorbates. However, when the frequency of the IR light is tuned to a vibrational resonance (middle panel) a new light absorption channel appears: the molecules absorb the IR light and the associated energy is transferred to the substrate. The extra expansion at a given IR frequency characterizes the molecular absorption at this wavelength.

difference between the surface expansion with and without molecules) at a given wavelength yields the molecular absorption at this wavelength. A spectroscopy measurement for the case when the crystal is covered by adsorbed molecules is schematically illustrated in Figure 3.1.

3.3 Infrared Scanning-Tunneling-Microscopy-Based Spectroscopy: Instrumentation

IR excitation of the tetramantane/Au(111) surface was performed using a homemade tunable mode-hop-free laser. The main components of the tunable IR laser are schematically shown in Figure 3.2. A singly resonant optical parametric oscillator (OPO) based on periodically poled MgO-doped lithium niobate was employed to down-convert the light frequency from

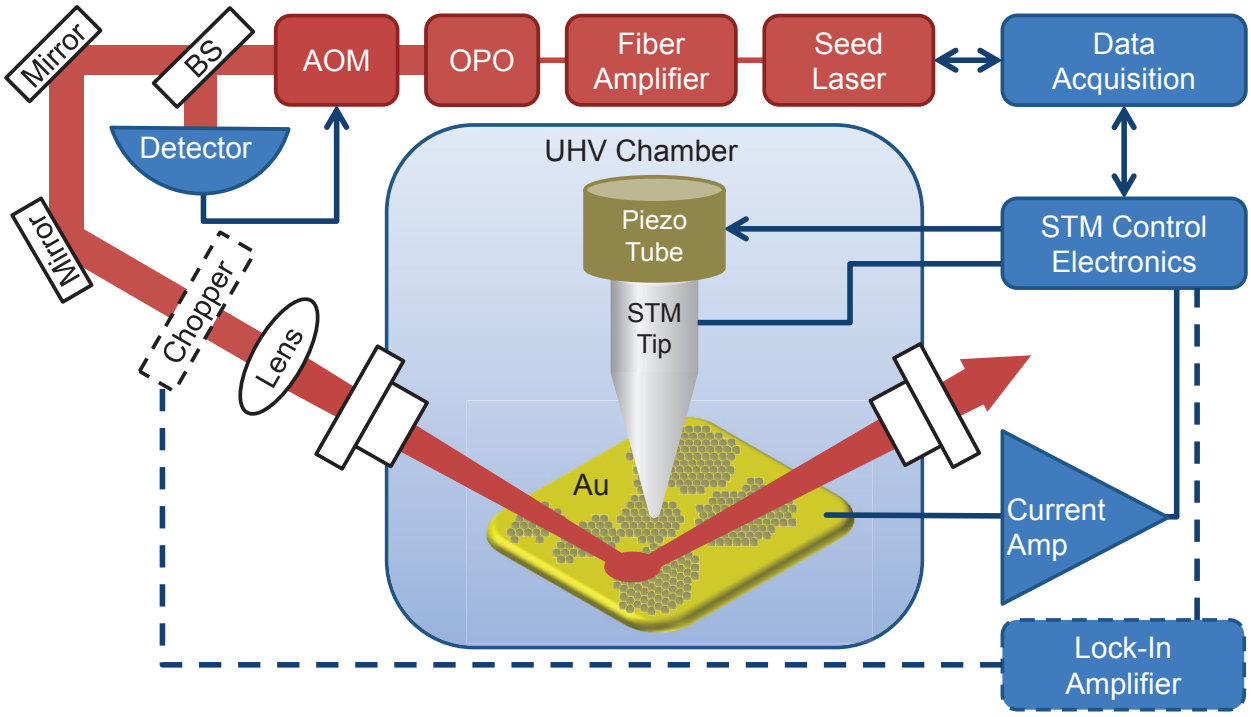

Figure 3.2: Experimental setup combining a tunable IR laser and a UHV STM. The IR light intensity is stabilized by a feedback loop consisting of an acousto-optical modulator (AOM), a beam splitter (BS), and a diode detector. The IR light was directed into the STM as described in the text. A lock-in amplifier and chopper were used for AC measurements.

a pump laser. The pump laser consists of an external cavity laser diode as a seed laser light source and an optical amplifier. Pump tuning with synchronous periodically poled MgO-doped lithium niobate temperature control was used to deliver continuous frequency tuning of the IR OPO output as reported elsewhere [83]. A feedback loop was used to stabilize the IR light intensity at the OPO output to suppress fluctuations down to about 0.5% of the overall intensity. The laser beam (total power $\sim 30\,\mathrm{mW}$) was guided into the UHV STM chamber through a CaF_2 viewport. The beam was converged via an external lens to achieve a spot size of 1.2 mm diameter on the sample. The beam center was intentionally targeted to a point on the surface 0.8–1.5 mm away from the STM junction. This was done to avoid direct light excitation of the tip-sample tunnel junction, thus eliminating the effects of tip thermal expansion, rectification, and thermoelectric current generation [84]. Under these conditions no significant difference, apart from overall amplitude variation, was found between IRSTM spectra taken at different lateral distances between the laser spot and the tunnel junction, or with different laser spot sizes.

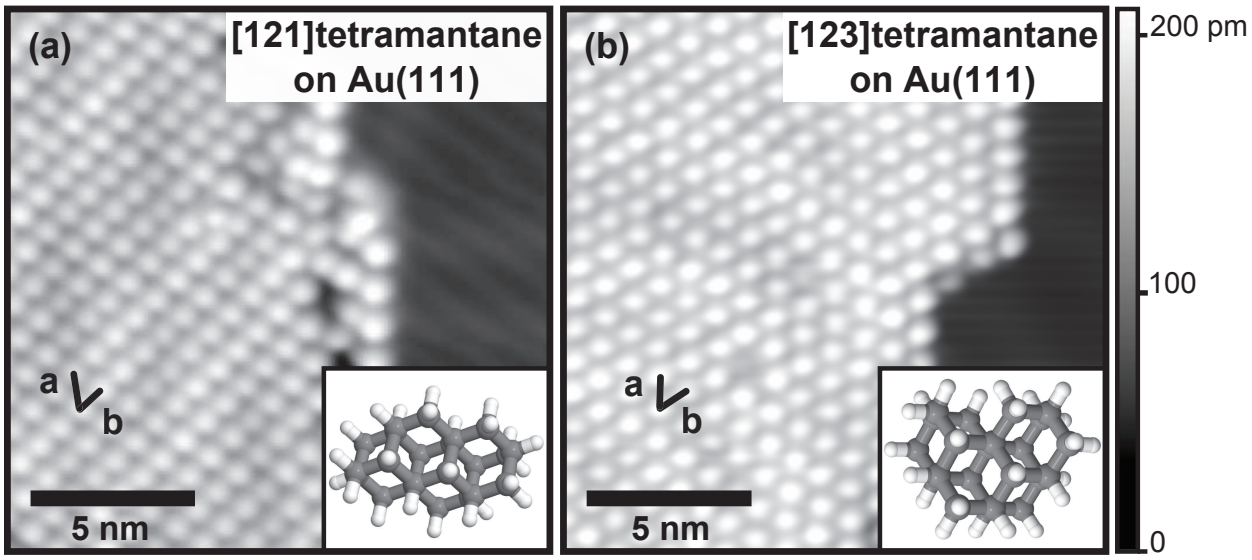

Figure 3.3: (a) STM topography of [121]tetramantane molecules on Au(111) ($V_{\text{sample}} = 1.0\,\text{V}$, $I = 50\,\text{pA}$, $T = 13\,\text{K}$). The molecular lattice has an oblique structure with lattice constants $|\mathbf{a}| = 11.1 \pm 0.1\,\text{Å}$, $|\mathbf{b}| = 8.3 \pm 0.1\,\text{Å}$, and an interior angle of $59° \pm 1°$. The inset shows a model of [121]tetramantane (gray and white balls represent carbon and hydrogen atoms). (b) STM topography of [123]tetramantane on a Au(111) surface ($V_{\text{sample}} = -2.0\,\text{V}$, $I = 100\,\text{pA}$, $T = 13\,\text{K}$). Within experimental resolution [123]tetramantane molecules form a hexagonal structure with $|\mathbf{a}| = |\mathbf{b}| = 9.8 \pm 0.1\,\text{Å}$. The inset shows a model of P [123]tetramantane (our [123]tetramantane/Au(111) samples were prepared from a racemic mixture containing P and M enantiomers).

3.4 Scanning Tunneling Microscopy of Tetramantane on Au(111)

Tetramantane molecules at coverages of less than one monolayer on a Au(111) surface were studied by STM and IRSTM. [121]tetramantane [inset of Figure 3.3(a)] and [123]tetramantane [inset of Figure 3.3(b)] were chosen because they are structural isomers described by the same chemical formula $C_{22}H_{28}$, and also because [121]tetramantane on Au(111) exhibits a pronounced CH stretch mode that has been previously observed using STM-IETS [38]. The molecules were extracted from petroleum and purified into powder form [85]. The powders were sublimated in vacuum at temperatures in the range of 30 °C–34 °C onto a clean Au(111) surface held at room temperature, resulting in coverages ranging from 0.5 to 1.0 monolayer (ML). STM measurements were performed at $T = 13$–$15\,\text{K}$. Figures 3.3(a) and 3.3(b) show typical STM images of [121]tetramantane/Au(111) and [123]tetramantane/Au(111), respectively. The two molecules look similar in their topography, although the [121]tetramantane packaging is slightly elongated in the direction of the molecular lattice

vector labeled **a** [Figure 3.3(a)].

3.5 Infrared Scanning-Tunneling-Microscopy-Based Spectra of Tetramantane on Au(111)

IRSTM spectra were measured via two different modes: with optical chopping of the laser light (AC mode) and without optical chopping (DC mode). Figure 3.4(a) shows the IRSTM spectrum of a single monolayer of [121]tetramantane measured using the AC mode. Here the differential STM Z signal was measured under constant-current feedback conditions (via lock-in detection at the chopping frequency) while sweeping the IR excitation from 2830 to 2940 cm^{-1}. The same measurement was performed on bare Au(111) as a reference. Six IR absorption peaks can clearly be seen for [121]tetramantane/Au(111) compared to the bare Au(111) spectrum at 2850 ± 1, 2855 ± 1, 2881 ± 1, 2897 ± 1, 2909 ± 1, and $2920 \pm 1\,\mathrm{cm}^{-1}$. The appearance of these peaks indicates a larger thermal expansion amplitude at the corresponding IR frequencies and, therefore, can be attributed to extra energy absorption by [121]tetramantane vibrational modes at these frequencies. The ratio of the peak heights [$\sim 7 \times 10^{-4}$ Å for the major peaks shown in Figure 3.4(a)] to the background level [$\sim 1 \times 10^{-2}$ Å in Figure 3.4(a)] corresponds to the relative absorption of the [121]tetramantane monolayer compared to the bare gold absorption. Assuming that polished gold at low temperatures absorbs $\sim 1\,\%$ of incoming IR light [86, 87], the ratio of the major peak height to the background level yields a molecular absorption coefficient of $\sim 0.07\%$ for one monolayer of [121]tetramantane. This corresponds to an absorption cross section of $\sim 6 \times 10^{-18}\,\mathrm{cm}^2$ per molecule.

We also performed IRSTM measurements of [121]tetramantane using the DC mode (a measurement with no optical chopping). This is a simpler measurement than the AC mode, since the AC mode requires low optical chopping frequencies and long lock-in time constants. Figure 3.4(b) shows the DC IRSTM spectrum of 0.7 ML of [121]tetramantane on Au(111), as well as a bare Au(111) reference spectrum. The [121]tetramantane/Au(111) spectrum shows peaks relative to the bare Au(111) spectrum at the same energy positions as in Figure 3.4(a). These peaks are therefore attributed to extra light absorption by [121]tetramantane molecules. The DC IRSTM spectra reflect the same information as AC spectra, but the peak amplitude is harder to quantitatively interpret due to the lack of a well-defined overall absorption reference point (i.e., such as the bare gold absorption). The DC spectra are also more strongly affected by unavoidable drifts in the experimental setup. These drifts are caused by redistribution of the thermal fluxes inside the STM due to the fact that the tip-sample temperature equilibrium depends very sensitively on parameters such as sample orientation, beam path, and laser power stability. We note, however, that after a baseline subtraction (i.e., subtraction of a third order polynomial fit to the estimated bare Au(111) contribution to the spectrum) the vibrational spectra look very similar for both AC and DC measurement modes.

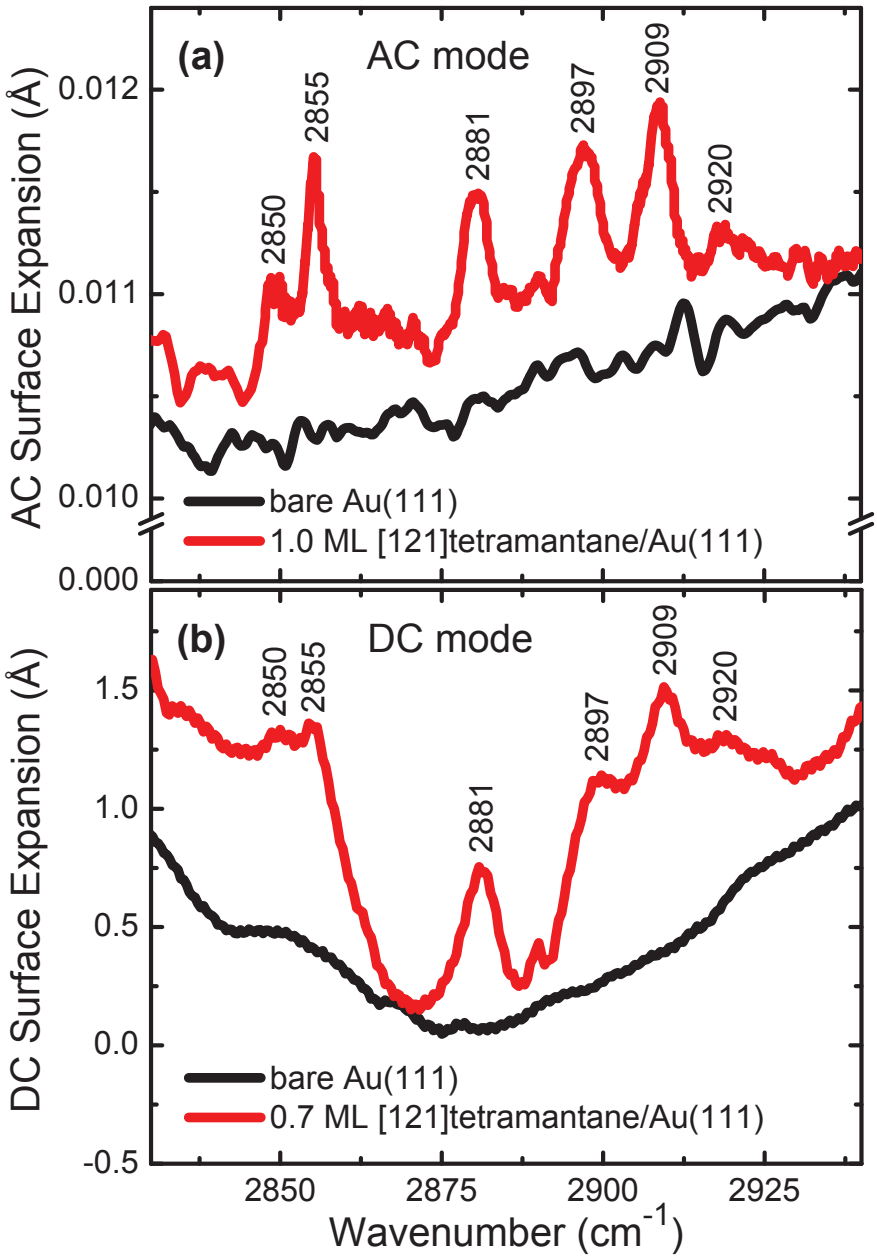

Figure 3.4: (a) Differential AC surface expansion due to absorption of modulated IR light, measured via lock-in amplifier for constant-current STM Z signal (chopper modulation frequency $\sim 13\,\mathrm{Hz}$, lock-in amplifier time constant 3 s). The black (lower) and red (upper) lines show AC surface expansion of bare gold and [121]tetramantane-decorated gold, respectively. (b) DC surface expansion of bare gold (black lower line) and [121]tetramantane-decorated gold (red upper line) as a function of incident IR frequency, measured via constant-current STM Z signal.

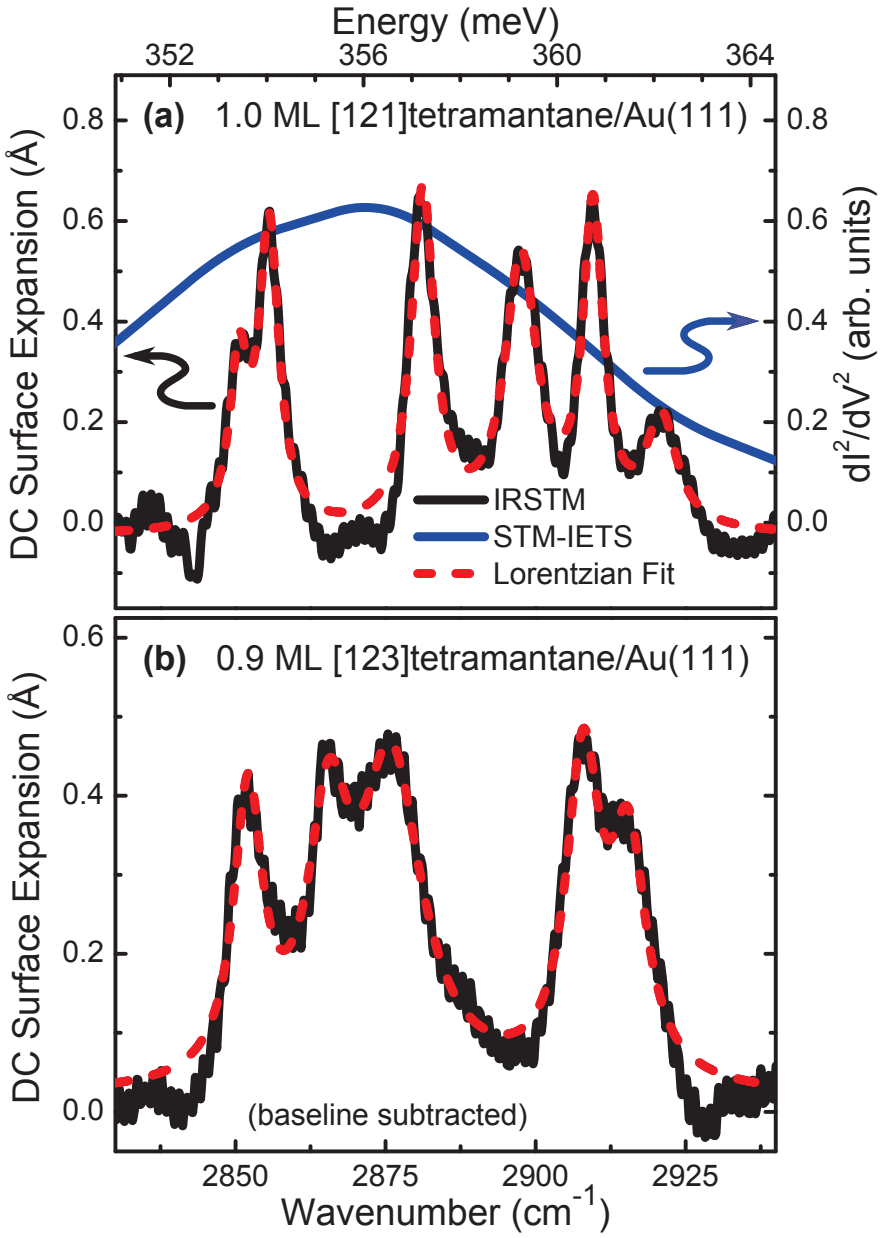

Figure 3.5: DC surface expansion due to molecular IR absorption as a function of incident IR frequency. (a) The black solid line shows the average DC surface expansion of [121]tetramantane/Au(111) (five sweeps) with gold baseline signal subtracted. The blue solid line (with a single broad peak) shows an STM d^2I/dV^2 spectrum of [121]tetramantane/Au(111) from Reference 38. (b) The black solid line shows the average DC surface expansion of [123]tetramantane/Au(111) (twelve sweeps) with gold baseline signal subtracted. The red dashed lines are (a) six-peak and (b) five-peak Lorentzian fits to the experimental data.

In order to demonstrate the potential of IRSTM for chemical characterization, IRSTM spectroscopy was additionally performed on samples of [123]tetramantane. As seen in Figure 3.3, both molecular species form similar self-assembled overlayer structures on Au(111). Figure 3.5 shows DC IRSTM spectra of 1 ML of [121]tetramantane on Au(111) versus 0.9 ML of [123]tetramantane on Au(111) (after baseline subtraction). The two spectra are clearly distinct from each other, and both exhibit several well-resolved peaks. Peak energies were extracted by fitting Lorentzian lines to the spectra [fits can be seen in Figure 3.5]. [123]tetramantane/Au(111) vibrational peaks are found at 2852 ± 1, 2866 ± 1, 2876 ± 1, 2908 ± 1, and $2915 \pm 1\,\mathrm{cm}^{-1}$, while the [121]tetramantane/Au(111) peaks are seen at 2850 ± 1, 2855 ± 1, 2881 ± 1, 2897 ± 1, 2909 ± 1, and $2920 \pm 1\,\mathrm{cm}^{-1}$. This illustrates the power of IRSTM to distinguish submonolayer amounts of even closely related chemical compounds.

3.6 Discussion

It is instructive to discuss some differences between IRSTM spectroscopy and STM-IETS. Figure 3.5(a) shows a d^2I/dV^2 spectrum of [121]tetramantane/Au(111) from Reference 38 (the blue line having only one broad peak). The IETS peak (obtained at the lower temperature of $T = 7\,\mathrm{K}$ with bias modulation voltage amplitude $V_\mathrm{m} = 1$–$10\,\mathrm{mV}$) is much broader in energy and cannot resolve any of the multiple CH stretch modes that exist in this energy range. Since IETS energy resolution depends on temperature and bias modulation voltage amplitude [88], the IETS spectral resolution in Reference 38 is estimated to be $30\,\mathrm{cm}^{-1}$ at best. In contrast, the energy resolution for IRSTM is determined by the spectral accuracy of the laser. For tunable IR lasers the spectral uncertainty mainly arises from mode hops which cause sudden changes in the frequency of emitted light. The laser used here was found to be nearly free of mode hopping over the scanned frequency range from 2830 to $2940\,\mathrm{cm}^{-1}$ (an average of three hops occurs per scan, each of magnitude $< 1\,\mathrm{cm}^{-1}$) [83]. We therefore conservatively estimate the spectral resolution of IRSTM to be no worse than $1\,\mathrm{cm}^{-1}$ across the frequency range explored here. It should be noted that IRSTM also differs from STM-IETS in that IRSTM probes IR active vibrational modes with the dipole moment perpendicular to the metal surface, while STM-IETS active modes do not obey rigorous selection rules [89, 90].

The linewidths observed using IRSTM carry information regarding molecular interactions. Our tetramantane/Au(111) linewidths were found to be in the range of 4–$12\,\mathrm{cm}^{-1}$ (full width at half maximum), corresponding to vibrational lifetimes in the range of 0.4–1.3 ps. Our experimental energy resolution ($\leq 1\,\mathrm{cm}^{-1}$) and the homogeneity of our samples imply that this broadening is not instrumental but is rather due to molecule-molecule and molecule-substrate interactions (as well as possibly overlapping modes). We observed notably less broadening of tetramantane CH stretch modes for molecules on Au(111) compared to previously measured powder samples (typical widths for the powder measurements reported in Reference 91 are on the order of 10–$20\,\mathrm{cm}^{-1}$). Two main factors likely account for this difference: measurement temperature (13–15 K for the surface measurements versus

room temperature for the powder measurements) and structural differences between surface and bulk systems. Regarding structure, our surface measurements were performed on well-ordered adlayers, while the spectra reported in Reference 91 were obtained on powders lacking perfect crystalline order. Inhomogeneous broadening of the vibrational peaks in the powders is thus expected to be larger than in monolayers on Au(111). Other aspects of the local environment, such as the number of nearest neighbors and the relative coupling strengths between them, can also affect peak broadening. Molecules arranged in two-dimensional lattices (as measured here) are surrounded by a smaller number of nearest neighbors and so can be expected to exhibit smaller broadening compared to the three-dimensional environment experienced by molecules in a powder. Interaction of molecules with a metal substrate, on the other hand, is expected to broaden peaks. Since we see an overall narrowing of vibrational peak widths compared to bulk measurements, we conclude that the narrowing effects of lower temperature and reduction in coordination dominate over the broadening effects of the molecule-surface interaction.

Further information regarding molecule-molecule interactions can be inferred by comparing IRSTM measurements to bulk measurements performed on powder samples. Peaks at notably different energies are observed in bulk powders of different tetramantane isomers, specifically at 2840, 2863, 2884, and 2901 cm^{-1} for [121]tetramantane and at 2847, 2871, and 2903 cm^{-1} for [123]tetramantane [91]. There is not a perfect one-to-one correspondence between these bulk vibrational modes and the adsorbate modes reported here, but the peaks for the surface measurements do appear overall to be shifted to higher frequencies. We assume this is not due to mechanical renormalization [92] since the molecules are not strongly bonded to the metal surface [38]. Furthermore, neither chemical nor electrostatic shifts are expected to be significant since tetramantane molecules have a large gap between the highest occupied and lowest unoccupied molecular levels, and therefore very little charge transfer between molecules and the gold surface is expected to occur [38]. Two mechanisms that might be at work here are the coupling of dynamic molecular dipole moments to substrate image charges (a redshifting effect) and dynamic dipole-dipole coupling between molecules (a blueshifting effect) [92]. The fact that the vibrational peaks for surface-adsorbed molecules tend to be blueshifted relative to the peaks for powder samples implies that intermolecular dipole-dipole coupling for the surface samples plays a more important role than coupling of the dynamic dipole moments to their images in the substrate. This is consistent with recent observations of appreciable attractive van der Waals interactions in diamondoid dimer structures [93, 94].

3.7 Conclusion

In conclusion, we have demonstrated the feasibility of IRSTM for performing IR spectroscopic studies of molecular submonolayers on metallic surfaces by combing a tunable IR laser and an STM. We have shown that the excellent spectral resolution of IRSTM can be used for chemical characterization of molecular adlayers, as well as for measurements of single-

molecule optical absorption cross sections. IRSTM measurements of tetramantane molecules on gold reveal that adsorbed tetramantane vibrational peaks are narrowed and blueshifted relative to bulk measurements, implying that intermolecular interactions for adsorbed tetramantane have a stronger influence on molecular vibrational resonances than the interaction between tetramantane molecules and the gold surface. Regarding the ultimate sensitivity of this new technique, we believe that lasers with better intensity stabilization and substrates with an increased thermal expansion coefficient (such as based on a bimetallic strip principle) could significantly improve the IRSTM sensitivity compared to the sensitivity achieved in this work.

Chapter 4

Vibrational Properties of Adamantane on Au(111)

In this chapter both theoretical and experimental studies of the infrared spectrum of an adamantane monolayer on a Au(111) surface are presented. Using the scanning tunneling microscopy-based infrared spectroscopy technique described in Chapter 3 we were able to measure both the nanoscale structure of an adamantane monolayer on Au(111) as well as its infrared spectrum, while density-functional-theory-based *ab initio* calculations allowed us to interpret the microscopic vibrational dynamics revealed by our measurements. We found that the infrared spectrum of an adamantane monolayer on Au(111) is substantially modified with respect to the gas-phase infrared spectrum. The first modification is caused by the adamantane-adamantane interaction due to monolayer packing and it reduces the infrared intensity of the $2912\,\mathrm{cm}^{-1}$ peak (gas phase) by a factor of 3.5. The second modification originates from the adamantane-gold interaction and it increases the infrared intensity of the $2938\,\mathrm{cm}^{-1}$ peak (gas phase) by a factor of 2.6, and reduces its frequency by $276\,\mathrm{cm}^{-1}$. We expect that the techniques described here can be used for an independent estimate of substrate effects and intermolecular interactions in other diamondoid molecules, and for other metallic substrates.

This chapter is adapted with permission from Y. Sakai et al., "Intermolecular interactions and substrate effects for an adamantane monolayer on a Au(111) surface", Phys. Rev. B **88**, 235407 (2013). Copyright 2013 American Physical Society.

4.1 Introduction

Diamondoids form a class of hydrocarbon molecules composed of sp^3 hybridized carbon atoms. They can be regarded as small pieces of diamond whose dangling bonds are terminated with hydrogen atoms. Diamondoids are known to exhibit negative electron affinity and have potential to be used in future applications as electron emitters [96, 97] and as building blocks for other nanoscale devices [38]. Diamondoids have also attracted much in-

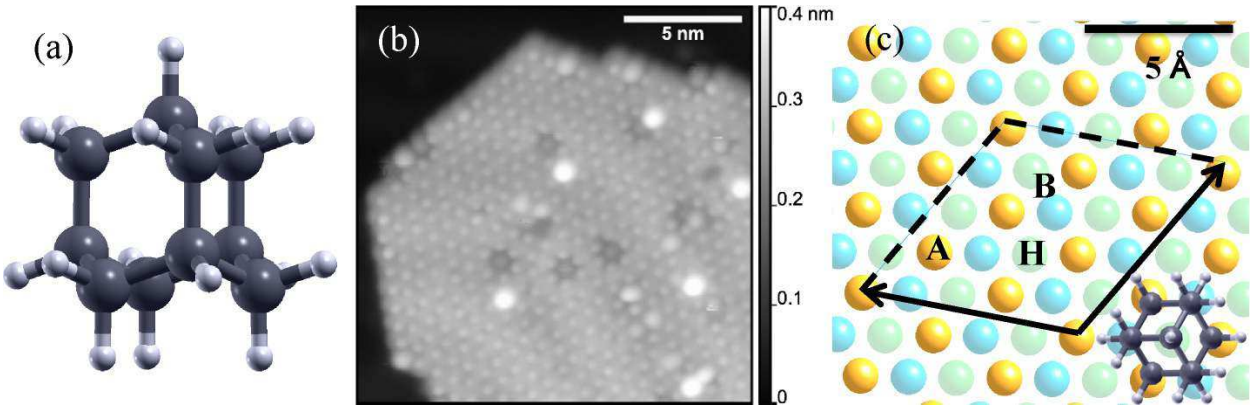

Figure 4.1: (a) Model of molecular structure of an adamantane molecule. Hydrogen and carbon atoms are represented by white and gray spheres, respectively. (b) STM topography of a self-assembled island of adamantane molecules on a Au(111) surface (sample bias $V_{\text{sample}} = -1.0\,\text{V}$, current setpoint $I = 100\,\text{pA}$, temperature $T = 13\,\text{K}$). (c) Schematic picture of alignment of the molecules on the Au(111) surface. Gold atoms in the topmost layer, second layer, and third layer are represented by gold, blue, and green color spheres of different shades. Black lines show the supercell of the $\sqrt{7} \times \sqrt{7}$ molecular alignment. Upper case letters indicate the location of adsorption sites: A for *atop* site, B for *bridge* site, and H for *hollow* site. Top view of an adamantane in the *hollow-atop* geometry is also illustrated [the center of the molecule is in the *hollow* site and the three bottom hydrogen atoms are in the *atop* site; the three bottom hydrogen atoms can be seen at the bottom of Figure 4.1(a), but not be seen in Figure 4.1(c)].

terest because of their possible appearance in the interstellar medium [98, 99]. The smallest diamondoid is adamantane ($C_{10}H_{16}$), which has a highly symmetric cage-like structure (T_d point group) illustrated in Figure 4.1(a). Various theoretical and experimental results on IR spectroscopy of both gas and solid adamantane have been reported in the literature [99–107]. Self-assembled monolayers of larger diamondoids than adamantane (i.e. tetramantane) on a Au(111) surface system has been studied with scanning tunneling microscopy in Section 3.4 of this dissertation and in Reference 38. The IR spectrum of a functionalized adamantane on a Au(111) surface has been studied by Kitagawa et al. [108]; however the functionalization prevents adamantane molecules from being in direct contact with the Au(111) surface. Therefore a detailed characterization of the adamantane monolayer-gold surface interaction is missing.

In this chapter we investigate a submonolayer of adamantane in direct contact with a Au(111) surface. We present experimentally obtained the IR spectrum of a self-assembled adamantane submonolayer on a Au(111) surface by using IRSTM, a technique which combines IR spectroscopy and scanning tunneling microscopy as described in Chapter 3. The observed spectrum of the adamantane monolayer on Au(111) is significantly altered with respect to the gas and solid phase of adamantane. To account for this difference theoreti-

cally, we study the IR spectrum within the framework of density functional theory (DFT) and density functional perturbation theory. Our analysis reveals that intermolecular and molecule-substrate interactions cause mixing (hybridization) of the gas-phase vibrational modes. As a result, IR active vibrational modes of adamantane molecules on a gold substrate are found to be considerably different than those of the gas phase. For example, our calculations show that the intermolecular interaction in the adamantane monolayer reduces the IR intensity of one of the gas-phase IR peaks by a factor of 3.5. In addition, the interaction between adamantane molecules and the Au(111) substrate increases the IR intensity of another gas-phase mode by a factor of 2.6 and causes a significant redshift of $276\,\mathrm{cm}^{-1}$ for this mode.

This chapter is organized as follows: in Section 4.2, the details of our experiment are described. In Section 4.3 the computational methods are introduced. In Section 4.4 the theoretical and experimental IR spectra are described and analyzed. In Sections 4.4.2, 4.4.2 and 4.4.2 we study theoretically the IR spectrum of a single adamantane molecule, the IR spectrum of an adamantane monolayer, and the IR spectrum of an adamantane monolayer on a Au(111) surface, respectively. In Section 4.4.3 we compare experimental and theoretical IR spectra. Finally, the conclusions are given in Section 4.5.

4.2 Experimental Methods

Adamantane (Sigma-Aldrich, purity $\geq 99\%$) was deposited onto a clean Au(111) surface using a source consisting of adamantane powder contained in a sealed glass tube (the surface was exposed to adamantane vapor at room temperature through a precision leak valve between the adamantane source and the main vacuum chamber). In order to improve the adamantane vapor quality, the sealed tube containing the adamantane powder was passed through five pump/purge cycles utilizing argon as a purge gas. Before the deposition, it was necessary to precool a freshly cleaned gold crystal to 15 K to facilitate adsorption of the molecules onto the Au(111) surface. The precooled gold crystal was then transferred into a chamber with base pressure of $\sim 1 \times 10^{-11}$ Torr where the crystal was held in a room temperature manipulator during the adamantane deposition which lasted for about ten minutes (pressure rose to $\sim 1 \times 10^{-9}$ Torr when the adamantane valve was opened for deposition). After the deposition, the sample was immediately transferred into the scanning tunneling microscope operating at $T = 13$–15 K for STM surface characterization. The adamantane molecules on Au(111) were observed to self-assemble into hexagonally packed molecular islands with a lattice constant of 7.5 ± 0.2 Å. Figure 4.1(b) shows a typical STM image of an adamantane island on a Au(111) surface.

IR absorption spectra of adamantane submonolayers on the Au(111) surface were obtained by using IRSTM. The detailed description of the IRSTM technique and the discussion of its performance were given in Chapter 3. Here we briefly note that IRSTM employs an STM tip in tunneling mode as a sensitive detector to measure the thermal expansion of a sample due to molecular absorption of monochromatic IR radiation [68, 109]. The surface

thermal expansion of the sample, recorded as a function of IR frequency, yields the IR molecular absorption spectrum. Frequency-tunable IR excitation of the samples can be achieved by using a tunable mode-hop-free laser source based on a singly resonant optical parametric oscillator [83].

4.3 Theoretical Calculations

4.3.1 Geometry of Adamantane on Au(111)

We start with a discussion of the orientation of an adamantane monolayer on the Au(111) surface as shown in Figure 4.1. Based on the STM topography shown in Figure 4.1(b), we modeled the molecular arrangement on a Au(111) surface. In our model, the adamantane molecules are arranged in a $\sqrt{7} \times \sqrt{7}$ structure as shown in Figure 4.1(c). The intermolecular distance in this model is 7.40 Å, which is close to the observed intermolecular distance 7.5 ± 0.2 Å. In our calculations we placed the adamantane molecules in the way that the threefold axis of the molecule is perpendicular to the surface, with three bottom hydrogen atoms facing down towards the Au(111) surface. Because of its threefold symmetry, this configuration is compatible with the hexagonal self-assembled island seen in the STM topography Figure 4.1(b).

We determined the most stable adsorption geometry of adamantane by computing the total energy for various adsorption sites. We performed *ab initio* total energy calculations within the framework of DFT [110, 111] to understand the properties of an adamantane monolayer on a Au(111) surface. We used the local density approximation (LDA) for the exchange and correlation energy functionals based on the quantum Monte Carlo results of Ceperley and Alder [112] as parameterized by Perdew and Zunger [113]. Vanderbilt ultrasoft pseudopotentials [114] were adopted in combination with a plane wave basis with cut off energies of 30 and 360 Ry for the wavefunctions and charge density, respectively. A Brillouin zone integration was done on an $8 \times 8 \times 1$ uniform k-grid. Gaussian smearing with a 0.01 Ry width was used for the calculation of metallic systems. The Quantum ESPRESSO was used package [115] to perform DFT calculations and XCrySDen [116] was used to visualize the results.

We modeled the Au(111) surface by a finite slab with a thickness of seven gold layers with seven gold atoms in each layer in a supercell geometry [117]. The primitive unit cell of the slab included one adamantane molecule. Therefore, in total the primitive unit cell contained 75 atoms. The width of the vacuum region was 15.5 Å.

Binding energies and molecule-surface distances of four different optimized geometries are listed in Table 4.1. The name of each geometry is based on the position of the center of the molecule and the positions of the three bottom hydrogen atoms shown in Figure 4.1(a). In the most stable geometry (*hollow-atop*) the center of the molecule is on the *hollow* site and three hydrogen atoms are close to the gold atoms in the topmost layer [see Figure 4.1(c)].

Table 4.1: Theoretical binding energies and surface-molecular distances of several adsorption geometries obtained within the LDA approximation. The binding energies in the Table are computed as the sum of the total energy of the gold slab and the isolated adamantane molecule minus the total energy of an adamantane adsorbed on a Au(111) surface system. The convention for the binding sites of Au(111) (*atop*, *bridge*, *hollow*) is as in Figure 4.1(c). In our naming convention (for example *atop-bridge*), the first part (*atop*) represents the position of the center of the adamantane molecule, and second part (*bridge*) represents position of the three bottom hydrogen atoms of adamantane.

Geometry	Distance Å	Binding Energy meV/molecule
atop-bridge	2.25	379
atop-hollow	2.25	384
hollow-atop	2.29	490
hollow-hollow	2.32	355

The calculated distance between the bottom hydrogen atoms and the gold surface is 2.29 Å after optimization of the atomic coordinates.

Our structural model does not explicitly include the herringbone reconstruction of the Au(111) surface. Nevertheless, we approximated the effect of the herringbone reconstruction either by slightly compressing the intermolecular distance (by 4%), or by changing the binding geometry. In both cases, we found only a slight change (shift of at most $5\,\mathrm{cm}^{-1}$) of the adamantane IR spectrum.

It is well known that LDA energy functionals do not correctly describe long-range interactions such as the van der Waals (vdW) interaction. Thus we also cross-checked our results with van der Waals density functionals (vdW-DFs) [118–122]. In particular, we used an improved version [119] of the nonlocal vdW correlation functional together with Cooper exchange [120]. We optimized the four different structures to compare the energetics with those of the LDA. After the structural optimization with a vdW functional, the *hollow-atop* geometry remained the most stable configuration although the binding energy differences were reduced compared to the LDA (the binding energy difference between the *hollow-atop* geometry and the *atop-bridge* geometry was reduced from 111 meV/molecule (in LDA) to 44 meV/molecule). In addition, the distance between the molecule and surface using the vdW functional was increased from 2.29 Å (in LDA) to 2.45 Å in the *hollow-atop* geometry. Since both of these changes are not large, we expect that the use of the vdW-DF functionals throughout this study has not qualitatively affected the computed IR spectra.

4.3.2 Phonon and Infrared Intensity Calculations

Next, we describe the methods with which we computed the frequency and IR intensity of the adamantane vibration modes, in various environments (gas, monolayer, and on the

Au(111) substrate).

For this purpose we used density functional perturbation theory as described in Reference 123. All calculations were done only in the Brillouin zone center point (Γ). We define the phonon effective charge of the j^{th} phonon branch as

$$Q^{\alpha}(\omega_j) = \sum_{\beta,s} Z_s^{\alpha\beta} U_s^{\beta}(\omega_j). \tag{4.1}$$

Here $\mathbf{Z}$ is the Born effective charge tensor, $\mathbf{U}(\omega_j)$ is the eigendisplacement vector, and ω_j is the phonon frequency of the j^{th} phonon branch. Cartesian vector components are represented by α and β, while s represents the atom index. The Born effective charge $Z_s^{\alpha\beta}$ is defined as the first derivative of the force F_s^{β} acting on an atom s with respect to the electric field E_{α},

$$Z_s^{\alpha\beta} = \frac{\partial F_s^{\beta}}{\partial E_{\alpha}}. \tag{4.2}$$

The IR intensity of the j^{th} phonon branch can be computed from the phonon effective charge [124]:

$$I_{\text{IR}}(\omega_j) = \sum_{\alpha} \left| Q^{\alpha}(\omega_j) \right|^2. \tag{4.3}$$

Once we obtained the IR intensities $I_{\text{IR}}(\omega_j)$, we modeled the IR spectrum at any frequency ω by assuming a Lorentzian lineshape with a constant linewidth of $10\,\text{cm}^{-1}$ (full width at half maximum). In general, all nine Cartesian components of the Born effective charge must be calculated to obtain the IR intensities. However, on the metallic surface, one can focus only on the components of the electric field perpendicular to the surface ($\alpha = z$) [125–127].

To compute the Born effective charge, we used a finite-difference approximation of Equation 4.2, and we applied the electric field using a saw-tooth like potential in the direction perpendicular to the slab (z). Therefore we were able to obtain the Born effective charge by dividing the force induced by the electric field (ΔF) with the strength of the electric field (E_z).

Using this method we calculated the IR spectra of a single molecule, of a molecular monolayer without a substrate, and of molecules on a Au(111) substrate. To track the changes in the IR spectrum due to intermolecular interaction and due to substrate effects, we performed the following interpolation procedure. We define an interpolated dynamical matrix $\mathbf{D}_{\text{int}}$ and Born effective charge $\mathbf{Z}_{\text{int}}$ between any two configurations A and B as

$$\begin{aligned} \mathbf{D}_{\text{int}} &= (1-\lambda)\mathbf{D}_{\text{A}} + \lambda \mathbf{D}_{\text{B}}, \\ \mathbf{Z}_{\text{int}} &= (1-\lambda)\mathbf{Z}_{\text{A}} + \lambda \mathbf{Z}_{\text{B}}. \end{aligned} \tag{4.4}$$

Here $\mathbf{D}_{\text{int}} = \mathbf{D}_{\text{A}}$ for $\lambda = 0$ and $\mathbf{D}_{\text{int}} = \mathbf{D}_{\text{B}}$ for $\lambda = 1$ and is continuously tuned from A to B for $0 < \lambda < 1$ (same for $\mathbf{Z}_{\text{int}}$). Diagonalizing $\mathbf{D}_{\text{int}}$ for each λ and using interpolated $\mathbf{Z}_{\text{int}}$ we obtained interpolated IR intensity for each λ with $0 < \lambda < 1$.

For the start and end configurations A and B, we use either no subscript, subscript M, or subscript Au to denote either an isolated molecule, molecules in an isolated molecular monolayer, or a monolayer on a Au(111) substrate, respectively. We first interpolated the spectra from the isolated molecule phase to the monolayer phase (M) to determine the effect of the intermolecular interactions. Finally, to estimate the effect of the molecule-substrate interactions, we interpolated the spectrum of the monolayer phase (M) to the case of molecules on the gold substrate (Au). (The case of a single adamantane molecule on the Au(111) surface was not considered, because it would require a too large computational unit cell size.)

In the interpolation procedure, we took into account only dynamical matrix elements of carbon and hydrogen atoms (neglecting the displacements of gold atoms). We found that the effect of gold atom displacements on vibrational frequencies is only $0.3\,\text{cm}^{-1}$ and on the IR intensity less than 10%.

In addition to the interpolation method we also quantitatively analyzed the similarity of eigendisplacement vectors between various configurations. We did this by computing the norm of the inner product $\left|\langle u_i^{\text{A}}|u_j^{\text{B}}\rangle\right|^2$ between i^{th} phonon eigendisplacement vector $\langle u_i^{\text{A}}|$ in configuration A, and j^{th} phonon eigendisplacement vector $|u_j^{\text{B}}\rangle$ in configuration B. We use the same subscript convention as for the interpolation procedure (Au, M, or no subscript for molecules on the substrate, the molecular monolayer, or single molecule case respectively). Since an adamantane molecule consists of 78 phonon modes, we have simplified the analysis by only considering inner products between the 16 predominantly CH stretch modes.

4.4 Results and Discussion

4.4.1 Experimental Infrared Spectra of Adamantane

Figure 4.2 shows an experimentally measured IRSTM spectrum (green line) of 0.8 ML of adamantane adsorbed on a Au(111) surface. The spectrum was obtained by measuring the STM Z signal under constant-current feedback conditions while sweeping the IR excitation from $2840\,\text{cm}^{-1}$ to $2990\,\text{cm}^{-1}$ (the spectrum shown was averaged over 15 frequency sweeps and corrected for background by subtracting a linear fit to the estimated bare gold contribution to the spectrum). Two IR absorption peaks for adamantane/Au(111) can clearly be seen at 2846 ± 2 and $2912 \pm 1\,\text{cm}^{-1}$ in Figure 4.2. The other small peaks seen in Figure 4.2 were not reproducible and thus we were not able to unambiguously relate them to the adamantane absorption. The black dashed lines in Figure 4.2 show the IR peak positions of an adamantane molecule in the gas phase [107]. Comparing the green curve and the black dashed line in Figure 4.2, it is clear that the IR spectrum of adamantane on the Au(111) surface is considerably different from the gas-phase spectrum.

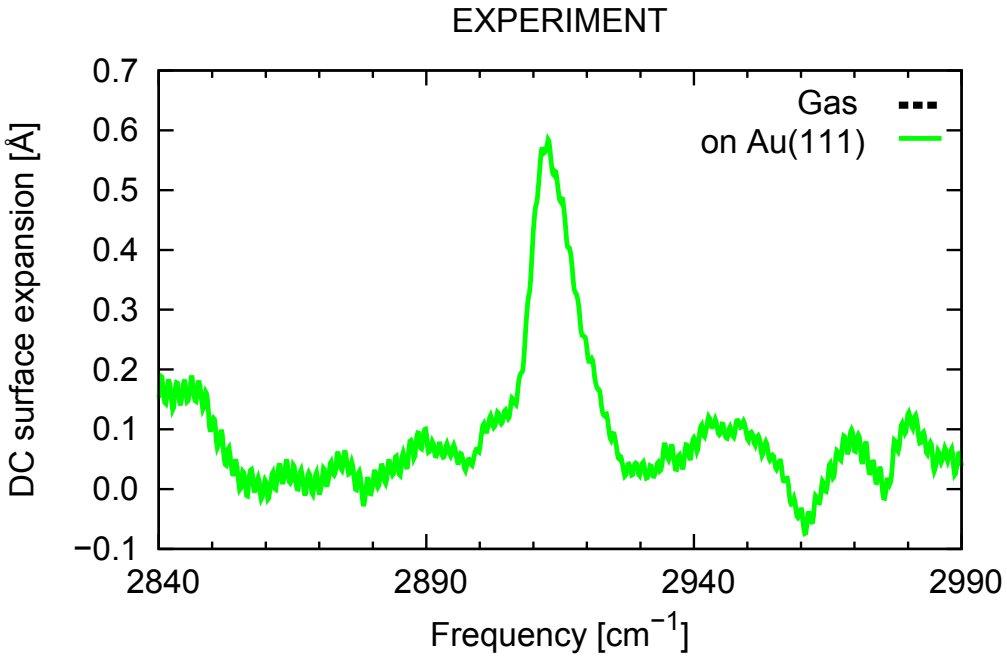

Figure 4.2: The green line shows the experimentally observed spectrum (averaged over 15 sweeps) of 0.8 ML of adamantane on a Au(111) surface with gold baseline signal subtracted. The IR absorption peaks are seen at 2846 ± 2 and $2912 \pm 1\,\mathrm{cm}^{-1}$. The vertical black dashed lines show the IR peak positions of an adamantane molecule in the gas phase as listed in Table 4.2 (2859, 2912, and $2938\,\mathrm{cm}^{-1}$).

4.4.2 Theoretical Analysis of Adamantane Infrared Spectra

To understand the origin of IR spectrum modification of adamantane on Au(111) we computed IR spectra for an isolated adamantane molecule, for an adamantane monolayer, and for an adamantane monolayer placed on the Au(111) substrate. We discuss these three cases in the following three subsections.

Single Molecule

We computed the vibrational frequencies and IR intensities of an isolated single molecule of adamantane by placing the molecule in a large unit cell (length of each side is 16 Å) to minimize the interaction between periodic replicas. The calculated vibrational frequencies of the CH stretch modes (and phonon effective charge) are listed in Table 4.2 and compared with the experimental frequencies from the literature [104, 107]. Our calculation reproduces quite well the vibrational frequencies as compared to the experimental data. We found the largest discrepancy of $\sim 30\,\mathrm{cm}^{-1}$ for two modes (labeled ω_2 and ω_7 in Table 4.2), while the discrepancy for the other modes is only $\sim 10\,\mathrm{cm}^{-1}$.

There are 16 CH stretch modes in adamantane (equal to the number of CH bonds). Out

Table 4.2: Calculated vibrational frequencies (in cm^{-1}) and phonon effective charge Q^z (in elementary charge e) of an isolated adamantane molecule from 2850 to 2950 cm^{-1}. Experimental values are shown for the gas phase [107] and solution phase [104]. We label phonon modes by ω_1–ω_7 with one label corresponding to one irreducible representation (irrep). Only T_2 modes can be observed in the gas IR spectroscopy. A_1, E, and T_2 are Raman active, while T_1 modes are inactive (both in IR and Raman).

	Irrep	Frequency	Q^z	Previous Experiments	
				Reference 107[a]	Reference 104[b]
ω_1	A_1	2924	-	-	2913
ω_2	A_1	2891	-	-	2857
ω_3	E	2892	-	-	2900
ω_4	T_1	2938	-	-	-
ω_5	T_2	2940	0.25	2938	2950
ω_6	T_2	2918	0.32	2912	2904
ω_7	T_2	2892	0.19	2859	2849

[a] IR spectroscopy of gas-phase adamantane.
[b] IR and Raman spectroscopy of adamantane solution. Mode assignment is based on Reference 105.

of 16 modes, there are three modes corresponding to the T_2 irreducible representation, one T_1, one E, and two A_1 modes. In the highly symmetric adamantane molecule (point group T_d) only these three T_2 modes are IR active while other CH stretch modes are IR inactive. The IR active modes have the following approximate characters: asymmetric stretching of the CH_2 bonds (labeled ω_5 in Table 4.2), symmetric CH stretch mode (ω_6), and symmetric CH_2 stretch mode (ω_7). Their eigendisplacement vectors are also shown in Figures 4.3(d), (e), and (f).

The calculated IR spectrum of an isolated adamantane molecule is indicated in Figure 4.4 by a black dashed line. Here we computed only the $\alpha = z$ component of the IR intensities (Equation 4.3) to simplify the comparison with the IR intensities of adamantane in molecular monolayer and monolayer on the Au(111) surface. We obtained three substantial IR absorption peaks of a single molecule of adamantane in the frequency region from 2850 to 2950 cm^{-1}. The highest, middle, and lowest frequency peaks correspond to the ω_5, ω_6, and ω_7 modes, respectively. The ω_6 peak has the largest IR intensity, followed by the ω_5 peak. This order of the IR intensities is consistent with a previous DFT result [106].

Adamantane Monolayer

Before analyzing the IR spectrum of an adamantane monolayer on a Au(111) surface, we first analyzed the IR spectrum of an isolated adamantane monolayer (with the same intermolecular distance as in the monolayer on the gold substrate).

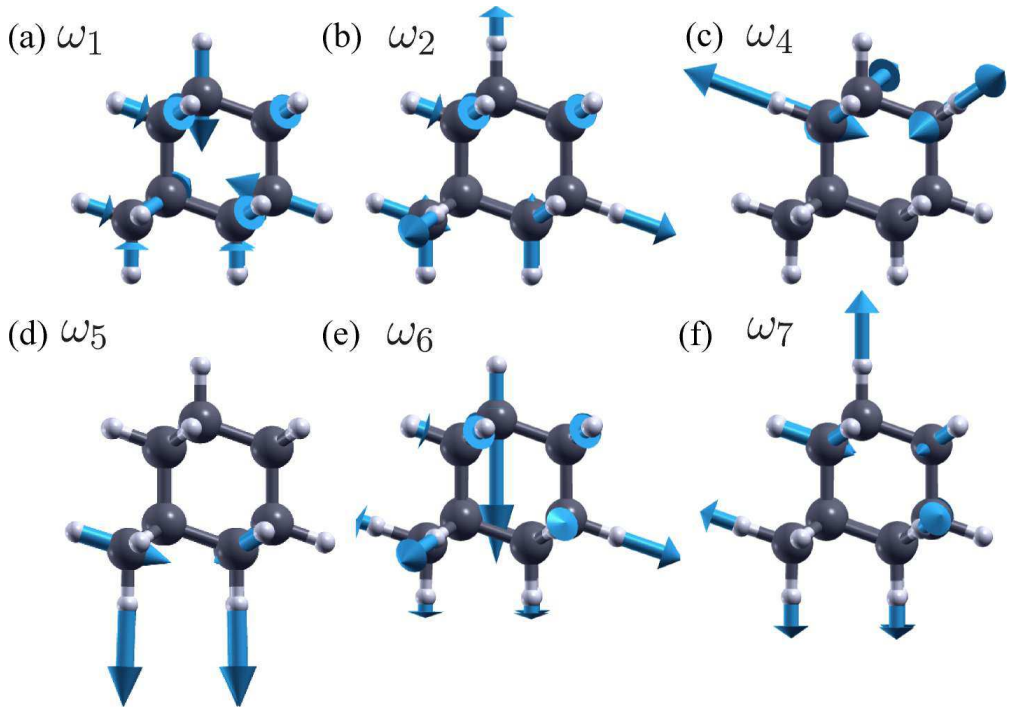

Figure 4.3: Eigendisplacement vectors of (a) ω_1, (b) ω_2, (c) ω_4, (d) ω_5, (e) ω_6, and (f) ω_7 modes of an isolated adamantane molecule (notation is from Table 4.2). Gray and white spheres represent carbon and hydrogen atoms, respectively. Blue arrows indicate the displacements of the atoms (mostly hydrogen atoms). Some of the atoms and eigendisplacements are overlapping since the molecule is shown from a high-symmetry direction.

Table 4.3: Calculated vibrational frequencies (in cm^{-1}), phonon effective charges Q^z (in elementary charge e) of an adamantane monolayer, and and inner products of CH stretch modes of an adamantane monolayer. We label monolayer phonon modes by ω_1^{M}–ω_6^{M} with one label corresponding to one irreducible representation (irrep). Norm of the overlap between gas-phase phonon eigenvector ($\langle u_j|$) and monolayer phonon eigenvector ($|u_i^{\mathrm{M}}\rangle$) is shown, indicating nature of the hybridization of the gas-phase phonons into the monolayer-phase phonons. In the table we have neglected all overlaps whose norm is smaller than 0.1.

	Gas-Phase Overlap							Irrep	Frequency	Q^z
	ω_1	ω_2	ω_3	ω_4	ω_5	ω_6	ω_7			
ω_1^{M}	0.36	.	.	.	.	0.63	.	A_1	2921	0.19
ω_2^{M}	.	0.95	.	.	.	.	.	A_1	2879	0.03
ω_3^{M}	.	.	.	0.99	.	.	.	A_2	2931	-
ω_4^{M}	.	.	.	.	0.90	.	.	A_1	2934	0.22
ω_5^{M}	0.58	.	.	.	.	0.33	.	A_1	2902	0.06
ω_6^{M}	.	.	.	.	.	.	0.94	A_1	2884	0.13

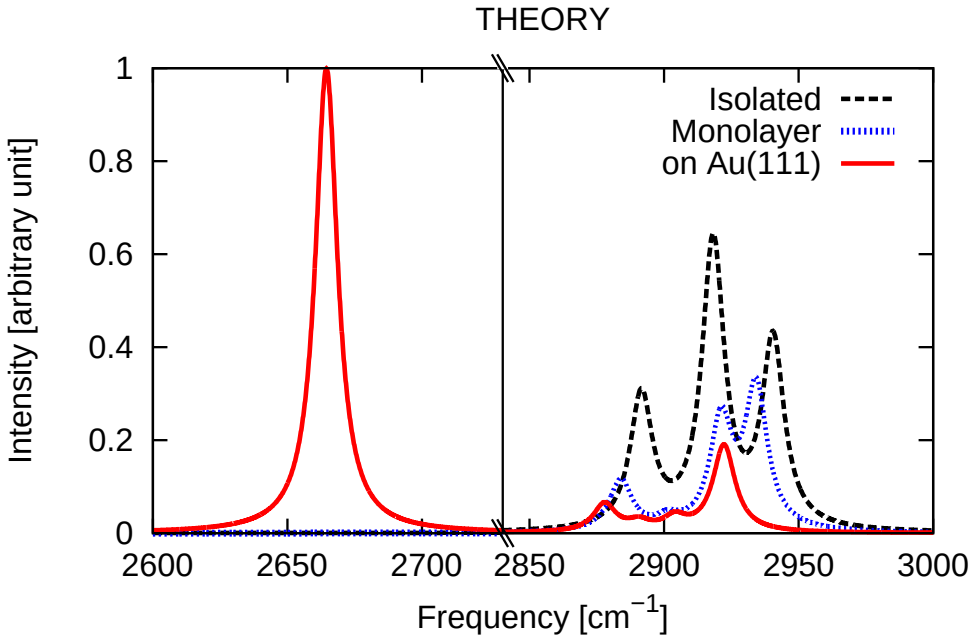

Figure 4.4: Calculated IR spectra of an isolated adamantane molecule (black dashed line), an adamantane monolayer (blue dotted line), and an adamantane monolayer on Au(111) (red solid line). The IR spectra are displayed in arbitrary units (chosen so that the intensity of the IR peak around 2650 cm^{-1} equals 1.0). The black vertical line in the figure separates lower and higher frequency regimes (there are no IR active modes in the intermediate regime between 2730 and 2840 cm^{-1}). Here only the IR spectra close to the CH stretch mode frequencies are shown (the closest IR mode not corresponding to CH stretch is below 1500 cm^{-1}).

Placing adamantane in the monolayer arrangement (see Section 4.3.1) lowers the symmetry of the system from $\mathrm{T_d}$ (in the gas phase) to $\mathrm{C_{3v}}$. This symmetry reduction is followed by splitting of the threefold degenerate $\mathrm{T_2}$ representation (in $\mathrm{T_d}$) to a twofold E representation and a onefold $\mathrm{A_1}$ representation. The basis functions of the E representation are x and y, therefore they have no IR activity in the z direction (perpendicular to the monolayer). In contrast, the modes with $\mathrm{A_1}$ representation are active along the z direction. In addition, symmetry reduction to the adamantane monolayer splits the $\mathrm{T_1}$ representation into E and $\mathrm{A_2}$, both of which are IR inactive in the z direction (E is active in x and y). Therefore, the adamantane monolayer has in total five CH stretch modes that are IR active along the z direction. We label these five modes corresponding to the $\mathrm{A_1}$ representation with ω_1^{M}, ω_2^{M}, ω_4^{M}, ω_5^{M}, and ω_6^{M}.

The blue dashed line in Figure 4.4 shows the calculated IR spectrum of the adamantane monolayer. The changes in the IR spectrum of the adamantane monolayer compared to the

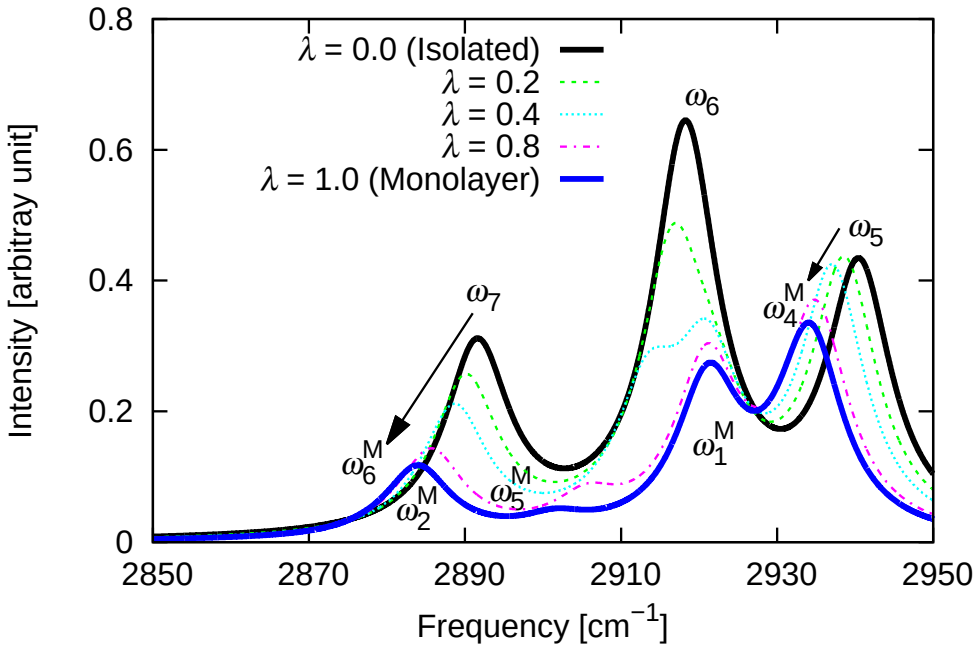

Figure 4.5: Interpolated IR spectra going from an adamantane single molecule (solid black line) to an adamantane monolayer (solid blue line). The dashed ($\lambda = 0.2$), dotted ($\lambda = 0.4$), and chain ($\lambda = 0.8$) lines are interpolated spectra between two cases (using techniques from Section 4.3.2). The arrows indicate the peaks evolution from the isolated molecule case to the monolayer case.

single molecule are presented in more detail in Figure 4.5 and in Table 4.3. Figure 4.5 shows interpolated IR spectra between a single molecule and a molecular monolayer case (using the interpolation method described in Section 4.3.2). Table 4.3 shows the calculated vibrational frequencies, phonon effective charges, and inner products between phonon eigenvectors of gas and monolayer adamantane.

From Figure 4.5 and the inner products in Table 4.3, we found that there is one-to-one correspondence between the ω_2, ω_4, ω_5, ω_7 modes of a single-molecule adamantane phase and the ω_2^{M}, ω_3^{M}, ω_4^{M}, and ω_6^{M} modes of the monolayer adamantane phase, respectively. This correspondence is also evident in the similarity of the phonon eigendisplacement vectors of these two phases [compare Figures 4.3(b), (c), (d), (f) with Figures 4.6(b), (c), (d), (f)]. Three of these modes (ω_2, ω_5, and ω_7) are redshifted by about $10\,\mathrm{cm}^{-1}$ in the monolayer phase (see arrows in Figure 4.5) which is close to the redshifts found in the solid phase diamondoids [99]. The IR inactive mode ω_4 is redshifted by $7\,\mathrm{cm}^{-1}$ in the monolayer phase.

The remaining IR active CH stretch modes in the adamantane monolayer (ω_1^{M} and ω_5^{M}) result from a strong mixing of the ω_1 and ω_6 modes in the gas phase (the inner products shown in Table 4.3 are between 0.33 and 0.63) which also affects their eigendisplacement

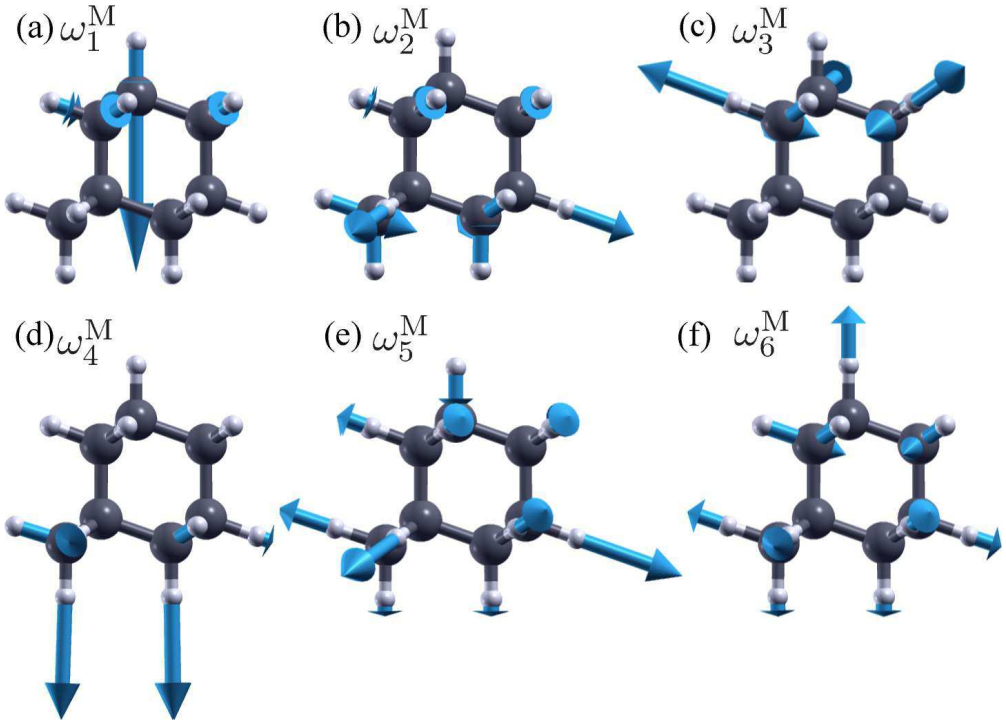

Figure 4.6: Phonon eigendisplacement vectors of (a) ω_1^{M}, (b) ω_2^{M}, (c) ω_3^{M}, (d) ω_4^{M}, (e) ω_5^{M}, and (f) ω_6^{M} modes of an adamantane monolayer without a gold substrate.

patterns [compare Figures 4.3(a) and (e) with Figures 4.6(a) and (e)]. In addition, the ω_5^{M} mode is redshifted by about $20\,\mathrm{cm}^{-1}$ with respect to the ω_1 and ω_6 mode in the gas phase.

Monolayer on Au(111)

Finally, we studied the vibrational properties of an adamantane monolayer on a Au(111) surface. Introduction of the Au(111) surface further reduces the symmetry of the system from C_{3v} (in the monolayer) to C_3. Due to symmetry reductions, both the IR active A_1 mode and the IR inactive A_2 mode having C_{3v} symmetry (monolayer) are changed to the IR active A representation having C_3 symmetry. The IR inactive E modes, remains inactive in the C_3 symmetry along the z direction. The red solid line in Figure 4.4 shows the calculated IR spectrum of a molecular monolayer on a gold substrate. Vibrational frequencies and phonon effective charges are shown in Table 4.4. The most notable difference compared to the spectrum of the isolated adamantane monolayer and gas-phase molecule is the significant redshift of one of the modes ω_6^{Au} (to $2664\,\mathrm{cm}^{-1}$) with a sizable increase in the phonon effective charge (to $0.40\,e$).

Figure 4.7 shows the interpolated IR spectra between the isolated monolayer case and the monolayer on Au(111). This analysis shows that the ω_1^{Au} mode is nearly unaffected by the Au(111) substrate as it originates from the stretching of a topmost CH bond, relatively

Table 4.4: Vibrational frequencies (in cm^{-1}), phonon effective charges Q^z (in elementary charge e), and inner products of CH stretch modes of adamantane molecules on a Au(111) surface. Norm of the overlap between adamantane monolayer-phase phonon eigenvector ($\langle u_j^{\mathrm{M}}|$) and monolayer-on-gold phonon eigenvector ($|u_i^{\mathrm{Au}}\rangle$) is shown, indicating the nature of the hybridization of the gas-phase phonons into the monolayer-phase phonons. In the table we have neglected all overlaps whose norm is smaller than 0.1.

	Monolayer-Phase Overlap						Irrep	Frequency	Q^z
	ω_1^{M}	ω_2^{M}	ω_3^{M}	ω_4^{M}	ω_5^{M}	ω_6^{M}			
ω_1^{Au}	1.00	.	.	.	.	.	A	2922	0.17
ω_2^{Au}	.	0.35	.	.	0.27	0.33	A	2878	0.10
ω_3^{Au}	.	.	1.00	.	.	.	A	2935	0.01
ω_4^{Au}	.	0.34	.	0.21	0.42	.	A	2904	0.06
ω_5^{Au}	.	.	.	.	0.29	0.63	A	2891	0.07
ω_6^{Au}	.	0.27	.	0.70	.	.	A	2664	0.40

far from the Au(111) surface. In fact, the eigendisplacement vectors of the ω_1^{Au} mode and ω_1^{M} mode are nearly the same (compare Figure 4.6(a) and Figure 4.8(a)).

Interpolation analysis of the remaining IR peaks is quite involved in this case. Therefore we turned to the analysis of the inner products of the phonon modes in the isolated monolayer and the monolayer placed on Au(111). These inner products are shown in Table 4.4. From this table we again confirm that the ω_1^{Au} mode originates from the ω_1^{M} mode. In addition, we found that the ω_3^{Au} mode has one-to-one correspondence with the ω_3^{M} mode.

For the remaining IR active modes (ω_2^{Au}, ω_4^{Au}, ω_5^{Au}, and ω_6^{Au}) we found strong influence by the monolayer-substrate interaction. Analyzing Table 4.4 reveals that the ω_2^{Au} mode of adamantane on the Au(111) substrate is a mixture of the ω_2^{M}, ω_5^{M}, and ω_6^{M} modes of the isolated monolayer phase. Similarly, the ω_4^{Au} mode is composed of the ω_2^{M}, ω_4^{M}, and ω_5^{M} modes, while the ω_5^{Au} mode comes mostly from the ω_6^{M} mode with some admixture of the ω_5^{M} mode. The IR intensity of modes ω_2^{Au}, ω_4^{Au} and ω_5^{Au} are relatively small since these modes include only a small amount of CH bond stretch perpendicular to the surface (see phonon eigendisplacements in Figure 4.8).

On the other hand, Table 4.4 shows a rather remarkable change in the frequency and IR intensity of the ω_6^{Au} mode. This mode is a mixture of the ω_4^{M} ($2934\,\mathrm{cm}^{-1}$) and ω_2^{M} ($2879\,\mathrm{cm}^{-1}$) modes of the isolated monolayer phase and its frequency is redshifted to $2664\,\mathrm{cm}^{-1}$. Furthermore, its IR intensity is increased from 0.05 to $0.16\,e^2$ (effective charge in Table 4.4 changes from 0.22 to $0.40\,e$) compared to the ω_4^{M} mode. The ω_6^{Au} mode consists of the in-phase perpendicular vibration of the three bottom hydrogen atoms near the Au(111) surface [see Figure 4.8(f)], therefore it is not unexpected that this mode will be significantly affected by the Au(111) surface. Comparison of the charge density of the isolated adamantane monolayer to the charge density of the monolayer on the Au(111) surface reveals that the molecule-surface interaction reduces the electron charge density on the adamantane CH bonds. We

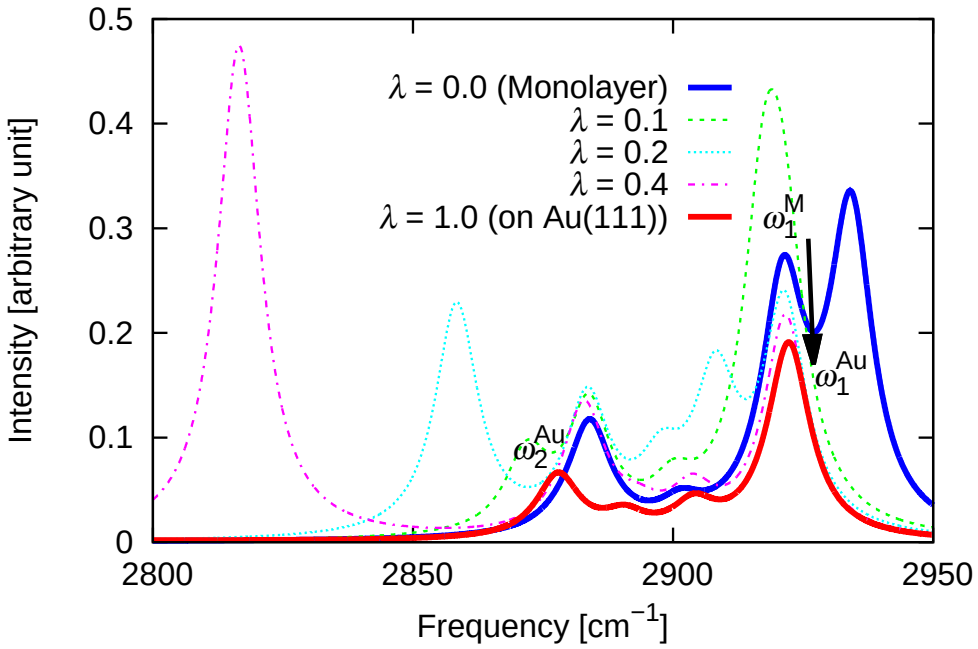

Figure 4.7: Interpolated IR spectra going from an isolated molecular monolayer to a monolayer on Au(111). The blue solid line shows the IR spectrum of the isolated molecular monolayer, while the red solid line shows the IR spectrum of the monolayer on the Au(111) substrate. The dashed ($\lambda = 0.1$), dotted ($\lambda = 0.2$), and chain ($\lambda = 0.4$) lines show an interpolated spectra between the two cases. The arrow shows the transition from ω_1^{M} to ω_1^{Au}. The peak position of the relatively weak ω_2^{Au} mode is also indicated. The severely redshifted peak ω_6^{Au} is not shown in this figure (see left panel of Figure 4.4).

speculate that this reduction of charge density within the CH bonds is responsible for the decrease in the ω_6^{Au} mode frequency as well as increase of its effective charge.

4.4.3 Comparison of Theory and Experiment

Figure 4.9 shows a comparison of the experimental (green line) and theoretical (dashed blue line) IR spectra for an adamantane monolayer on the Au(111) surface. We found good qualitative agreement between the two spectra, both in the peak position and in their relative intensities (the experimental vertical scale is chosen so that the peak height at 2846 cm^{-1} matches the theoretical peak height at 2851 cm^{-1}). Agreement is even better after applying a correction to the calculated phonon frequencies (red line in Figure 4.9) as it is described below in Section 4.4.3.

We have assigned the relatively large experimentally obtained IR peak at 2912 cm^{-1} to the theoretically obtained ω_1^{Au} mode (2922 cm^{-1}, corrected frequency 2914 cm^{-1}, phonon effective

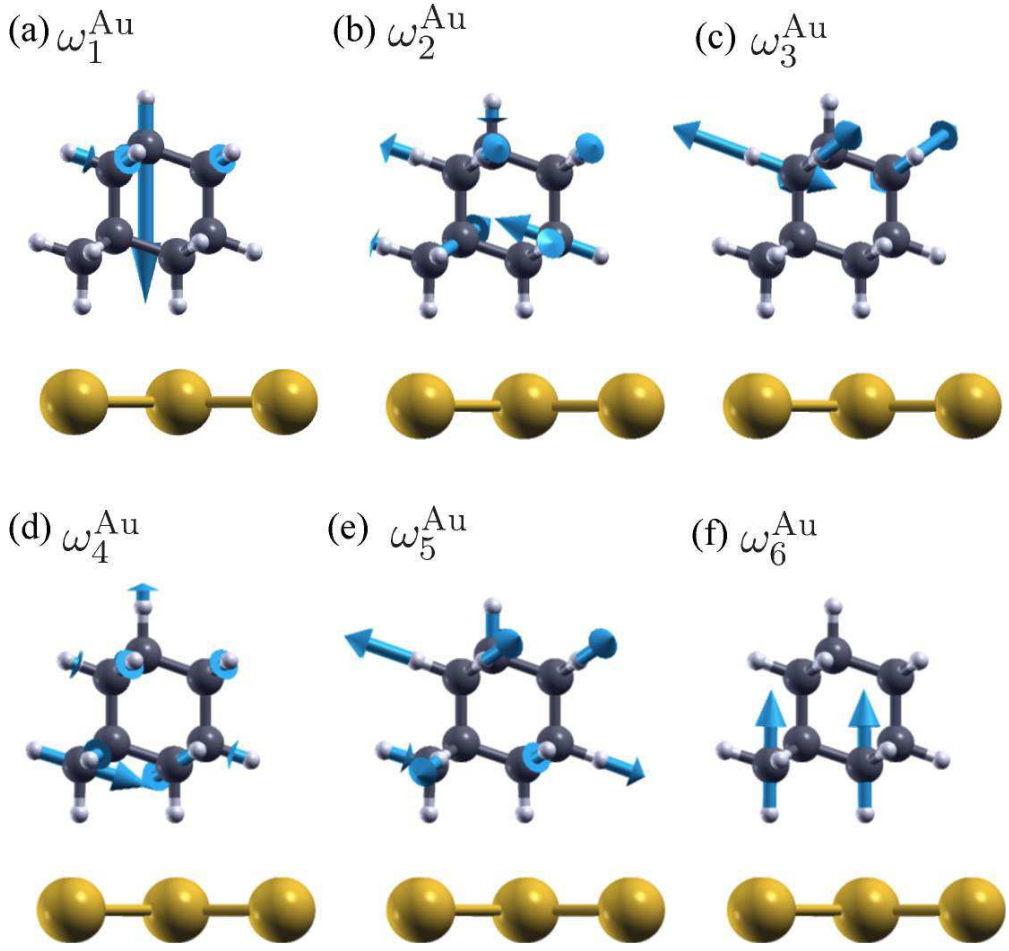

Figure 4.8: Eigendisplacement vectors of (a) ω_1^{Au}, (b) ω_2^{Au}, (c) ω_3^{Au}, (d) ω_4^{Au}, (e) ω_5^{Au}, and (f) ω_6^{Au} modes of an adamantane monolayer on a Au(111) surface. Yellow spheres illustrate gold atoms in the topmost layer of the Au(111) surface.

charge $0.17\,e$). Furthermore, we have assigned the relatively weaker mode at $2846\,\mathrm{cm}^{-1}$ to the theoretically obtained ω_2^{Au} mode ($2878\,\mathrm{cm}^{-1}$, corrected frequency $2851\,\mathrm{cm}^{-1}$, phonon effective charge $0.10\,e$). Remaining features in the experimental data (green line in Figure 4.9) were not reproducible and therefore cannot be reliably assigned to the additional IR phonon modes. This is consistent with our theory, as the remaining IR active modes ω_3^{Au}, ω_4^{Au}, and ω_5^{Au} have a much smaller phonon effective charge (from 0.01 to $0.07\,e$).

Finally, our calculation predicts the existence of a significantly redshifted IR active mode ω_6^{Au} at $2664\,\mathrm{cm}^{-1}$ (corrected value is $2644\,\mathrm{cm}^{-1}$) with a large phonon effective charge ($0\,40e$). Although the frequency of this mode was outside of our experimentally attainable frequency range (from 2840 to $2990\,\mathrm{cm}^{-1}$), we expect that it will be accessible to future experimental probing.

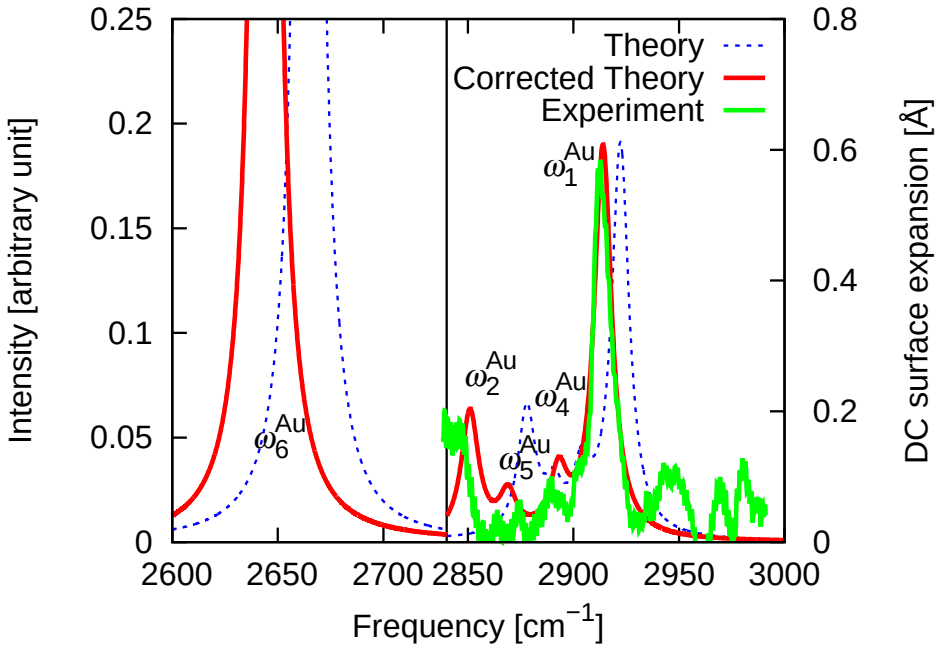

Figure 4.9: Uncorrected (blue dashed line) and corrected (red solid line) theoretical IR spectra and experimentally observed IR spectrum (green solid line). The frequency region between 2730 cm^{-1} and 2840 cm^{-1} is not shown. The vertical scale is chosen so that the theoretical and experimental peaks around 2850 cm^{-1} have almost the same height. Left and right vertical axes correspond to theoretical and experimental IR intensity. Corrected theoretical values of ω_1^{Au}, ω_2^{Au}, ω_4^{Au}, ω_5^{Au}, and ω_6^{Au} modes are 2914, 2851, 2893, 2869, and 2644 cm^{-1}, respectively.

Dynamical Matrix Correction

Here we present the method we used to correct the DFT-LDA IR spectrum of the adamantane monolayer on the Au(111) substrate (red line in Figure 4.9). First we obtained the correction D^{corr} to the calculated dynamical matrix of the adamantane gas phase so that it exactly reproduces the experimentally measured frequencies of adamantane gas and solution phase,

$$D^{corr} = \sum_i (\Delta_i^2 - 2\omega_i\Delta_i)\,|u_i\rangle\,\langle u_i|\,. \tag{4.5}$$

Here ω_i and $|u_i\rangle$ are the phonon frequencies and eigenvectors of the original dynamical matrix, while Δ_i is the difference between the computed and the measured adamantane gas and solution phase frequency. In the second step, we added this same correction matrix D^{corr} to the dynamical matrix of the adamantane monolayer on the Au(111) surface. Finally, we used the eigenvalues and eigenvectors of the corrected dynamical matrix to compute the

corrected IR spectrum.

Our correction procedures improved the agreement of the calculated IR spectrum of adamantane on the Au(111) surface with the experimental spectrum (see Figure 4.9). The theoretical peak position of the ω_1^{Au} mode has been redshifted by $8\,\mathrm{cm}^{-1}$ (from 2922 to $2914\,\mathrm{cm}^{-1}$) and it now sits closer to the experimental peak position ($2913 \pm 1\,\mathrm{cm}^{-1}$). Similarly, the ω_2^{Au} mode has been redshifted by $27\,\mathrm{cm}^{-1}$ (from 2878 to $2851\,\mathrm{cm}^{-1}$), again closer to the experimental value ($2846 \pm 2\,\mathrm{cm}^{-1}$). The dominant components of the correction matrix (Equation 4.5) correspond to the CH and CH_2 bonds (the corresponding amplitudes are about $1.2 \times 10^4\,\mathrm{cm}^{-2}$).

4.5 Conclusion

Our work combining IRSTM measurements and *ab initio* calculation of the IR spectrum of an adamantane monolayer on Au(111) demonstrates the complex nature of adamantane-adamantane and adamantane-gold interactions. In Section 4.4.2 we have described in detail the effect of each of these interactions on the mixing (hybridization) of adamantane vibrational modes, the changes in their frequencies, and the IR intensities. Figure 4.10 summarizes the main results of this chapter. The black dashed line in Figure 4.10 shows the calculated isolated adamantane gas-phase IR spectrum, while the red line shows the severely modified spectrum of the adamantane monolayer on the Au(111) surface. The green line shows the experimental spectrum of an adamantane submonolayer on Au(111).

The IR spectrum of the isolated adamantane molecule (black dashed line in Figure 4.10) consists of three IR active CH stretch modes (ω_5, ω_6, ω_7). The adamantane-adamantane interaction (packing effect) reduces the IR intensity of one of these modes (ω_6) by a factor of 3.5. On the other hand, the adamantane-gold interaction severely redshifts the gas-phase ω_5 mode (by $276\,\mathrm{cm}^{-1}$), and increases its IR intensity by a factor of 2.6. In addition, both ω_5 and ω_6 are hybridized with IR inactive gas-phase modes (ω_2 and ω_1 respectively). See Sections 4.4.2, 4.4.2 and Tables 4.3, 4.4 for more details.

In conclusion, we expect that these experimental and theoretical techniques can be used to study intermolecular and molecule-substrate effects of other molecular systems, including the use of other metallic substrates. In particular, we expect that the IR intensity reduction of the gas-phase ω_6 mode (or equivalent, for other molecules) can be used as a direct measure of intermolecular interactions. Similarly, the increase in the IR intensity and the redshift of the ω_5 mode can be used as a direct measure of molecule-substrate interactions.

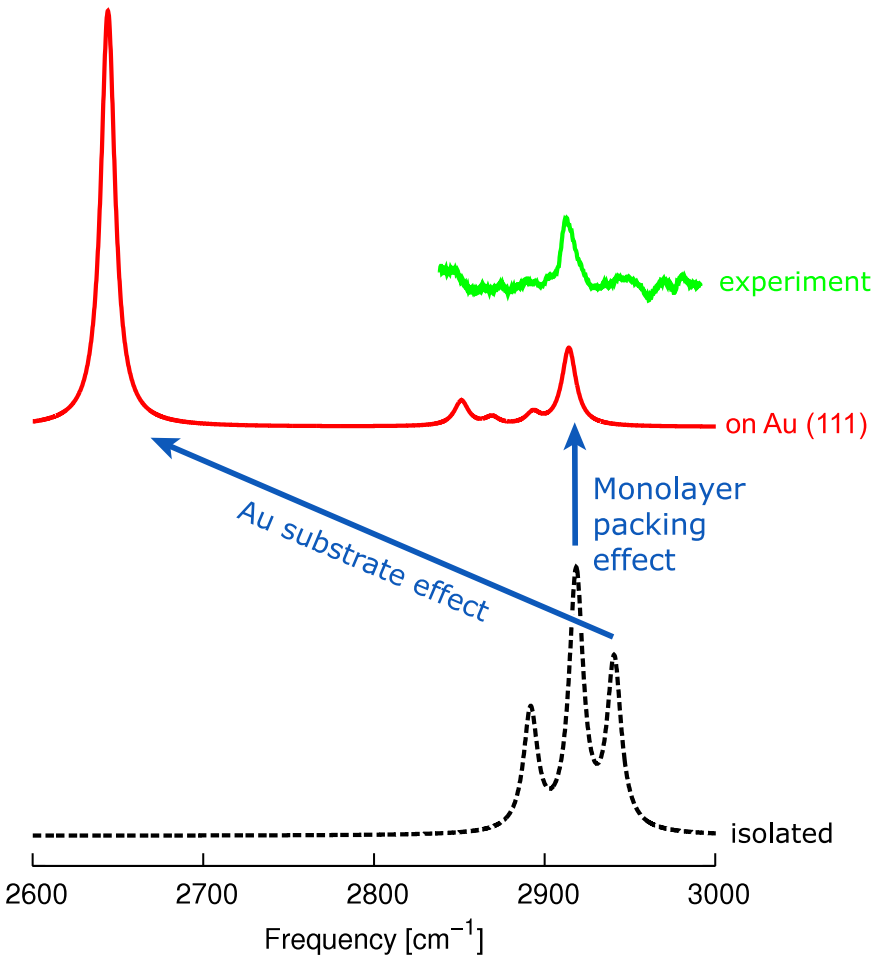

Figure 4.10: Summary of the main results. There are three IR active CH stretch modes in the isolated (gas-phase) adamantane molecule (black dashed line). The interaction between the neighboring adamantane molecules in the monolayer (packing effect) reduces the IR intensity of the central IR active mode by a factor of 3.5. The interaction between the monolayer and the Au(111) surface (Au substrate effect) reduces the highest frequency gas-phase mode by 276 cm^{-1} and it increases its IR intensity by a factor of 2.6. The remaining third IR active gas-phase mode is affected both by the Au(111) substrate and by the packing effect. See Section 4.4.2 for more detailed analysis. The calculated IR spectrum of an adamantane monolayer on Au(111) is shown with a red line, while the experimental spectrum is shown with a green line.

Bibliography

[1] R. P. Feynman, "There's Plenty of Room at the Bottom", Engineering and Science **23**, 22 (1960).

[2] E. K. Drexler, *Engines of Creation: The Coming Era of Nanotechnology*, 1st ed. (Garden City, N.Y.: Anchor Press/Doubleday, 1986).

[3] G. Binnig, H. Rohrer, Ch. Gerber, and E. Weibel, "Surface Studies by Scanning Tunneling Microscopy", Phys. Rev. Lett. **49**, 57 (1982).

[4] G. Binnig and H. Rohrer, "Scanning tunneling microscopy—from birth to adolescence", Rev. Mod. Phys. **59**, 615 (1987).

[5] R. J. Hamers, R. M. Tromp, and J. E. Demuth, "Surface Electronic Structure of Si(111)-(7×7) Resolved in Real Space", Phys. Rev. Lett. **56**, 1972 (1986).

[6] R. J. Hamers, "Atomic-Resolution Surface Spectroscopy with the Scanning Tunneling Microscope", Annu. Rev. Phys. Chem. **40**, 531 (1989).

[7] J. A. Stroscio and D. M. Eigler, "Atomic and Molecular Manipulation with the Scanning Tunneling Microscope", Science **254**, 1319 (1991).

[8] M. F. Crommie, C. P. Lutz, and D. M. Eigler, "Confinement of Electrons to Quantum Corrals on a Metal Surface", Science **262**, 218 (1993).

[9] F. Moresco, "Manipulation of large molecules by low-temperature STM: model systems for molecular electronics", Phys. Rep. **399**, 175 (2004).

[10] S.-W. Hla, "Scanning tunneling microscopy single atom/molecule manipulation and its application to nanoscience and technology", J. Vac. Sci. Technol. B **23**, 1351 (2005).

[11] G. Binnig, C. F. Quate, and Ch. Gerber, "Atomic Force Microscope", Phys. Rev. Lett. **56**, 930 (1986).

[12] D. W. Pohl, W. Denk, and M. Lanz, "Optical stethoscopy: Image recording with resolution $\lambda/20$", Appl. Phys. Lett. **44**, 651 (1984).

[13] E. Betzig, A. Lewis, A. Harootunian, M. Isaacson, and E. Kratschmer, "Near Field Scanning Optical Microscopy (NSOM)", Biophys. J. **49**, 269 (1986).

[14] R. A. Friesner, "*Ab initio* quantum chemistry: Methodology and applications", Proc. Nat. Acad. Sci. USA **102**, 6648 (2005).

[15] V. Balzani, A. Credi, and M. Venturi, *Molecular Devices and Machines: Concepts and Perspectives for the Nanoworld*, 2nd ed. (Wiley-VCH Verlag GmbH & Co. KGaA, Weinheim, Germany, 2008).

[16] W. R. Browne and B. L. Feringa, "Light Switching of Molecules on Surfaces", Annu. Rev. Phys. Chem. **60**, 407 (2009).

[17] H. Rau, in *Photochromism: Molecules and Systems*, edited by H. Dürr and H. Bouas-Laurent, Studies in Organic Chemistry (Elsevier, Amsterdam, 1990), pp. 165–192.

[18] C.-Q. Wu, J.-X. Li, and D.-H. Lee, "Switching and Nonswitching Phases of Photomechanical Molecules in Dissipative Environments", Phys. Rev. Lett. **99**, 038302 (2007).

[19] M. L. Tiago, S. Ismail-Beigi, and S. G. Louie, "Photoisomerization of azobenzene from first-principles constrained density-functional calculations", J. Chem. Phys. **122**, 094311 (2005).

[20] T. J. Martinez, "Physical chemistry: Seaming is believing", Nature **467**, 412 (2010).

[21] D. Polli, P. Altoe, O. Weingart, K. M. Spillane, C. Manzoni, D. Brida, G. Tomasello, G. Orlandi, P. Kukura, R. A. Mathies, M. Garavelli, and G. Cerullo, "Conical intersection dynamics of the primary photoisomerization event in vision", Nature **467**, 440 (2010).

[22] T. R. Ohno, Y. Chen, S. E. Harvey, G. H. Kroll, J. H. Weaver, R. E. Haufler, and R. E. Smalley, "C_{60} bonding and energy-level alignment on metal and semiconductor surfaces", Phys. Rev. B **44**, 13747 (1991).

[23] S. Hagen, P. Kate, F. Leyssner, D. Nandi, M. Wolf, and P. Tegeder, "Excitation mechanism in the photoisomerization of a surface-bound azobenzene derivative: Role of the metallic substrate", J. Chem. Phys. **129**, 164102 (2008).

[24] M. Wolf and P. Tegeder, "Reversible molecular switching at a metal surface: A case study of tetra-*tert*-butyl-azobenzene on Au(111)", Surf. Sci. **603**, 1506 (2009).

[25] M. J. Comstock, N. Levy, A. Kirakosian, J. Cho, F. Lauterwasser, J. H. Harvey, D. A. Strubbe, J. M. J. Fréchet, D. Trauner, S. G. Louie, and M. F. Crommie, "Reversible Photomechanical Switching of Individual Engineered Molecules at a Metallic Surface", Phys. Rev. Lett. **99**, 038301 (2007).

[26] J. Cho, L. Berbil-Bautista, N. Levy, D. Poulsen, J. M. J. Fréchet, and M. F. Crommie, "Functionalization, self-assembly, and photoswitching quenching for azobenzene derivatives adsorbed on Au(111)", J. Chem. Phys. **133**, 234707 (2010).

[27] E. B. Wilson, Jr., J. C. Decius, and P. C. Cross, *Molecular Vibrations: The Theory of Infrared and Raman Vibrational Spectra* (New York: McGraw-Hill Book Company, 1955).

[28] C. L. Feng, Y. Zhang, J. Jin, Y. Song, L. Xie, G. Qu, L. Jiang, and D. Zhu, "Completely interfacial photoisomerization of 4-hydroxy-3′-trifluoromethyl-azobenzene studied by STM on HOPG", Surf. Sci. **513**, 111 (2002).

[29] S. Yasuda, T. Nakamura, M. Matsumoto, and H. Shigekawa, "Phase Switching of a Single Isomeric Molecule and Associated Characteristic Rectification", J. Am. Chem. Soc. **125**, 16430 (2003).

[30] A. S. Kumar, T. Ye, T. Takami, B.-C. Yu, A. K. Flatt, J. M. Tour, and P. S. Weiss, "Reversible Photo-Switching of Single Azobenzene Molecules in Controlled Nanoscale Environments", Nano Lett. **8**, 1644 (2008).

[31] M. Bazarnik, J. Henzl, R. Czajka, and K. Morgenstern, "Light driven reactions of single physisorbed azobenzenes", Chem. Commun. **47**, 7764 (2011).

[32] K. Morgenstern, "Switching individual molecules by light and electrons: From isomerisation to chirality flip", Prog. Surf. Sci. **86**, 115 (2011).

[33] S. Grothe, S. Chi, P. Dosanjh, R. Liang, W. N. Hardy, S. A. Burke, D. A. Bonn, and Y. Pennec, "Bound states of defects in superconducting LiFeAs studied by scanning tunneling spectroscopy", Phys. Rev. B **86**, 174503 (2012).

[34] R. M. Feenstra, G. Meyer, F. Moresco, and K. H. Rieder, "Low-temperature scanning tunneling spectroscopy of n-type GaAs(110) surfaces", Phys. Rev. B **66**, 165204 (2002).

[35] M. F. Crommie, C. P. Lutz, and D. M. Eigler, "Spectroscopy of a single adsorbed atom", Phys. Rev. B **48**, 2851 (1993).

[36] B. C. Stipe, M. A. Rezaei, and W. Ho, "Single-Molecule Vibrational Spectroscopy and Microscopy", Science **280**, 1732 (1998).

[37] N. Lorente, M. Persson, L. J. Lauhon, and W. Ho, "Symmetry Selection Rules for Vibrationally Inelastic Tunneling", Phys. Rev. Lett. **86**, 2593 (2001).

[38] Y. Wang, E. Kioupakis, X. Lu, D. Wegner, R. Yamachika, J. E. Dahl, R. M. K. Carlson, S. G. Louie, and M. F. Crommie, "Spatially resolved electronic and vibronic properties of single diamondoid molecules", Nat. Mater. **7**, 38 (2008).

[39] T. Kudernac, N. Ruangsupapichat, M. Parschau, B. Macia, N. Katsonis, S. R. Harutyunyan, K.-H. Ernst, and B. L. Feringa, "Electrically driven directional motion of a four-wheeled molecule on a metal surface", Nature **479**, 208 (2011).

[40] S. H. Pan, E. W. Hudson, and J. C. Davis, "^{3}He refrigerator based very low temperature scanning tunneling microscope", Rev. Sci. Instrum. **70**, 1459 (1999).

[41] J. Bardeen, "Tunnelling from a Many-Particle Point of View", Phys. Rev. Lett. **6**, 57 (1961).

[42] J. Tersoff and D. R. Hamann, "Theory and Application for the Scanning Tunneling Microscope", Phys. Rev. Lett. **50**, 1998 (1983).

[43] J. Tersoff and D. R. Hamann, "Theory of the scanning tunneling microscope", Phys. Rev. B **31**, 805 (1985).

[44] C. J. Chen, *Introduction to Scanning Tunneling Microscopy*, 2nd ed. (New York: Oxford University Press, 2008).

[45] R. Yamachika, "Probing Atomic-Scale Properties of Organic and Organometallic Molecules by Scanning Tunneling Spectroscopy", PhD thesis (University of California, Berkeley, 2009).

[46] M. J. Comstock, "Photomechanical Switching of Individual Molecules on a Surface", PhD thesis (University of California, Berkeley, 2008).

[47] N. B. Levy, "Investigations into nanometer scale surface opto-electro-mechanical coupling", PhD thesis (University of California, Berkeley, 2010).

[48] J. Cho, "Exploring Self-Assembly and Photomechanical Switching Properties of Molecules at Surfaces", PhD thesis (University of California, Berkeley, 2010).

[49] D. Nečas and P. Klapetek, "Gwyddion: an open-source software for SPM data analysis", Cent. Eur. J. Phys. **10**, 181 (2012).

[50] K. Chatterjee, M. C. Boyer, W. D. Wise, and E. W. Hudson, "An auxiliary capacitor based ultrafast drive circuit for shear piezoelectric motors", Rev. Sci. Instrum. **80**, 095110 (2009).

[51] M. K. Grobis, "Scanning Tunneling Spectroscopy of Fullerene Nanostructures", PhD thesis (University of California, Berkeley, 2005).

[52] I. V. Pechenezhskiy, J. Cho, G. D. Nguyen, L. Berbil-Bautista, B. L. Giles, D. A. Poulsen, J. M. J. Fréchet, and M. F. Crommie, "Self-Assembly and Photomechanical Switching of an Azobenzene Derivative on GaAs(110): Scanning Tunneling Microscopy Study", J. Phys. Chem. C **116**, 1052 (2012).

[53] C. Zhang, M.-H. Du, H.-P. Cheng, X.-G. Zhang, A. E. Roitberg, and J. L. Krause, "Coherent Electron Transport through an Azobenzene Molecule: A Light-Driven Molecular Switch", Phys. Rev. Lett. **92**, 158301 (2004).

[54] M. R. Banghart, M. Volgraf, and D. Trauner, "Engineering Light-Gated Ion Channels", Biochemistry **45**, 15129 (2006).

[55] J. J. Chambers, M. R. Banghart, D. Trauner, and R. H. Kramer, "Light-Induced Depolarization of Neurons Using a Modified Shaker K^+ Channel and a Molecular Photoswitch", J. Neurophysiol. **96**, 2792 (2006).

[56] L. Óvári, M. Wolf, and P. Tegeder, "Reversible Changes in the Vibrational Structure of Tetra-*tert*-butylazobenzene on a Au(111) Surface Induced by Light and Thermal Activation", J. Phys. Chem. C **111**, 15370 (2007).

[57] S. Hagen, F. Leyssner, D. Nandi, M. Wolf, and P. Tegeder, "Reversible switching of tetra-*tert*-butyl-azobenzene on a Au(111) surface induced by light and thermal activation", Chem. Phys. Lett. **444**, 85 (2007).

[58] R. M. Feenstra, J. A. Stroscio, J. Tersoff, and A. P. Fein, "Atom-selective imaging of the GaAs(110) surface", Phys. Rev. Lett. **58**, 1192 (1987).

[59] M. B. Johnson, O. Albrektsen, R. M. Feenstra, and H. W. M. Salemink, "Direct imaging of dopants in GaAs with cross-sectional scanning tunneling microscopy", Appl. Phys. Lett. **63**, 2923 (1993); "Erratum: Direct imaging of dopants in GaAs with cross-sectional scanning tunneling microscopy [Appl. Phys. Lett. **63**, 2923 (1993)]", ibid. **64**, 1454 (1994).

[60] J. F. Zheng, X. Liu, N. Newman, E. R. Weber, D. F. Ogletree, and M. Salmeron, "Scanning Tunneling Microscopy Studies of Si Donors (Si_{Ga}) in GaAs", Phys. Rev. Lett. **72**, 1490 (1994).

[61] K.-J. Chao, A. R. Smith, and C.-K. Shih, "Direct determination of exact charge states of surface point defects using scanning tunneling microscopy: As vacancies on GaAs(110)", Phys. Rev. B **53**, 6935 (1996).

[62] N. Pozhidaeva, M.-E. Cormier, A. Chaudhari, and G. A. Woolley, "Reversible Photocontrol of Peptide Helix Content: Adjusting Thermal Stability of the Cis State", Bioconjugate Chem. **15**, 1297 (2004).

[63] M. Alemani, M. V. Peters, S. Hecht, K.-H. Rieder, F. Moresco, and L. Grill, "Electric Field-Induced Isomerization of Azobenzene by STM", J. Am. Chem. Soc. **128**, 14446 (2006).

[64] M. J. Comstock, N. Levy, J. Cho, L. Berbil-Bautista, M. F. Crommie, D. A. Poulsen, and J. M. J. Fréchet, "Measuring reversible photomechanical switching rates for a molecule at a surface ", Appl. Phys. Lett. **92**, 123107 (2008).

[65] M. Alemani, S. Selvanathan, F. Ample, M. V. Peters, K.-H. Rieder, F. Moresco, C. Joachim, S. Hecht, and L. Grill, "Adsorption and Switching Properties of Azobenzene Derivatives on Different Noble Metal Surfaces: Au(111), Cu(111), and Au(100)", J. Phys. Chem. C **112**, 10509 (2008).

[66] N. Levy, M. J. Comstock, J. Cho, L. Berbil-Bautista, A. Kirakosian, F. Lauterwasser, D. A. Poulsen, J. M. J. Fréchet, and M. F. Crommie, "Self-Patterned Molecular Photoswitching in Nanoscale Surface Assemblies", Nano Lett. **9**, 935 (2009).

[67] M. J. Comstock, D. A. Strubbe, L. Berbil-Bautista, N. Levy, J. Cho, D. Poulsen, J. M. J. Fréchet, S. G. Louie, and M. F. Crommie, "Determination of Photoswitching Dynamics through Chiral Mapping of Single Molecules Using a Scanning Tunneling Microscope", Phys. Rev. Lett. **104**, 178301 (2010).

[68] I. V. Pechenezhskiy, X. Hong, G. D. Nguyen, J. E. P. Dahl, R. M. K. Carlson, F. Wang, and M. F. Crommie, "Infrared Spectroscopy of Molecular Submonolayers on Surfaces by Infrared Scanning Tunneling Microscopy: Tetramantane on Au(111)", Phys. Rev. Lett. **111**, 126101 (2013).

[69] R. Berndt, R. Gaisch, J. K. Gimzewski, B. Reihl, R. R. Schlittler, W. D. Schneider, and M. Tschudy, "Photon Emission at Molecular Resolution Induced by a Scanning Tunneling Microscope", Science **262**, 1425 (1993).

[70] X. H. Qiu, G. V. Nazin, and W. Ho, "Vibrationally Resolved Fluorescence Excited with Submolecular Precision", Science **299**, 542 (2003).

[71] Z.-C. Dong, X.-L. Guo, A. S. Trifonov, P. S. Dorozhkin, K. Miki, K. Kimura, S. Yokoyama, and S. Mashiko, "Vibrationally Resolved Fluorescence from Organic Molecules near Metal Surfaces in a Scanning Tunneling Microscope", Phys. Rev. Lett. **92**, 086801 (2004).

[72] Z. C. Dong, X. L. Zhang, H. Y. Gao, Y. Luo, C. Zhang, L. G. Chen, R. Zhang, X. Tao, Y. Zhang, J. L. Yang, and J. G. Hou, "Generation of molecular hot electroluminescence by resonant nanocavity plasmons", Nat. Photonics **4**, 50 (2010).

[73] C. Chen, P. Chu, C. A. Bobisch, D. L. Mills, and W. Ho, "Viewing the Interior of a Single Molecule: Vibronically Resolved Photon Imaging at Submolecular Resolution", Phys. Rev. Lett. **105**, 217402 (2010).

[74] A. Hartschuh, "Tip-Enhanced Near-Field Optical Microscopy", Angew. Chem., Int. Ed. Engl. **47**, 8178 (2008).

[75] J. Steidtner and B. Pettinger, "Tip-Enhanced Raman Spectroscopy and Microscopy on Single Dye Molecules with 15 nm Resolution", Phys. Rev. Lett. **100**, 236101 (2008).

[76] B. Pettinger, P. Schambach, C. J. Villagómez, and N. Scott, "Tip-Enhanced Raman Spectroscopy: Near-Fields Acting on a Few Molecules", Annu. Rev. Phys. Chem. **63**, 379 (2012).

[77] B. Pettinger, G. Picardi, R. Schuster, and G. Ertl, "Surface-enhanced and STM-tip-enhanced Raman Spectroscopy at Metal Surfaces", Single Mol. **3**, 285 (2002).

[78] A. Dazzi, R. Prazeres, F. Glotin, and J. M. Ortega, "Local infrared microspectroscopy with subwavelength spatial resolution with an atomic force microscope tip used as a photothermal sensor", Opt. Lett. **30**, 2388 (2005).

[79] A. Dazzi, C. B. Prater, Q. Hu, D. B. Chase, J. F. Rabolt, and C. Marcott, "AFM-IR: Combining Atomic Force Microscopy and Infrared Spectroscopy for Nanoscale Chemical Characterization", Appl. Spectrosc. **66**, 1365 (2012).

[80] J. R. Felts, K. Kjoller, M. Lo, C. B. Prater, and W. P. King, "Nanometer-Scale Infrared Spectroscopy of Heterogeneous Polymer Nanostructures Fabricated by Tip-Based Nanofabrication", ACS Nano **6**, 8015 (2012).

[81] B. Lahiri, G. Holland, and A. Centrone, "Chemical Imaging Beyond the Diffraction Limit: Experimental Validation of the PTIR Technique", Small **9**, 439 (2013).

[82] V. Krishna and J. C. Tully, "Vibrational lifetimes of molecular adsorbates on metal surfaces", J. Chem. Phys. **125**, 054706 (2006).

[83] X. Hong, X. Shen, M. Gong, and F. Wang, "Broadly tunable mode-hop-free mid-infrared light source with MgO:PPLN continuous-wave optical parametric oscillator", Opt. Lett. **37**, 4982 (2012).

[84] M. Völcker, W. Krieger, T. Suzuki, and H. Walther, "Laser-assisted scanning tunneling microscopy", J. Vac. Sci. Technol. B **9**, 541 (1991).

[85] J. E. Dahl, S. G. Liu, and R. M. K. Carlson, "Isolation and Structure of Higher Diamondoids, Nanometer-Sized Diamond Molecules", Science **299**, 96 (2003).

[86] T. Holstein, "Optical and Infrared Reflectivity of Metals at Low Temperatures", Phys. Rev. **88**, 1427 (1952).

[87] M. M. Fulk and M. M. Reynolds, "Emissivities of Metallic Surfaces at 76 °K", J. Appl. Phys. **28**, 1464 (1957).

[88] L. J. Lauhon and W. Ho, "Effects of temperature and other experimental variables on single molecule vibrational spectroscopy with the scanning tunneling microscope", Rev. Sci. Instrum. **72**, 216 (2001).

[89] A. Troisi and M. A. Ratner, "Propensity rules for inelastic electron tunneling spectroscopy of single-molecule transport junctions", J. Chem. Phys. **125**, 214709 (2006).

[90] J. B. Maddox, U. Harbola, N. Liu, C. Silien, W. Ho, G. C. Bazan, and S. Mukamel, "Simulation of Single Molecule Inelastic Electron Tunneling Signals in Paraphenylene-Vinylene Oligomers and Distyrylbenzene[2.2]paracyclophanes", J. Phys. Chem. A **110**, 6329 (2006).

[91] J. Oomens, N. Polfer, O. Pirali, Y. Ueno, R. Maboudian, P. W. May, J. Filik, J. E. Dahl, S. Liu, and R. M. K. Carlson, "Infrared spectroscopic investigation of higher diamondoids", J. Mol. Spectrosc. **238**, 158 (2006).

[92] F. M. Hoffmann, "Infrared reflection-absorption spectroscopy of adsorbed molecules", Surf. Sci. Rep. **3**, 107 (1983).

[93] P. R. Schreiner, L. V. Chernish, P. A. Gunchenko, E. Yu. Tikhonchuk, H. Hausmann, M. Serafin, S. Schlecht, J. E. P. Dahl, R. M. K. Carlson, and A. A. Fokin, "Overcoming lability of extremely long alkane carbon-carbon bonds through dispersion forces", Nature (London) **477**, 308 (2011).

[94] A. A. Fokin, L. V. Chernish, P. A. Gunchenko, E. Yu. Tikhonchuk, H. Hausmann, M. Serafin, J. E. P. Dahl, R. M. K. Carlson, and P. R. Schreiner, "Stable Alkanes Containing Very Long Carbon-Carbon bonds", J. Am. Chem. Soc. **134**, 13641 (2012).

[95] Y. Sakai, G. D. Nguyen, R. B. Capaz, S. Coh, I. V. Pechenezhskiy, X. Hong, F. Wang, M. F. Crommie, S. Saito, S. G. Louie, and M. L. Cohen, "Intermolecular interactions and substrate effects for an adamantane monolayer on a Au(111) surface", Phys. Rev. B **88**, 235407 (2013).

[96] N. D. Drummond, A. J. Williamson, R. J. Needs, and G. Galli, "Electron Emission from Diamondoids: A Diffusion Quantum Monte Carlo Study", Phys. Rev. Lett. **95**, 096801 (2005).

[97] W. L. Yang, J. D. Fabbri, T. M. Willey, J. R. I. Lee, J. E. Dahl, R. M. K. Carlson, P. R. Schreiner, A. A. Fokin, B. A. Tkachenko, N. A. Fokina, W. Meevasana, N. Mannella, K. Tanaka, X. J. Zhou, T. van Buuren, M. A. Kelly, Z. Hussain, N. A. Melosh, and Z.-X. Shen, "Monochromatic Electron Photoemission from Diamondoid Monolayers", Science **316**, 1460 (2007).

[98] D. F. Blake, F. Freund, K. F. M. Krishnan, C. J. Echer, R. Shipp, T. E. Bunch, A. G. Tielens, R. J. Lipari, C. J. D. Hetherington, and S. Chang, "The nature and origin of interstellar diamond", Nature (London) **332**, 611 (1988).

[99] O. Pirali, M. Vervloet, J. E. Dahl, R. M. K. Carlson, A. G. G. M. Tielens, and J. Oomens, "Infrared Spectroscopy of Diamondoid Molecules: New Insights into the Presence of Nanodiamonds in the Interstellar Medium", Astrophys. J. **661**, 919 (2007).

[100] R. T. Bailey, "Spectroscopic and thermodynamic studies of molecular crystals—I: The internal vibrations of adamantane in the plastic phase", Spectrochim. Acta, Part A **27**, 1447 (1971).

[101] T. J. Broxton, L. W. Deady, M. Kendall, and R. D. Topsom, "Infrared Spectra of Adamantanes", Appl. Spectrosc. **25**, 600 (1971).

[102] P.-J. Wu, L. Hsu, and D. A. Dows, "Spectroscopic Study of the Phase Transition in Crystalline Adamantane", J. Chem. Phys. **54**, 2714 (1971).

[103] R. M. Corn, V. L. Shannon, R. G. Snyder, and H. L. Strauss, "Orientational dynamics and disorder of solid adamantane as studied by infrared spectroscopy", J. Chem. Phys. **81**, 5231 (1984).

[104] L. Bistričić, G. Baranović, and K. Mlinarić-Majerski, "A vibrational assignment of adamantane and some of its isotopomers. Empirical versus scaled semiempirical force field", Spectrochim. Acta, Part A **51**, 1643 (1995).

[105] G. Szász and A. Kovács, "Investigation of the density-functional theory-derived scaled quantum mechanical method for cage-like systems: the vibrational analysis of adamantane", Mol. Phys. **96**, 161 (1999).

[106] J. O. Jensen, "Vibrational frequencies and structural determination of adamantane", Spectrochim. Acta, Part A **60**, 1895 (2004).

[107] O. Pirali, V. Boudon, J. Oomens, and M. Vervloet, "Rotationally resolved infrared spectroscopy of adamantane", J. Chem. Phys. **136**, 024310 (2012).

[108] T. Kitagawa, Y. Idomoto, H. Matsubara, D. Hobara, T. Kakiuchi, T. Okazaki, and K. Komatsu, "Rigid Molecular Tripod with an Adamantane Framework and Thiol Legs. Synthesis and Observation of an Ordered Monolayer on Au(111)", J. Org. Chem. **71**, 1362 (2006).

[109] D. A. Smith and R. W. Owens, "Laser-assisted scanning tunnelling microscope detection of a molecular adsorbate", Appl. Phys. Lett. **76**, 3825 (2000).

[110] P. Hohenberg and W. Kohn, "Inhomogeneous Electron Gas", Phys. Rev. **136**, B864 (1964).

[111] W. Kohn and L. J. Sham, "Self-Consistent Equations Including Exchange and Correlation Effects", Phys. Rev. **140**, A1133 (1965).

[112] D. M. Ceperley and B. J. Alder, "Ground State of the Electron Gas by a Stochastic Method", Phys. Rev. Lett. **45**, 566 (1980).

[113] J. P. Perdew and A. Zunger, "Self-interaction correction to density-functional approximations for many-electron systems", Phys. Rev. B **23**, 5048 (1981).

[114] D. Vanderbilt, "Soft self-consistent pseudopotentials in a generalized eigenvalue formalism", Phys. Rev. B **41**, 7892 (1990).

[115] P. Giannozzi, S. Baroni, N. Bonini, M. Calandra, R. Car, C. Cavazzoni, D. Ceresoli, G. L. Chiarotti, M. Cococcioni, I. Dabo, A. D. Corso, S. de Gironcoli, S. Fabris, G. Fratesi, R. Gebauer, U. Gerstmann, C. Gougoussis, A. Kokalj, M. Lazzeri, L. Martin-Samos, N. Marzari, F. Mauri, R. Mazzarello, S. Paolini, A. Pasquarello, L. Paulatto, C. Sbraccia, S. Scandolo, G. Sclauzero, A. P. Seitsonen, A. Smogunov, P. Umari, and R. M. Wentzcovitch, "QUANTUM ESPRESSO: a modular and open-source software project for quantum simulations of materials", J. Phys.: Condens. Matter **21**, 395502 (2009).

[116] A. Kokalj, "Computer graphics and graphical user interfaces as tools in simulations of matter at the atomic scale", Comput. Mat. Sci. **28**, 155 (2003).

[117] M. L. Cohen, M. Schlüter, J. R. Chelikowsky, and S. G. Louie, "Self-consistent pseudopotential method for localized configurations: Molecules", Phys. Rev. B **12**, 5575 (1975).

[118] H. Rydberg, M. Dion, N. Jacobson, E. Schröder, P. Hyldgaard, S. I. Simak, D. C. Langreth, and B. I. Lundqvist, "Van der Waals Density Functional for Layered Structures", Phys. Rev. Lett. **91**, 126402 (2003).

[119] K. Lee, É. D. Murray, L. Kong, B. I. Lundqvist, and D. C. Langreth, "Higher-accuracy van der Waals density functional", Phys. Rev. B **82**, 081101 (2010).

[120] V. R. Cooper, "Van der Waals density functional: An appropriate exchange functional", Phys. Rev. B **81**, 161104 (2010).

[121] I. Hamada and M. Tsukada, "Adsorption of C_{60} on Au(111) revisited: A van der Waals density functional study", Phys. Rev. B **83**, 245437 (2011).

[122] G. Li, I. Tamblyn, V. R. Cooper, H.-J. Gao, and J. B. Neaton, "Molecular adsorption on metal surfaces with van der Waals density functionals", Phys. Rev. B **85**, 121409 (2012).

[123] S. Baroni, S. de Gironcoli, A. Dal Corso, and P. Giannozzi, "Phonons and related crystal properties from density-functional perturbation theory", Rev. Mod. Phys. **73**, 515 (2001).

[124] D. Porezag and M. R. Pederson, "Infrared intensities and Raman-scattering activities within density-functional theory", Phys. Rev. B **54**, 7830 (1996).

[125] R. G. Greenler, "Infrared Study of Adsorbed Molecules on Metal Surfaces by Reflection Techniques", J. Chem. Phys. **44**, 310 (1966).

[126] R. M. Hexter and M. G. Albrecht, "Metal surface Raman spectroscopy: Theory", Spectrochim. Acta, Part A **35**, 233 (1979).

[127] N. Sheppard and J. Erkelens, "Vibrational Spectra of Species Adsorbed on Surfaces: Forms of Vibrations and Selection Rules for Regular Arrays of Adsorbed Species", Appl. Spectrosc. **38**, 471 (1984).

[128] Y. J. Song, A. F. Otte, V. Shvarts, Z. Zhao, Y. Kuk, S. R. Blankenship, A. Band, F. M. Hess, and J. A. Stroscio, "Invited Review Article: A 10 mK scanning probe microscopy facility", Rev. Sci. Instrum. **81**, 121101 (2010).

Appendix A

Electronics for Driving Piezo Stacks

A.1 Walker Electronics Overview

We initially experienced unintentional tip crashes into our samples' surface. These crashes, which destroyed the atomically flat surfaces, had often occurred during the initial steps of the tip retraction process. The crashes were caused by the original walker box that was used to actuate the STM piezo stacks. This original walker box was built by the Physics Electronics Support Group. As it has been discussed in Section 1.5.4, the problem was due to the fact that the retraction (the backward motion of the sapphire prism assembly, which includes the tip) was achieved by changing the polarity of the approach waveform whereas a better way to achieve the same motion is to time-reverse the approach waveform. To fix the problem, we built new course worker electronics; its design is described in this appendix. The new electronics, a schematic diagram is shown in Figure A.1, includes a data acquisition (DAQ) board, a high voltage amplifier, and a relatively simple circuit that employs triacs as fast switches (the circuit with the triacs is referred to as the main circuit board in Figure A.1). The idea to use triacs came from Professor Joseph Stroscio's group [128]. It should be also noted that I recently became aware of the work by Chatterjee et al. [50] where many questions directly related to the design are discussed.

In order to achieve a greater flexibility, a National Instruments DAQ board is used to generate low voltage waveforms as well as to handle all the timings. The user interface with the board can be easily realized with a LabVIEW virtual instrument (VI). The use of a DAQ card also helps keep the design of the drive circuit with the triacs very simple.

The low voltage waveforms generated by the DAQ board have to be amplified up to 350–400 V to be capable of efficient actuation of the piezo stacks. As it has been already explained in Section 1.5.4, a single-step waveform should include two phases: a slow ('stick') phase in which the piezo stacks stays attached to the STM prism and a fast ('slip') phase in which the piezo breaks frictional contact with the prism and slides along it. The most demanding part of the driving process is the actuation of the slipping motion. This requires rapid (typically within few microseconds) charging or discharging of the piezo stacks. Since each

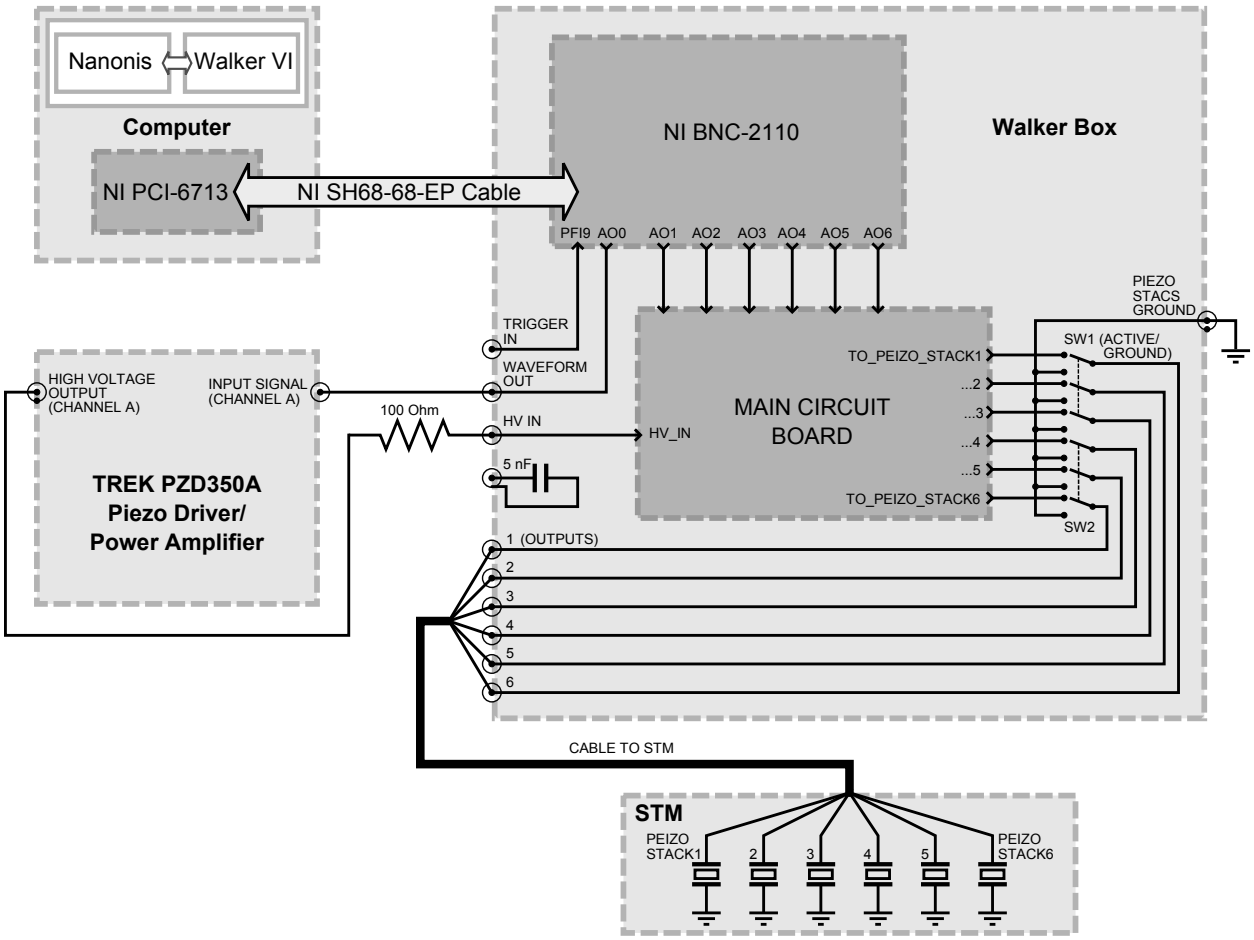

Figure A.1: Schematic of the new walker electronics for driving the STM piezo stacks.

piezo stack can be viewed as a capacitor with $C_{\text{piezo}} \approx 5\,\text{nF}$ at room temperature, charging and discharging currents may be as high as a few amperes. The bipolar dual-channel Trek Model PZD350A Piezo Driver/Power Amplifier (TREK INC.) has the output voltage limits of $V_{\text{lim}} = \pm 350\,\text{V}$, the output current limits of $I_{\text{lim}} = \pm 200\,\text{mA}$ per channel, and the slew rate greater than $550\,\text{V}/\mu\text{s}$. With a given piezo stack capacitive load these numbers put a serious constraint on the shortest rising/dropping time t_{min} achievable with this amplifier: $t_{\text{min}} = C_{\text{piezo}} V_{\text{lim}} / I_{\text{lim}} = 5\,\text{nF} \times 350\,\text{V}/200\,\text{mA} \approx 8.8\,\mu\text{s}$. It should be mentioned that with three dual-channel amplifiers, using one channel per each piezo stack, we were actually able to observe some motion of the STM prism but the motor performance was extremely unreliable even at room temperature.

To overcome the challenge of rapid charging and discharging of the piezo stacks with the given amplifier, a drive circuit with triacs has been designed and built. A schematic diagram of this circuit is shown in Figure A.2. The core idea of the circuit is auxiliary (storage) capacitors C1–C5 placed at the high voltage amplifier output to supply an extra

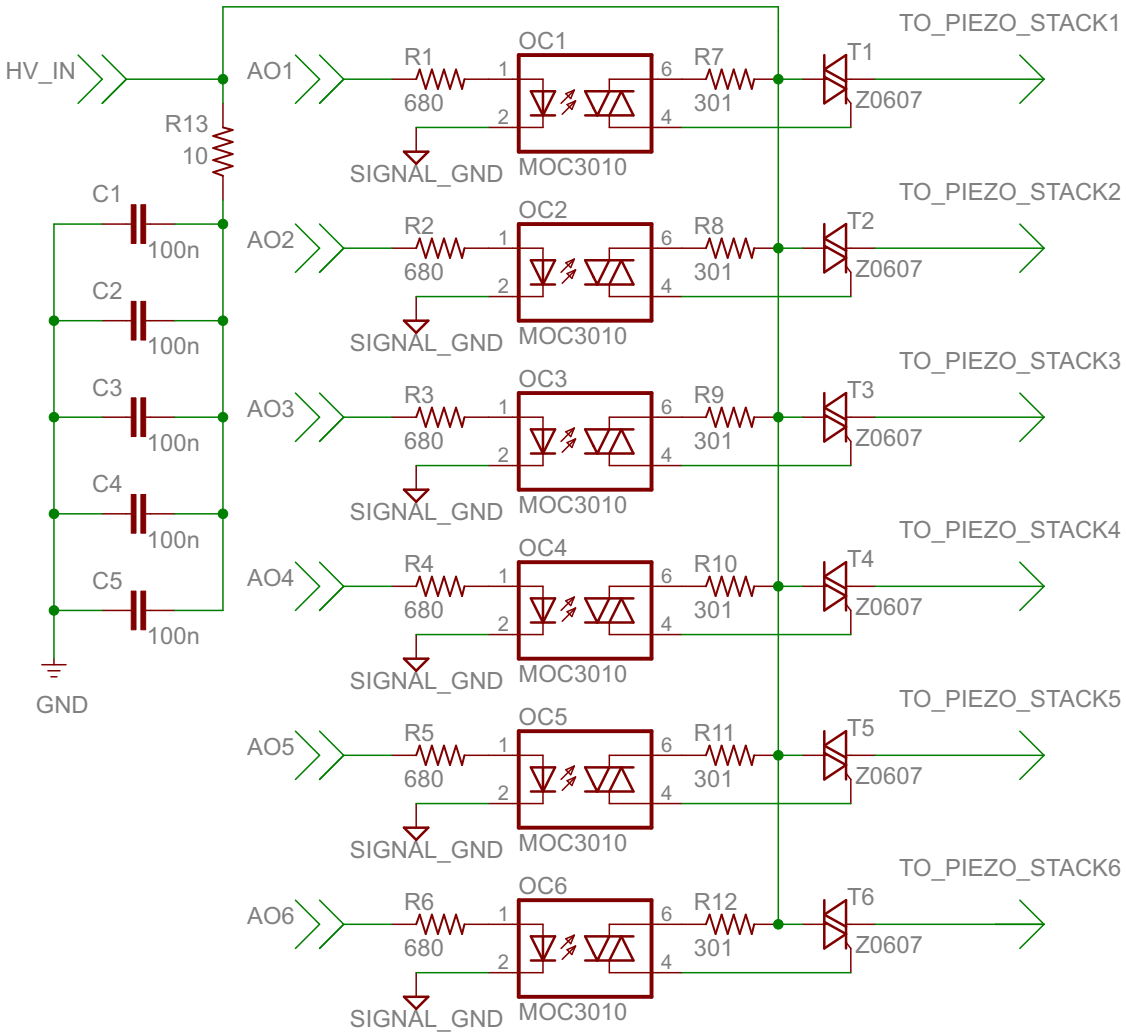

Figure A.2: Electronic schematic of the piezo driving circuit (the main circuit board in Figure A.1).

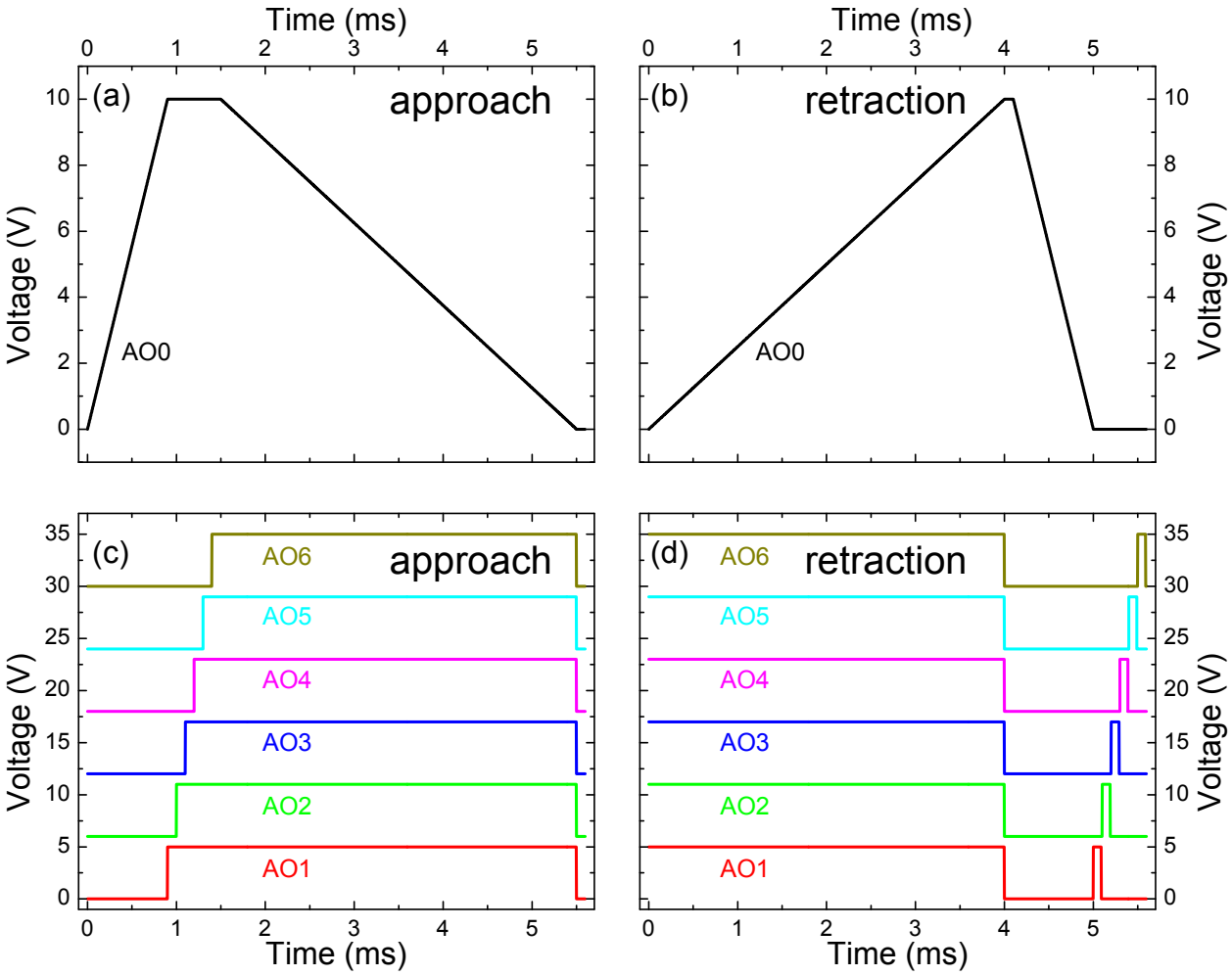

Figure A.3: Waveforms generated by the NI PCI-6713 DAQ board for actuating the piezo motor. (a) Signal from the analog output AO0 for a single approach step. This signal, after passing through the Trek Model PZD350A Power Amplifier, controls the charge on the auxiliary capacitors. (b) Signal from the analog output AO0 for a single retraction step. (c) Signals from the analog outputs AO1–AO6 that control the states of the triacs for a single approach step. The AO2–AO6 lines are vertically offset for clarity. (d) Signals from the analog outputs AO1–AO6 that control the states of the triacs for a single retraction step. The AO2–AO6 lines are vertically offset for clarity.

current during the rapid phase of charging or to serve as a charge sink during the fast discharging phase. Five 100 nF auxiliary capacitors are connected in parallel to increase the overall capacitance. The triacs T1–T6 are used as fast switches and can be driven into the conducting state by the corresponding trigger signals from the DAQ board.

The basic principle of operation is described as the following. During the approach,

each step starts with charging of the auxiliary capacitors [Figure A.3(a)] while all the triacs are switched off. After this, the triacs are switched on, one after another [Figure A.3(c)], causing the rapid rise of the voltages on the corresponding piezo stacks. Then the high voltage amplifier slowly reduces the voltage across the capacitors [Figure A.3(a)] and the piezo stacks to zero. Finally, all the triacs are switched off when the T1–T6 gate voltages are set to zero and all the piezo stacks are discharged (i.e., when there is no current flowing through the main terminals MT1 and MT2 of the triacs T1–T6). Conversely, during the retraction, each step starts with all the triacs being in the conducting state. The piezo stacks and the auxiliary capacitors are slowly charged to a desired voltage [Figure A.3(b)]. When the charging stops there is no current flowing through the triacs T1–T6 and they can be switched off [Figure A.3(d)]. After this, the auxiliary capacitors are discharged through the high voltage amplifier [Figure A.3(b)]. Finally, the triacs are prompted to switch on, driving rapid discharges of the piezo stacks.

A.2 Walker Electronics Design Details

As it is schematically shown in Figure A.1, a NI PCI-6713 DAQ Board (National Instruments Corporation) is plugged in a computer and connected to a NI BNC-2110 Shielded Connector Block (National Instruments Corporation) with a SH68-68-EP Cable (National Instruments Corporation). The analog output AO0 of the DAQ board is used to generate a low voltage waveform to be amplified with a Trek Model PZD350A Power Amplifier. The DAQ board also generates six signals to trigger the triacs. The analog outputs AO1–AO6 were chosen for this purpose to simplify the design. However, the DAQ digital lines can be used instead, should it be desired. The DAQ board is run by a VI (a program in the LabVIEW environment).

The analog output signal AO0 is amplified by the Trek Model PZD350A power amplifier and the high voltage output of the amplifier is connected to the auxiliary capacitors C1–C5. The analog output signals AO1–AO6 are used to control the triacs T1–T6 (Z0607). The low voltage waveform and the trigger signals are shown in Figure A.3. An isolation of the high voltage part of the circuit in Figure A.2 from the low voltage electronics is required. This is achieved with the optocouplers OC1–OC6 (MOC3010). Instead of the Z0607 triacs and the MOC3010 optocouplers, one can use the Q6008L5 triacs and the IL4218 optocouplers. The resistors R1–R6 are employed to limit the current through the photodiodes inside the optocouplers. The triac gate currents are supplied by the auxiliary capacitors and the power amplifier. The circuit in Figure A.2 was assembled on a ProtoBoard-6H-3U (BusBoard Prototype Systems Ltd), and it is refereed to as the main circuit board in Figure A.1. MT1 terminals of the triacs T1–T6 are connected to the piezo stacks with a long cable going from the walker box to the STM. To minimize the electrical noise, the switches SW1 and SW2 (Figure A.1) can be used to ground the piezo stacks when the piezo motor is stopped. The connection to the piezo stacks is provided via the PIEZO STACKS GROUND BNC connector on the front panel of the walker box. It should be noted that grounding the piezo

stacks to the walker box chassis may not be necessarily the best option to minimize the electrical noise.

During the retraction, there are times when the triacs should be switched off with the high voltage on both of its main terminals. This did not happen reliably before the introduction of an auxiliary 100 Ω resistor. The resistor was placed in between the HIGH VOLTAGE OUTPUT of the Trek power amplifier and the HV IN BNC connector wired to the HV_IN port of the main circuit board (Figure A.1).

A.3 Connecting SPM Control Systems to Walker Electronics

The controlled ('fine') stage of the tip approach (referred to as 'Stage 2' in Reference 46) requires at least a one-way communication channel between the SPM control system and the piezo motor electronics. The controlled approach is a procedure that is used to gently bring the STM tip close enough to the surface, so that the tunneling current of a specified value can be established. During this approaching process, the STM control electronics retracts the tip, the piezo motor makes a coarse approach step forward, and then the tip is released under feedback to probe for any tunneling current. If the measured current is lower than the feedback set point current, then the tip is retracted, and the piezo motor makes another step. This process continues until the tunneling current is equal to the set point current.

The described approach protocol requires synchronization of the SPM control system and the walker electronics. The SPM control system should send a request to the walker electronics to make a step and then wait for a specified amount of time. When the walker electronics detects a request for an extra piezo motor step, it should make an approach step within the given amount of time. Should the walker electronics be used with the RHK SPM 1000 Control System, the fine approach transistor-transistor logic (TTL) trigger signal has to be supplied to the TRIGGER IN BNC connector of the walker box (Figure A.1). The TRIGGER IN input is connected to the PFI9 input of the connector block and can be monitored by a VI (see one of the previous versions of the Walker VIs, for example, Walker 2.3).

Pin 7 of the DIO PORT A THROUGH on the backside of the Nanonis HVA4 unit provides a TTL trigger signal that can be used for the controlled stage of the tip approach procedure when the Nanonis SPM Control System is used. With the Nanonis SPM Control System the trigger signal can also be monitored using the Nanonis BP4-PI Programming Interface Software Module (SPECS Zurich GmbH). The later does not require any physical connections between the Nanonis SPM Control System and the walker electronics. If the real TTL signal is used, a connection between pin 7 of the DIO PORT A THROUGH and the inner pin of the TRIGGER IN BNC connector should be made. However, there have been three known cases in our group when this connection was suspected for damaging the NI PCI-7833R board (National Instruments Corporation), which could be found inside

the Nanonis RC4 Real-Time Controller (SPECS Zurich GmbH). Therefore, it is strongly suggested that in the future this connection should be done through an optocoupler. It is recommended to monitor the trigger signal using the Nanonis BP4-PI Programming Interface Software Module and this is implemented with the Walker 4.1 VI, which provides the best way to control the walker electronics. The approach waveforms, the retraction waveforms, and the corresponding trigger signals for each of the triacs are stored in the text files that are external to the VI. Therefore, most modifications to the waveforms can be done by simply modifying these files.

It should be noted here that in order to avoid the tip crashing during the controlled approach, the approach step size must be always shorter than the piezo tube Z range. Since the actual piezo motor step size depends not only on the applied voltage amplitude but also on the tension of the spring plate holding the walker [46], on the STM operating temperature, and on the conditions of the sapphire prism surface, there is no specific voltage amplitude that should be used all the time. The voltage amplitude of the waveform for the controlled approach should be rather determined experimentally. An equal voltage amplitude should be used for the initial steps of the retraction to avoid the tip crashing. The Walker VIs provide a simple interface for controlling the amplitude of the approach and retraction waveforms.

A.4 Performance of Walker Electronics

The performance of the new electronics was documented with a 5 nF capacitive load. The voltages across the capacitive load and the auxiliary capacitors, which were measured with high voltage probes, are shown in Figure A.4. Rapid rises and drops of the voltages from 10% to 90% levels within ~ 300 ns were achieved. There are some transient artifacts that have not been seriously investigated since these artifacts do not compromise the performance of the piezo walker in any detectable way. Optimizations to the electronics are likely possible to improve the shape of the actual high voltage waveforms.

Given the typical voltage rising/dropping times, currents as high as 5 A are expected to flow through the triacs T1–T6. According to the component datasheet, the root-mean-square on-state current for the Z0607 triacs must not exceed 0.8 A. While for the short periods of time this limit is significantly exceeded, the average root-mean-square current through the triacs should be well within the rating. The Q6008L5 triacs might be a better option.

The new electronics for the piezo motor has been working very reliably. No crashes have been detected on reapproaches of the same microscopic sample spots when the proper piezo motor step sizes were chosen.

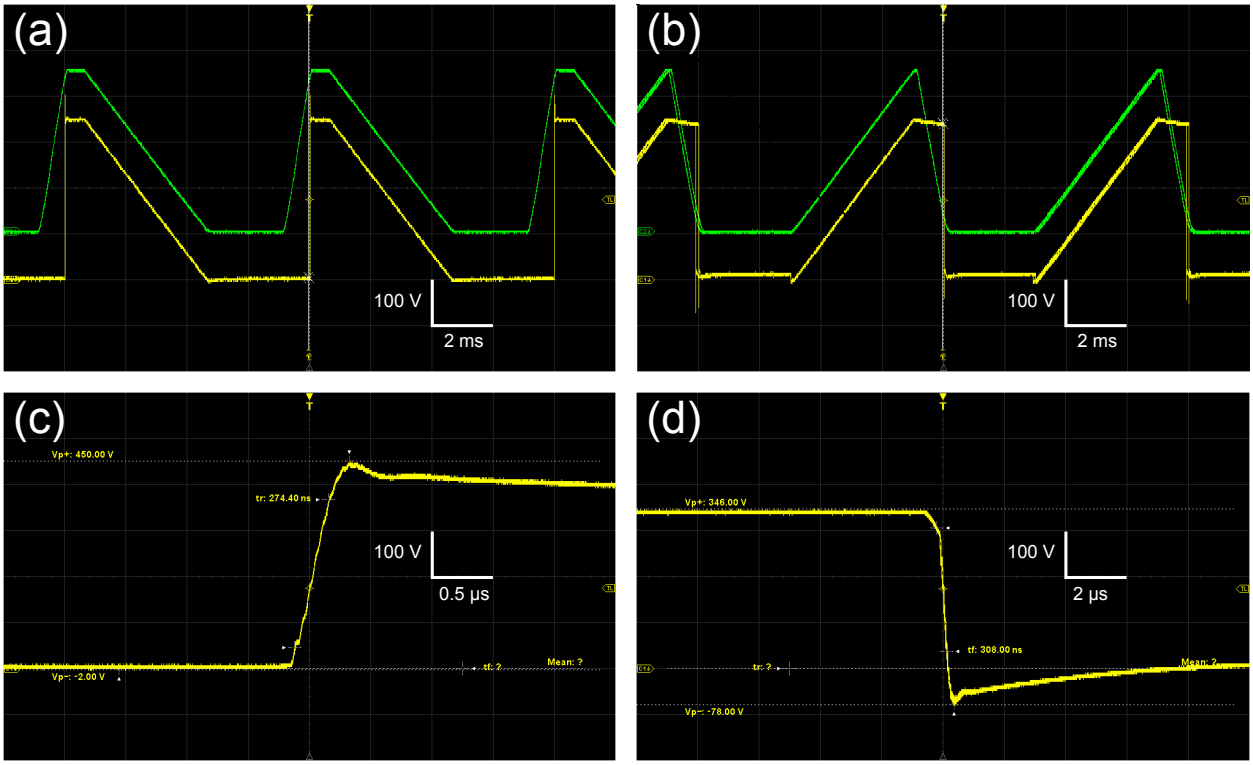

Figure A.4: Performance of the piezo electronics tested with a 5 nF capacitive load: (a) an approach oscillogram, (b) a retraction oscillogram, (c) a zoomed-in oscillogram of the sharp edge of the approach waveform, (d) a zoomed-in oscillogram of the sharp edge of the retraction waveform. The yellow lines indicate the voltage across the capacitor load, while the green lines show the voltage across the auxiliary (storage) capacitors C1–C5.

Appendix B

Heli-tran Transfer Line Sealing

The results reported in this dissertation have been obtained with an STM that is equipped with an LT-3B Heli-tran Open Cycle Cryogenic Refrigeration System (Advanced Research Systems Inc.). An overview of the STM cryogenic system is given in Reference 46. Subsequent improvements to the STM design decreased the base temperature down to $\sim 13\,\mathrm{K}$ [48].

To keep the STM at the base temperature a 100-liter helium dewar can be used to supply liquid helium for 3.0–3.5 days (this corresponds to an average flow of 1.1–1.4 L/hr). However, thermal oscillations had been notably interfering with the STM measurements. The temperature was typically stable during the first day of the STM operation with an initially full dewar but the thermal oscillations became present during the second and the third days. Figure B.1 shows these periodic thermal oscillations that were especially pronounced at the refrigerator cold stage (or 'cold finger' [46]). These thermal oscillations often appeared to have a period of about 21 sec and a peak-to-peak amplitude of more than 1 K. The STM temperature sensor, mounted to the STM sample holder near the sample, showed relatively minor oscillations in the temperature. Nevertheless, these thermal oscillations almost always appeared in the STM topographs due to high sensitivity of the tunneling current to any drifts in the setup caused by the thermal fluctuations. Measurement artifacts due to the thermal oscillations can be seen, for example, in Figure 2.5(a) in the form of alternating horizontal light and dark regions. Increasing the helium flow typically helped achieve slightly lower temperatures but never resulted in effective damping of the oscillations.

It turned out that the oscillations due to the absence of a good seal between the dewar bayonet of the Heli-tran transfer line and the bayonet extension. During the first day of the operation, the oscillations were not seen because the liquid level was above the junction between the extension and the dewar bayonet. Once the liquid level dropped below the junction the oscillations appeared due to two-phase (liquid and gas) flow in the transfer line.

The two-phase flow can be prevented by applying an indium seal between the extension and the dewar bayonet. A piece of an indium wire that has a 1 mm diameter (Advanced Research Systems Inc. or Goodfellow) may be used. The wire should be bent into a ring with a diameter equal to the outer diameter of the extension thread (the thread that goes into the dewar bayonet). The seal should be placed around the bottom of the thread (the

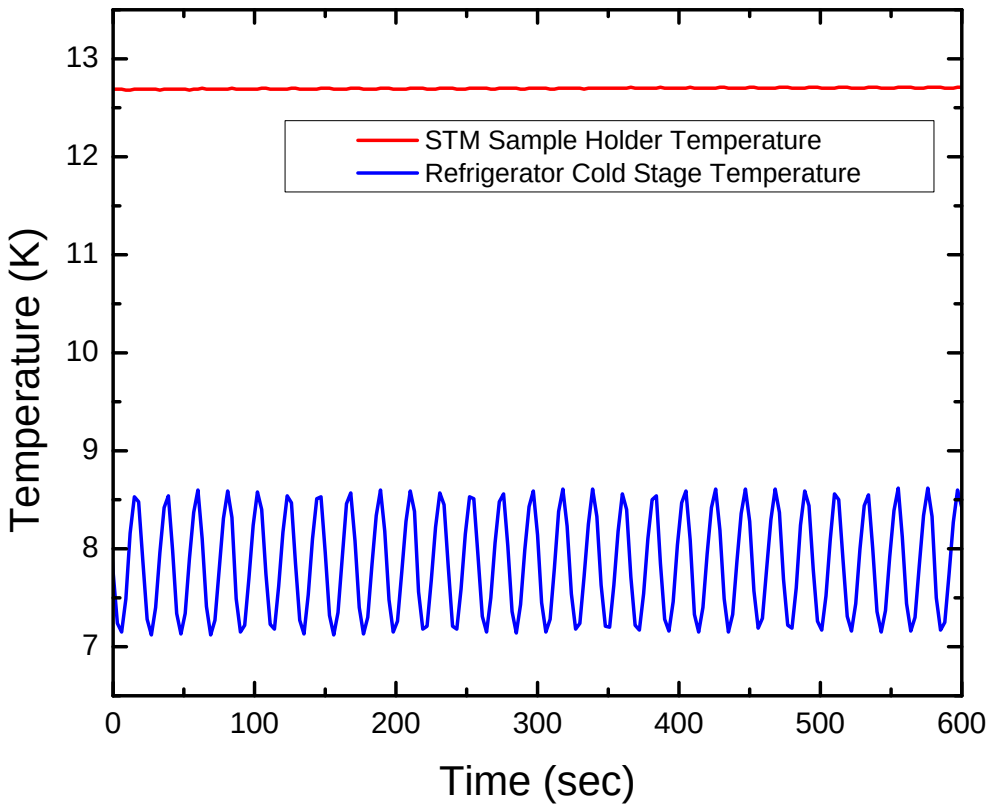

Figure B.1: Temperature oscillations at the refrigerator cold stage (blue line) and at the STM sample holder (red line). The temperature was recorded after 15 hours of the STM operation with an initially full helium dewar.

thread end that is farther away from the dewar bayonet). Finally, the extension has to be screwed into the transfer line bayonet and tighten relatively well with pliers, or very gently with vice grips. After tightening, the indium seal should be visibly compressed.

Introduction of the indium seal was found to completely eliminate the thermal oscillations provided that the high enough liquid helium flow was used.